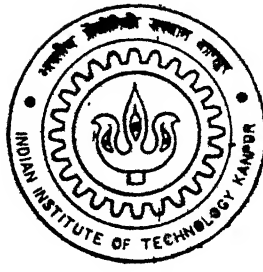


Y010640

# **Processing and Properties Of Mechanically Alloyed Nanocrystalline Nickel-Iron**

**By**

**Shyam Kumar**



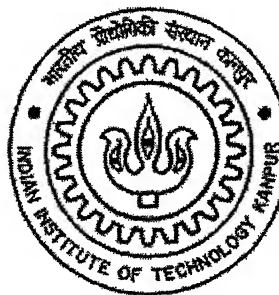
**DEPARTMENT OF MATERIALS AND METALLURGICAL ENGINEERING  
Indian Institute of Technology Kanpur**

**July, 2002**

# **Processing and Properties Of Mechanically Alloyed Nanocrystalline Nickel-Iron**

by

**Shyam Kumar**



**DEPARTMENT OF MATERIALS AND METALLURGICAL ENGINEERING**

**INDIAN INSTITUTE OF TECHNOLOGY, KANPUR**

**July 2002**

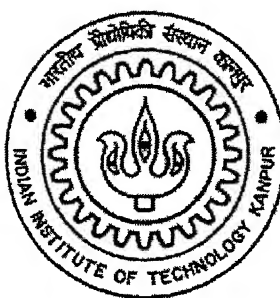
# Processing and Properties Of Mechanically Alloyed Nanocrystalline Ni-Fe

*A Thesis Submitted*  
In Partial Fulfillment of the Requirements  
For the Degree of

**MASTER OF TECHNOLOGY**

by

**Shyam Kumar**  
(Roll No. Y010640)



*to the*

**DEPARTMENT OF MATERIALS AND METALLURGICAL ENGINEERING**

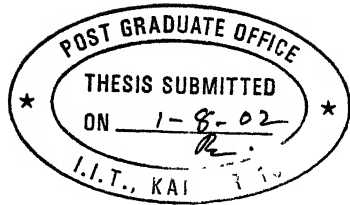
**INDIAN INSTITUTE OF TECHNOLOGY, KANPUR**

**July 2002**

4 FEB 2003 / MMU  
पुरुषोत्तम काशीनाथ देव कर पुस्तकालय  
भारतीय नौदोसिकी संस्थान कानपुर  
अवाप्ति नं. A-141906



A141906



## CERTIFICATE

This is to certify that the thesis entitled "*Processing and Properties Of Mechanically Alloyed Nanocrystalline Ni-Fe*" by Shyam Kumar (Roll No. Y010640) has been carried out under my supervision and to the best of my knowledge this work has not been submitted elsewhere for a degree.

Asim Tewari

Dr. Asim Tewari

Assistant Professor

R.K. Dube

Dr. R.K. Dube

Professor

Department of Materials and Metallurgical Engineering

Indian Institute of Technology

Kanpur-208016, India

Date: July 30, 2002

## Abstract

A mixture of 80 wt% carbonyl nickel and 20 wt% electrolytic iron powders were milled in a high energy ball mill for different periods of time ranging from 5 min to 30 hr in an effort to make nanocrystalline 80Ni-20Fe. The effect of milling time on the crystallite size was studied using XRD technique. It has been shown that the crystallite size decreases with the milling time. The rate of decrease of crystallite size is very rapid between 5 min-12 hr milling time. Beyond this milling time, the crystallite size is more or less constant with respect to the milling time. It has been possible to obtain a crystallite size of 30 nm in the mechanically alloyed 80Ni-20Fe, which was milled for 30 hr. The predominant phase formed has been identified as nickel rich solid solution. The 30 hr ball-milled 80Ni-20Fe powder was mixed with a binder and a homogeneous and free flowing slurry was prepared. The slurry was cast into a strip form and subsequently dried to form a coherent green strip. The green strip was sintered at 1273K under H<sub>2</sub> atmosphere for 15 min. Subsequently it was hot rolled at the same temperature in H<sub>2</sub> atmosphere. Bright field transmission electron micrographs of hot rolled strip of M.A.80Ni-20Fe show structure similar to that of the forest of dislocations, which are low angle grain boundary between the adjacent nanocrystals. The grain size of the final hot rolled strip was found to be 120 nm. The hot rolled strip of M.A. 80Ni-20Fe has density of about 70% of the theoretical. The M/H curve for these materials show nearly zeros coercivity and possibility of lowering remanence by magnetic field annealing. So these materials may have superior soft magnetic properties.

## Abstract

A mixture of 80 wt% carbonyl nickel and 20 wt% electrolytic iron powders were milled in a high energy ball mill for different periods of time ranging from 5 min to 30 hr in an effort to make nanocrystalline 80Ni-20Fe. The effect of milling time on the crystallite size was studied using XRD technique. It has been shown that the crystallite size decreases with the milling time. The rate of decrease of crystallite size is very rapid between 5 min-12 hr milling time. Beyond this milling time, the crystallite size is more or less constant with respect to the milling time. It has been possible to obtain a crystallite size of 30 nm in the mechanically alloyed 80Ni-20Fe, which was milled for 30 hr. The predominant phase formed has been identified as nickel rich solid solution. The 30 hr ball-milled 80Ni-20Fe powder was mixed with a binder and a homogeneous and free flowing slurry was prepared. The slurry was cast into a strip form and subsequently dried to form a coherent green strip. The green strip was sintered at 1273K under H<sub>2</sub> atmosphere for 15 min. Subsequently it was hot rolled at the same temperature in H<sub>2</sub> atmosphere. Bright field transmission electron micrographs of hot rolled strip of M.A.80Ni-20Fe show structure similar to that of the forest of dislocations, which are low angle grain boundary between the adjacent nanocrystals. The grain size of the final hot rolled strip was found to be 120 nm. The hot rolled strip of M.A. 80Ni-20Fe has density of about 70% of the theoretical. The M/H curve for these materials show nearly zeros coercivity and possibility of lowering remanence by magnetic field annealing. So these materials may have superior soft magnetic properties.

## Acknowledgments

At the very outset I want to express my deep regard and gratitude to my thesis supervisors, Dr. R.K. Dube and Dr. Asim Tewari whose brilliant technical prowess and hearty co-operation encouraged me a lot to overcome the frustrated and sluggish moments of experimental and computational research. I would ever remember the unforgettable moments of working with them when they literally guided me through the complicated technicalities of the present work. I convey my heartfelt thanks to all my friends and seniors who gave their invaluable moral support and companionship to make my stay in the IIT-K a pleasant experience. Special mention is due to ShyLu John, Girijesh Shukla, Sanjay Vajpai and Vinit Kr. Dwivedi whose refreshing presence nourished me intellectually.

I gratefully acknowledge the help received from Dr. Subodh Kumar of Dept of Metallurgy, I.I.Sc. Bangalore for quickly providing me XRD data of my samples on latest XRD machine. The help rendered by Mr. S.C. Soni, Mr. Umashanker, Mr. Siva Kumar, Mr. Birthwal, and staff members of the Engineering metallurgy lab. is greatly acknowledged, who selflessly extended their kind co-operation to me during the experimental work. I wish to thank Dr Gautama who helped me in preparing TEM samples.

Last but not the least, I extend my special thanks to my wife N.L.Vijitha who's unconditional love and encouragement always kept my morale high.



Shyam Kumar

## TABLE OF CONTENTS

<b>1. Introduction .....</b>	<b>1</b>
<b>2. Literature Review.....</b>	<b>3</b>
2.1 Nanocrystalline materials.....	3
2.2 Synthesis of Nanocrystalline materials .....	4
2.2.1 Inert gas condensation.....	5
2.2.2 Mechanical Alloying.....	5
2.2.3 Rapid solidification .....	5
2.3 Structure and characterization of nanocrystalline material.....	6
2.4 Properties of nanocrystalline materials.....	8
2.4.1 Diffusivity and Sinterability .....	8
2.4.2 Mechanical properties of nanocrystalline materials.....	9
2.4.3 Chemical properties of nanocrystalline materials.....	10
2.4.4 Magnetic properties of nanocrystalline materials .....	11
2.5 Applications of Nanocrystalline materials.....	11
2.5.1 Structural Applications .....	12
2.5.1.1 Cutting tools.....	12
2.5.1.2 Nanocomposites.....	13
2.5.1.3 Superplastic materials .....	13
2.5.1.4 Coatings .....	14

2.5.2 Magnetic applications .....	14
2.5.3 Catalysis and hydrogen storage materials.....	15
2.5.4. Functional Nanostructures-Electronic Applications .....	16
2.5.5 Bio-medical applications of nanocrystalline materials .....	16
2.6 Consolidation strategy for nanocrystalline materials.....	17
2.6.1 Consolidation temperature .....	18
2.6.2 Consolidation Pressure.....	19
2.6.3 Contamination.....	20
2.6.4 Suppression of grain growth .....	21
2.7 Kinetics of nanocrystalline (metastable) phase transformation .....	22
2. 7. 1 Nucleation of the metastable phases: .....	22
2. 7. 2 The crystal growth rate of the metastable phase: .....	23
2.8 Mechanical alloying.....	24
2.8.1 Raw materials: .....	24
2.8.2 Types of mills .....	25
2.8.2.1 Ball Attritor or Attritor mill .....	25
2.8.2.2 Planetary ball mill .....	26
2.8.2.3 Vibratory ball mill.....	27
2.8.2.4 Low energy tumbling mill .....	27
2.8.2.5 Tumbler ball mill .....	28
2.8.2.6 Tumbler rod mill .....	28
2.8.3 Process variables .....	29
2.8.3.1 Types of mill.....	30

2.8.3.2 Milling container.....	30
2.8.3.3 Ball-to-powder weight ratio.....	31
2.8.3.4 Milling atmosphere .....	31
2.8.3.5 Process control reagents.....	32
2.8.3.6 Milling time .....	33
2.8.3.7 Milling speed .....	33
2.8.3.8 Temperature of milling .....	34
2.8.4 Mechanism of mechanical alloying .....	35
2.8.5 Application of Mechanical Alloying.....	36
2.9 Fe-Ni system .....	36
2.9.1 Crystal structure of the Fe-Ni alloys .....	37
2.9.2 Electromagnetic properties of Fe-Ni alloys .....	38
2.9.2.2 Electrical resistivity of Fe-Ni alloys .....	40
2.9.2.3 Magnetic Anisotropy in Fe-Ni alloys .....	40
2.9.4 High Permeability of Fe-80Ni Alloys.....	41
<b>3. Experimental procedure .....</b>	<b>43</b>
3.1 Raw materials.....	43
3.1.1 Iron Powders .....	43
3.1.2 Nickel Powder.....	43
3.1.3 Binder.....	43
3.1.4 Plastisizer .....	43
3.1.5 Vehicle Medium.....	44
3.1.6 Gases .....	44

3.2 Preparation of nanocrystalline 80Ni-20Fe powder by mechanical alloying.....	44
3.3.1 Preparation of Green Strips by Slurry Casting Methods .....	45
3.3.2 Sintering of the green strips .....	46
3.3.3 Hot densification rolling of the sintered strips.....	47
3.4 Electron Microscopy.....	48
3.4.1 Transmission Electron Microscopy .....	48
3.4.2 Scanning Electron Microscopy .....	48
3.5 X-ray diffraction. ....	49
3.6 Grain size determination of M.A. powders.....	49
3.6.1 PEAKOC.....	49
3.6.2 Procedure for Analysis.....	50
3.7 Laser particle size analysis.....	51
3.8 Density Measurement .....	51
3.9 Magnetic characterization.....	51
<b>4. Result and discussion .....</b>	<b>53</b>
4.1 Size, size distribution and shape of the starting nickel and iron powders, and mechanically alloyed 80Ni-20Fe powders.....	53
4.2 Phase Identification in M.A. 80Ni-20Fe.....	54
4.3 Progressive variation of crystallite size with time of milling .....	54
4.4. Crystallite size of the starting powder .....	56
4.5 Properties of hot strip prepared from the M.A. 80Ni-20Fe powders.....	57
4.5.1 Density of the strip prepared from M.A. 80Ni-20Fe at various stages of processing .	57
4.5.2 Crystallite size of the hot rolled (H.R.) 80Ni-20Fe Strip.....	57

4.5.3 Magnetic properties of the hot rolled 80Ni-20Fe strip.. .. .. .. ..	58
4 5.3.1 Determionation of Curie temperature of 80Ni-20Fe.....	58
<b>5. CONCLUSIONS.....</b>	<b>60</b>
<b>REFERENCES.....</b>	<b>63</b>
<b>FIGURES .....</b>	<b>69</b>
<b>TABLES.....</b>	<b>118</b>

## LIST OF FIGURES

2.1	Schematic representation of four types of nanocrystalline materials (after Siegel 1994).	69
2.2	Schematic representation of a gas condensation chamber for the synthesis of nanocrystalline materials (after Siegel 1990).	70
2.3	Schematic representation of an equiaxed nanocrystalline metal distinguishing between the atoms associated with the individual grains (filled circles) and those constituting the grain boundary network (open circles) (after Gleiter 1989).	71
2.4	Scope of M.A. for fabrication of special purposes materials.	72
2.5	Schematic illustration of excess free energy for critical nucleus for stable and metastable phases vs. temperature.	73
2.6	Hypothetical relation of the growth rate for both stable and metastable phases. In this figure, $\beta$ of stable and metastable phases is 1.4 and 2.0, respectively. For $S_0$ , the value for the metastable phase is three times larger than that of the stable phase.	74
2.7	Szigvari attritor ball mill, the ball is charged by impellers radiating from a rotating vertical shaft, which rotates at speed up to 250 rpm. (After Gilman <i>et al.</i> )	75
2.8	Schematic drawing of a high-energy planetary ball mill.	76
2.9	Schematic drawing of a high-energy vibratory ball mill. (After Hashimoto <i>et al.</i> )	77
2.10	Ball-powder-ball collision of powder mixture during mechanical alloying (Gilman and Benjamin 1983).	78
2.11	Binary phase diagram for the Fe-Ni system (Massalski <i>et al.</i> 1990).	79
2.12	Effect of composition on lattice parameter (a) and density in Fe-Ni alloys at 20°C	80

2.13	Variation of the Curie point and magnetic moment 770C is added to nickel, which has only $0.6\mu_B$ in Fe-Ni alloys (Nakamura, 1976)	81
2.14	Effect of Mo on the resistivity of different Fe-Ni alloys.	82
2.15	Maximum impedance permeability for a 80Ni-15Fe-5Mo alloy as a function of annealing temperature.	83
Fig 3.1	Hot rolling mill arrangement	84
Fig 3.2	Model 155 Magnetometer system	85
Fig 3.3	Simplified block diagram of the model 155 Magnetometer.	86
Fig 4.1a:	Size distribution of carbonyl nickel powder.	87
Fig 4.1b:	Size distribution of electrolytic iron powder.	88
Fig 4.2a:	Size distribution of carbonyl nickel powder determined by Laser Particle Size Analyzer.	
		89
Fig 4.2b:	Size distribution of electrolytic iron powder determined by Laser Particle Size Analyzer.	
		90
Fig 4.2c:	Size distribution of mechanically alloyed 80wt%Ni-20wt%Fe powder (milling time =30hrs) determined by Laser Particle Size Analyzer.	91
Fig 4.3a:	SEM photograph of carbonyl nickel powder	92
Fig 4.3b:	SEM photograph of electrolytic iron powder	93
Fig 4.3c:	SEM photograph of mechanically alloyed 80Ni-20Fe powder (milling time=30hrs)	
		94
Fig 4.3d:	SEM photograph of mechanically alloyed 80Ni-20Fe powder (milling time=30hrs)	
		95
Fig 4.4:	XRD pattern of mechanically alloyed 80Ni-20Fe powder (milling time=5min)	96
Fig 4.5:	XRD pattern of mechanically alloyed 80Ni-20Fe powder (milling time=12 hr)	97
Fig 4.6:	XRD pattern of mechanically alloyed 80Ni-20Fe powder (milling time=23hr)	98

Fig 4.7:	XRD pattern of mechanically alloyed 80Ni-20Fe powder (milling time=30hr)	99
Fig 4.8:	XRD pattern of pure standard Si powder	100
Fig 4.9:	Comparison of XRD patterns of mechanically alloyed 80Ni-20Fe powders for 5min, 12hr, 23hr and 30hr.	101
Fig 4.10:	Effect of milling time on the crystallite size of mechanically alloyed 80Ni-20Fe	102
Fig 4.11:	XRD pattern of as received carbonyl nickel powder.	103
Fig 4.12:	XRD pattern of carbonyl nickel powder after sintering for 1hr at 1100 <sup>0</sup> C in a porcelain boat under hydrogen atmosphere.	104
Fig 4.13:	XRD pattern of as received carbonyl nickel powder.	105
Fig 4.14:	XRD pattern of electrolytic iron powder after sintering for 1hr at 1100 <sup>0</sup> C in a porcelain boat under hydrogen atmosphere.	106
Fig 4.15:	Profile shape function of Gaussian type for carbonyl nickel. This shows the value of respective 2θ and FWHM.	107
Fig 4.16:	Profile shape function of Gaussian type for carbonyl nickel sintered at 1100 <sup>0</sup> C under H <sub>2</sub> atmosphere. This shows the value of respective 2θ and FWHM.	108
Fig 4.17	Bright field images of hot rolled mechanically alloyed 80Ni-20Fe seen under Transmission Electron Microscope (a, b, c, d, e and f).	109
Fig 4.18:	Selected area diffraction patterns of hot rolled mechanically alloyed 80Ni-20Fe seen under Transmission Electron Microscope (a, b, c, d, e and f).	112
Fig 4.19:	Temperature dependence of magnetizations for hot rolled mechanically alloyed 80Ni-20Fe at a rate of 3K/min. the Curie temperature was found to be 525 <sup>0</sup> C	115
Fig 4.20:	Magnetic field dependence of saturation magnetization for mechanically alloyed 80Ni-20Fe at room temperature.	116

## List of tables

Table 1.1:	Changes in the properties at the nanocrystalline size scale	118
Table 1.2:	Current and projected U.S. market for nanostructured materials	118
Table 2.1:	Classification of nanocrystalline materials.	119
Table 2.2:	Commonly used methods of synthesis of NCM.	119
Table 2.3:	Attributes of Mechanical Alloying.	120
Table 2.4:	Types of mill and typical sample weight generally used [12].	120
Table 2.5:	Commonly used process control reagents (PCR) [34].	121
Table 2.6:	Properties of Ferromagnetic and neighboring transition elements [26].	121
Table 3.1:	Slurry composition used for casting green strip of M.A. 80Ni-20Fe.	122
Table 4.1:	Interpolated values of the particle size of Ni, Fe,,and M.A. 80Ni-20Fe(milling time=30hr) powders.	124
Table 4.2:	Particle size of Ni, Fe and 80Ni-20Fe (milling time=30hr) powders corresponding to various d values.	125
Table 4.3:	Profile shape function fitting parameter for M.A. 80Ni-20Fe a) Gaussian Fit b) Pseudo-Voigt fit.	126

Table 4.4:	Variation of grain size with milling time.	127
Table 4.5:	Ratio of d spacing vs. crystallite size.	127
Table 4.6:	Density of the strip prepared for M.A. 80Ni-20Fe powders at various stages of processing.	128

# CHAPTER 1

## 1. Introduction

Nanostructured materials have triggered an explosion of scientific and industrial interest over the last decade. The unique materials are distinguished from conventional by their extremely fine crystallite sizes. A typical nanocrystal has a diameter of up to 100 nm; the crystals of conventional materials are many orders of magnitude larger. Nanostructured (or nanocrystalline) microstructures can be obtained in metallic, ceramic and semi conducting, and diamond materials. According to M.C. Roco, chair of the national Science Foundation's (NSF) directorate on the nanosciences, USA, nanotechnology is defined as "the ability to work at the molecular level, atom by atom, to create large structures with fundamentally new properties and functions." Having a working understanding of atomic structures is "leading to unprecedented understanding and control over the basic building blocks and properties of all natural and man made things," says, Roco, making these science fiction like ideas an engineering challenge rather than a fantasy [1].

While their distinctive microstructures have made nanocrystalline materials a scientific curiosity, discoveries of unusual or enhanced nanomaterial properties (Table 1.1) have elicited an increasing amount of commercial interest. Companies worldwide are working to capitalize on these promising materials. According to the technical market research study Opportunities in Nanostructured Materials, published recently by Business Communications Company, the overall U.S. market for nanostructured particles and coating is valued at an estimated 342.3

million for 1996 (Table 1.2). In 2001, the U.S. market for nanostructured material is projected to reach \$154.6 million corresponding to an average growth rate of 29.6% from 1996 to 2001 [2].

Although much of the work being done in this field is developmental, there are indeed nanostructured products currently in the market. Nanosized particles are incorporated into commercially available polishing slurries, fire retardant materials, magnetic fluids, magnetic recording tapes, sunscreens, and transparent wood stains, among other products. High performance nanostructured coatings have seen some commercial use and are primarily in the prototype stages of development. Currently, the only bulk nanostructured material that has found industrial use is a soft magnetic iron based alloy produced by Vacuuschmelze of Germany. Besides metallic, the nanostructured powders and dispersions available in industrial scale quantities are ceramics, primarily oxides. Nanostructured silica and iron oxide powders have a commercial history spanning about half a century, whereas nanocrystalline alumina, titania, antimony oxide and other materials have more recently entered the market place. The non-oxide ceramic nanopowders available in commercial scale quantities are carbides, especially tungsten carbides. These powders are currently available in the particle sizes in the range of approximately 50 nm to 200 nm [2,3].

The present investigation is aimed at producing nanocrystalline Ni-Fe (4:1) powders by high-energy ball milling in a laboratory scale planetary mill and their processing into flat strips by hot slurry casting followed by densification rolling. SEM, TEM and XRD have been utilized as characterizing tools. The saturation magnetization and Curie temperature have been determined by Vibrating Sample Magnetometer (VSM).

# CHAPTER 2

## 2. Literature Review

### 2.1 Nanocrystalline materials

Nanocrystalline materials have been now investigated for more than a decade using a rather wide range of experimental methods [4-6]. The structures and properties of these new materials, which are artificially synthesized from nanometer sized clusters or powders, have been elucidated in a number of important areas and the relationships among these areas are beginning to be unfolded. Various investigations of their chemical, mechanical, electrical, magnetic, and optical behavior have already demonstrated the possibilities to engineer the properties of nanophase materials through control of their sizes and constituents [7,8]. There remain, however, tremendous opportunities for creative new tailored synthesis and processing methods.

Nanostructured materials, which are modulated over nanometer length scales, can be assembled with modulation dimensionalities of zero (atom clusters or filaments), one (multilayers), two (ultra fine grained over layers or coatings or buried layers), and three (nanophase materials), or with intermediate dimensionalities. Table 2.1 shows this classification and Fig 2.1 illustrates the four types of nanostructures schematically [8]. Thus, nanocomposite materials containing multiple phases can range from the most conventional case in which a nanoscale phase is embedded in a phase of conventional sizes to the case in which all the constituent phases are of nanoscale dimensions. All nanostructured materials share three

fundamental features, which make them useful to consider as a set of atomic domains (grains, layers or phases) spatially confined to less than 100 nanometers in at least one dimension, significant atom fractions associated with interfacial environments, and interactions between constituent domains.

## 2.2 Synthesis of Nanocrystalline materials

Synthesis of nanocrystalline materials dates back to the pioneering investigation of H. Gleiter of the University of Saarlandes in Germany in 1981 [9]. He synthesized ultra fine nanometer sized metallic particles using an inert gas condensation technique and consolidated them in-situ small discs under ultra-high vacuum conditions. Since then a number of techniques have been developed in which a starting material can be either in solid, liquid or gaseous states.

In principle, any method capable of producing very fine grained sized polycrystalline materials can be utilized to produce NC materials [10]. The grain size, morphology, and texture can be varied by suitably modifying/controlling the process variables in these methods. If a phase transformation is involved, e.g. liquid to solid, or vapor to solid then steps need to be taken to increase the nucleation rate and decrease the growth during the formation of the product phase. We shall now describe the different methods of preparing nanostructured materials starting from the vapor, liquid, or solid phases. The Table 2.2 summarizes the commonly used methods to synthesize nanocrystalline materials. Some of the most commonly used methods are described below:

### 2.2.1 Inert gas condensation

In this method, a metal or a mixture of metal is evaporated inside an ultrahigh vacuum (UHV) chamber filled with helium gas. As a result of inter-atomic collisions with the He-atoms in the chamber, the evaporated metal atoms lose their kinetic energy and condense in the form of small crystals of loose powder. These accumulate, due to convective flow, on a vertical liquid nitrogen filled cold finger. The powder is stripped off the cold finger by moving an annular Teflon ring down the length of the tube into a compaction device. The scrapping and compaction process are carried out under UHV conditions to maintain cleanliness of the particle surfaces (and subsequent interfaces) and also to minimize the amount of any entrapped gases (Fig. 2.2) [11]. High densities of as compacted samples have been measured with values of about 75-90% of bulk density for metal samples.

### 2.2.2 Mechanical Alloying

This process consists of repeated welding, fracturing, and re-welding of powder particles in a high-energy ball mill. This has been dealt in detail in the section 2.8.

### 2.2.3 Rapid solidification

If the cooling rate (or the under cooling) during rapid solidification of metallic melts is increased to a high values, then it is possible to increase the nucleation rate (and decrease the growth rate)

of the solid phase and consequently the grain size of the resultant product will be in the nanometer range. But this prediction has not been realized in practice, except in some special situations. A single-phase HfNi<sub>5</sub> nanocrystalline alloy (Lu et al. 1995) has been produced directly by rapid solidification. More frequently, nano-composites have been produced by this method during rapid solidification of metallic melts or during devitrification of metallic glasses produced by rapid solidification [12].

### 2.3 Structure and characterization of nanocrystalline material

A schematic representation of a hard sphere model of an equiaxed nanocrystalline metals shown in Fig 2.3 [6,13]. Two types of atoms can be distinguished: crystal atoms with nearest neighbor configuration corresponding to the lattice and the boundary atoms with a variety of inter-atomic spacing, differing from boundary to boundary. A nanocrystalline metal contains typically a high number of interfaces ( $\sim 6 \times 10^{25} \text{ m}^{-3}$  for a 10 nm grain size)[12] with random orientation relationships, and consequently, a substantial fraction of the atoms lies in the interfaces. Assuming that grains have the shape of spheres or cubes, the volume fraction of atoms associated with the boundaries can be calculated as

$$C = 3\Delta / d \quad (1)$$

Where  $\Delta$  is the average grain boundary thickness and  $d$  is the average grain diameter.

In order to understand the inter-relationship between structure and properties, nanocrystalline materials need to be characterized on both atomic and nanometer scale [14]. The

microstructural features of importance include (a) grain size, distribution and morphology, (b) the nature and morphology of grain boundaries and interphase interfaces, (c) the perfection and nature of intra-grain defects, (d) composition profiles across grains and interfaces, and (e) identification of residual trapped species from processing. In the case of layered nanostructures, the features of importance are (a) the thickness and coherency of interfaces, (b) composition profiles across interfaces, (c) the nature of defects.

There is a gamut of experimental techniques that can yield structural information on nanocrystalline materials. These include 'direct' microscopic techniques such as transmission electron microscopy (TEM), scanning tunneling microscopy (STM), field ion microscopy (FIM), and the less direct electron, x-ray, and neutron diffraction. Indirect spectroscopic tools such as extended x-ray absorption fine structure (EXAFS), nuclear magnetic resonance (NMR), Raman and Moss Bauer spectroscopy, and positron lifetime spectroscopy have been employed. Other useful tools employed include differential scanning calorimetry (DSC), mass spectroscopy, x-ray fluorescence, atomic absorption spectroscopy, Auger electron spectroscopy and hydrogen absorption.

Transmission electron microscopy (TEM) techniques (especially, the high-resolution TEM studies) are ideal to directly determine the grain sizes of nanocrystalline materials using the dark field technique. The width of Bragg's reflection in an X-ray (large angle) diffraction pattern can provide grain (or crystal) size information after the appropriate corrections (for instrumental and strain effects) are incorporated. The TEM techniques can clearly indicate whether there is a distribution of grain sizes and it is also possible to a grain size histogram by measuring the grain sizes and counting the number of grains. On the other hand, the X-ray diffraction technique gives only the average crystal size.

Owing to the ultra fine scale of these materials, traditional characterization tools such as TEM and X-ray and neutron diffraction are both necessary and useful to understand the structure of nanocrystalline materials. However for micro-chemical analysis on the requisite fine scale, further advances in the state of the art of instrumental capabilities will be necessary to obtain the desired lateral scale resolution. Only atom probe FIM or STM can offer the required lateral scale resolution for such chemical mapping.

## 2.4 Properties of nanocrystalline materials

Nanocrystalline materials have a variety of properties that are considerably different and improved in comparison with those of conventional coarser grain structures. These results from the impact of various combinations of the three important aspects (size, composition, and interfaces) of their nature. These include increased strength/hardness, enhanced diffusivity, reduced density, higher electrical resistivity, increased specific heat, higher thermal expansion coefficient, lower thermal conductivity, and superior soft magnetic properties [10]. A few examples will be presented here to try and give a sense of how the interplay among these aspects can significantly alter some useful technological properties of these materials.

### 2.4.1 Diffusivity and Sinterability

Since nanocrystalline materials contain a very large fraction of atoms at the grain boundaries, the numerous interfaces provide a high density of short circuit diffusion paths. Consequently they are expected to exhibit an enhanced diffusivity in comparison to single crystals or conventional

coarse-grained polycrystalline materials with the same chemical composition [15]. This enhanced diffusivity can have a significant effect on mechanical properties such as creep and super plasticity, ability to efficiently dope nanocrystalline materials with impurities at relatively low temperatures, and synthesis of alloy phases in immiscible metals and at temperatures much lower than those usually required in other systems.

The increased diffusivities leads to increased solid solubility limits, formation of intermetallic phases (at temperatures much lower than those required for coarse-grained materials and sometimes new phases) and increased sinterability of nanocrystalline powders.

#### 2.4.2 Mechanical properties of nanocrystalline materials

The elastic constants of nanocrystalline materials have been found to be reduced by 30% or less. These results were interpreted as a result of the large free volume of the interfacial component resulting from the increased average inter-atomic spacing in the boundary regions. The reduction in Young's modulus values was interpreted to be high porosity and cracks in the samples.

The Hall-Petch relationship for conventional coarse-grained polycrystalline materials suggests that the yield strength (or hardness) of a material increases with a decreasing grain size according to the relationship

$$\sigma = \sigma_0 + K_h d^n \quad (2)$$

Where  $d$  is the grain size,  $\sigma$  the 0.2% yield strength (or hardness),  $\sigma_0$  the lattice friction stress to move individual dislocations (or the hardness of a single crystal specimen,  $d \rightarrow \infty$ ),  $n$  the grain size exponent (generally  $-1/2$ ), and  $K_h$  a constant, called the Hall-Petch intensity parameter.

Accordingly nanocrystalline materials are expected to show a much higher yield strength than the coarse grained materials of the same composition. However it should be realized that the above equation has certain limitations [16]. First, the strength value cannot increase indefinitely to beyond the theoretical strength limit. Second, any relaxation process-taking place at the grain boundaries (because of the very fine grain size) could lead to a decrease in the strength and, thus an inverse Hall-Petch relationship could result below some critical grain size. Third, the Hall-Petch relationship was derived on the basis of strengthening resulting from dislocation pile-ups at physical obstacles. At extremely fine grain sizes, e.g., in the nanometer range, the individual grains cannot support more than one dislocation; and thus the Hall-Petch relationship may not be valid. Thus it is logical to expect that the mechanism of hardening/softening observed in nanocrystalline materials may be fundamentally different from that observed in coarser grained metals.

#### 2.4.3 Chemical properties of nanocrystalline materials

A majority of the processing methods produce the nanocrystalline materials in the form of powder, and therefore the total surface area available can be accurately tailored by controlling the particle and grain sizes through the processing parameters. Most important evidence of chemical reactivity of such material is demonstrated by their enhanced catalytic activity [17]. Recently, it has been emphasized that such catalytic activity is evolved in the environmental problems due to enhancement in the activity of aerosols due to their fine size. The effect of particle size on gas-metal interaction has been utilized in the development of nanocrystalline

materials for H<sub>2</sub> storage application. Moreover, enhanced diffusion mechanism in nanocrystalline materials may also be included in the novel chemical properties.

#### 2.4.4 Magnetic properties of nanocrystalline materials

Changes in magnetic properties of nanoscale ferromagnetic materials can be attributed to their small volume, which means they are typically single domain, and to the large fraction of atoms associated with the grain boundaries/interfaces. If the single domain nanoscale ferromagnetic particles (e.g., Fe, Co, or Ni) are put in a non-magnetic matrix such that their magnetic interaction is negligible, a super paramagnetic material is obtained. If the grain sizes are small enough, the structural distortions associated with the surfaces or interfaces can lower the Curie temperature, T<sub>c</sub>, and reduce the magnitude of the saturation magnetization M<sub>s</sub> [12,13]. For example, the M<sub>s</sub> of 6 nm Fe was reported to be 130emu/g compared to 220 emu/g for normal polycrystalline Fe. The curie temperature of 10nm Gd was decreased about 10K from that of coarse-grained Gd, and the transition was broader.

#### 2.5 Applications of Nanocrystalline materials

Nanocrystalline materials are relatively new and it is only during the past few years that researchers have started exploring the many potential benefits of these materials. A number of applications have been suggested based on the special attributes of these materials. Currently, bulk nanostructured soft magnetic iron based alloys and WC-Co composites have found

industrial uses (Rittner and Abraham 1998). Fig 2.4. Schematically shows the illustration of application of NC materials.

## 2.5.1 Structural Applications

Nanocrystalline have much higher hardness and strength than conventional coarse-grained materials. The enhanced diffusivity of these materials allows them to be deformed more easily, and at least in some cases, super-plastically. The present and potential applications of NC materials based on these properties are highlighted below.

### 2.5.1.1 Cutting tools

It has been shown that the hardness and strength of nanocrystalline materials is 4-5 times higher than that of coarse-grained materials of the same composition. McCandlish et al. (1994) have shown that the hardness of WC-Co composites with nanometer WC grains increases with decreasing grain size, reaching values as high as 2,200 VHN. Scratch test suggested that the higher hardness in nano-grained WC-Co is also accompanied by increased toughness. Thus, the abrasive wear resistance of nanostructured WC-Co is higher than the abrasive resistance of conventional WC-Co when the comparison is made at equal hardness. Thus, nanocrystalline WC-Co cutting tools are expected to have more than double the lifetime than conventional coarse-grained composites. These materials could also be used as fine drill bits for drilling holes in printed circuit boards (PCB) and as rotary cutting tools because of the fine grain size, sharp edge, and smooth surface finish.

### 2.5.1.2 Nanocomposites

Nanocomposites are those materials in which either the reinforcement or the matrix or both are having grains of nanometer scale. Further, nanocomposites may be such that the nano reinforcement may be distributed either in the grain boundaries or inside the grains (Niihara 1991). Bhaduri and Bhaduri (1998) have done a comprehensive review on ceramic nanocomposites [20].

It has been known that dispersing a second phase on a microscopic scale can considerably enhance the fracture toughness of ceramics. Since reducing the grain size to nanometer dimensions can provide increased strength and hardness, it is suggested that fabrication of micro/nanohybrids will lead to a class of super tough and super strong ceramics. In these hybrids, a nanocomposite matrix is reinforced with sub micron sized particles-whiskers, platelets, and long fibers- and these hybrids show enhanced fracture toughness and strength up to very high temperatures. Further, nano reinforcements increase creep resistance by suppressing grain boundary sliding.

### 2.5.1.3 Superplastic materials

It has been shown that materials in the nanocrystalline state show tendencies of super plastic deformation at temperatures lower and strain rates higher than conventional coarse-grain materials. Thus the deformation behavior of SiC/SiC nanocomposites has been comparable with metals and  $\text{Si}_3\text{N}_4/\text{SiC}$  composites have shown to deform super plastically [21]. Since ceramics

and conventionally brittle intermetallics can be rendered ductile at elevated temperatures (at least in some cases) by nanostructure processing. These materials can be formed to near net shape by means of deformation processing methods previously applicable only to produce ductile metal parts [12,19].

#### 2.5.1.4 Coatings

The high hardness and strength of nanocrystalline materials can be utilized to produce wear-resistant coatings. With the gas turbine industry's demand for higher operating temperatures to provide enhanced fuel efficiency, thermal barrier coating with reduced thermal conductivity provide the highest pay-off coating application. Because of the small grain size and increased phonon scattering at grain and layer boundaries, nanocrystalline coatings should adhere better and at the same time should exhibit reduced thermal conductivity.

#### 2.5.2 Magnetic applications

The exceptional soft magnetic properties of the "FINEMET" and "Nanoperm" nanocrystalline/amorphous Fe-base alloys promise applications in transformer cores for power frequencies, saturable reactors, high frequency transformers, and magnetic heads. Additional probable applications are for data communication interface components (pulse transformers), sensors (current transformers, magnetic direction sensors), common mode choke coils, magnetic shielding. Magnetic recording materials to some extent already use nanostructured materials. Magnetic materials are used in both the information storage media and in the "write" and "read"

heads. It is predicted that in the future essentially all media and heads will contain nanostructured materials.

### 2.5.3 Catalysis and hydrogen storage materials

Finely dispersed materials are traditionally used in catalysis because of the high specific surface area that is obtained when a sample is divided into small portions. In fact some of the first applications of nanoparticles were as catalysts (Ponec 1975). It has been shown in several studies that the catalytic activity and selectivity can be dependent on particle size. A strong correlation was observed between Pt particle sizes and catalytic activity.

Metal hydrides offer the best compromise of safety, efficiency, and for storage of hydrogen for use as a fuel. It was believed that a way to enhance their properties is to produce the materials in nanocrystalline form. The high density of grain boundaries/interfaces might increase diffusion. Nanocrystalline  $Mg_2Ni$  inclusions in a two phase  $Mg/Mg_2Ni$  alloy showed improved hydrogen storage behavior in terms of  $Mg_2Ni$  catalyzing the decomposition of the molecular hydrogen, greatly increasing the hydrogen absorption/desorption kinetics (Wasz et al. 1995). A further advantage of the nanoscale microstructure is that the alloy powder does not comminute as the result of repeated hydrogen charging-discharging cycles [12].

#### 2.5.4. Functional Nanostructures-Electronic Applications

“Functional” electronic and optical nanostructures are typically fashioned from single-crystal semiconductor materials using a variety of possible pattern formation (e.g., electron beam lithography) and pattern transfer processes (e.g., reactive ion etching), which can create structures at the nanoscale. By replacing inks with nanoparticles solutions, it is also conceivable that we could print structures onto surfaces e.g., printing electronic circuits. This is a large area of research and development of importance to the microelectronics industry for future directions such as quantum circuits and systems, massive memory, architecture and interconnected systems.

#### 2.5.5 Bio-medical applications of nanocrystalline materials

Magnetic nanoparticles are being used in biomedical research on cell separation, for magnetically targeted drug delivery, for protein and DNA purification, and for contrast enhancement in magnetic resonance imaging (MRI). Efforts increase the magnetic moment of the particles, which could enhance the contrast of MRI or reduce the concentration of magnetic particles needed for cell separation, or make drug delivery possible with lower magnetic field gradients. Functionalization of the nanoparticle surface could enable the selective attachment to particular type of cells. Magnetic nanoparticles for selective tag could someday be used in HIV immune therapy or the treatment of blood diseases. If magnetic nanoparticles were attached to cancer cells, they could be used for hypothermia, raising the local temperature about  $42^{\circ}\text{C}$  increases their sensitivity to radiation and chemotherapy, and heating above  $42^{\circ}\text{C}$  causes a

significant amount of cell death. AC magnetic field can heat magnetic nanoparticles, analogous to the way microwaves excite water molecules when food is cooked in a microwave oven. It is possible to design magnetic nanoparticles for maximum power dissipation at a particular frequency, within a frequency band that does not harm other biological functions.

Nanoparticles additions can be used in suns creams and cosmetics to protect our skin against UV rays, in plastics for out door applications to prevent UV-induced weathering and in bottle coatings to protect beer, wine and olive oil against photo degradation.

## 2.6 Consolidation strategy for nanocrystalline materials

The potential application of nanoscale materials as novel structural or functional engineering materials largely depends on the consolidation of powders into bulk nanoscale solids [12,22]. The retention of metastable microstructure in the course of this consolidation process is essential for preserving the often-superior mechanical, magnetic, or catalytic properties of the material [1]. Consolidation of the NC powders has been achieved by electro-discharge compaction (Okazaki 1993); plasma activated sintering (Groza 1993,1994); shock consolidation (Suryanaryana et al. 1997); hot isostatic processing [24], Hydrostatic extrusion (Liang et al. 1996); strained powder rolling (Liang et al. 1996a); and sinter forging (He and Ma 1996b). Optimization of consolidation parameters is important because retention of nanostructures requires use of low consolidation temperatures while achieving full (theoretical) density requires use of high temperatures [23]. However, it should be noted that because of the increased diffusivities in nanocrystalline materials, sintering (densification) takes place at a temperature much lower than in coarse-grained materials. This is likely to reduce the grain growth. It is

typically difficult to obtain full density while retaining the nanoscale microstructure. The high driving force and enhanced kinetics due to large curvature facilitates full densification of nanocrystalline materials at temperatures consistently below those of coarse-grained materials of the same composition by few hundred degrees. Retention of fine grain sizes and elimination of sintering aids are specific advantages of the lower processing temperatures [13-15].

### 2.6.1 Consolidation temperature

For conventional materials, pores are removed through sintering at high temperatures for long times, driven by the reduction in surface energy. For nanophase materials, consolidation temperature needs to be kept low to maintain nano scale grain sizes. Full densification is possible at some intermediate elevated temperatures because nanophase powders are expected to show increased sinterability compared with their conventional coarse-grained counterparts. A reduction in sintering temperature can reduce contamination and compositional changes, and stresses and cracking during cooling. A number of factors contribute to this possible processing advantage. For mechanically milled powder, particles with varying sizes may lead to easier filling of pores of different sizes. Fine grain sizes provide shorter diffusion paths and much increased densification rate during sintering.

It is obvious that the diffusional processes that mediate sintering also lead to undesired grain growth. The driving force for grain growth also increases, as grain sizes decrease such that the advantage nanophase materials have in sinterability can be partly lost due to concomitant grain growth that destroys the desirable nanoscale grain size. Therefore, consolidation temperature needs to be maintained sufficiently low, and other mechanisms (such as stress

assisted densification) must be invoked to allow full consolidation and retention of nanostructure.

## 2.6.2 Consolidation Pressure

To compensate for the low consolidation temperature the strategy usually adopted is to use hot pressing and forging employing high pressure (of the order of 0.5-1 GPa) to enhance the contribution of plastic deformation and bonding. The high stress enhances the plastic strain controlled pore closure. Also, the stress plays a significant role in stress assisted densification (diffusion) mechanisms. Possible stress effects on deformation and densification can be seen from the established formula for creep, in general,

$$\frac{\partial \varepsilon}{\partial t} = A \sigma^n / RT d^q * \exp(-Q/RT) f(\rho) \quad (3)$$

Where,  $\sigma$  is the applied stress,  $d$  the grain size,  $\partial \varepsilon / \partial t$  the strain rate,  $n$  = the stress exponent,  $q$  the grain size dependent exponent,  $A$ , a coefficient involving diffusivity prefactor, Burger vector, shear modulus etc.,  $Q$  the activation energy for the accommodation process,  $\rho$  the density,  $R$  the gas constant, and  $T$  the temperature. In this expression,  $A$ ,  $n$ ,  $q$ , and  $Q$  can have different values for different creep mechanisms (Nabarro-Herring creep, Coble creep, dislocation climb power law creep etc.), and  $f(\rho)$  accounts for density effects. The equation indicates that the high pressure applied and the strong grain size dependence of creep deformation can contribute significantly to densification by plastic deformation at relatively low temperatures. In addition, the extensive plastic deformation under high stress results in disruption of any continuous surface oxides on powder particles, which may degrade bonding and properties. The

high pressure applied may also have the beneficial effects of slowing down grain growth because of the reduction of free volumes in grain boundaries, which facilitate atomic jump across the boundary.

### 2.6.3 Contamination

Contamination of the powders through oxide formation during mechanical milling and consolidation of powders can be a serious problem. The incorporated oxygen in some cases has deleterious effects on mechanical properties of the compact, and perhaps on consolidation as well. To reduce contamination, all the mechanical alloying and consolidation should be performed under inert atmosphere. The powder should be purchased from the standard vendors with minimum impurity content. It is reasonable to conclude that when processing in argon, the majority of gaseous impurities usually come with the original commercial powders as contamination of the surface layers. However, these powder particles fairly large before and after milling of about  $40\mu$ . The low surface/volume ratio leads to a low impurity concentration in a bulk-averaged analysis of the compact. To reduce metallic impurities acquired during milling, milling media (vial and balls) that match the materials being milled (steel for iron powders) should be used. Alternatively, one can do a first run, after which the tool surfaces will be coated with desired material. Subsequent runs of the same material using such a 'seasoned' vial and balls would suffer a little contamination.

### 2.6.4 Suppression of grain growth

Compared with the grain sizes in as milled powder, grain growth is observed in all consolidation technique. There could be several possible ways for the suppression of runaway grain growth during consolidation. First of all, sinter-forging scheme allows full density processing at relatively low temperatures, significantly below  $0.5T_m$ , resulting in less grain growth than other consolidation methods. Second, a minute amount of impurities picked up during milling, although often below the detection limit, may have also contributed to the success in suppressing grain growth through solute drag or Zener drag mechanism. These trace impurities are uniformly distributed by the milling action, reducing the possibility of abnormal grain growth.

Grain size stability is especially high when a second element, copper is added into iron. In this case additional factors contribute to the retention of nanoscale grain sizes in consolidated composites. First of all, the powder after mechanical milling consists of a super saturated solid solution, with iron and copper alloyed on the atomic scale due to the non-equilibrium nature of the milling process. The solute drag effect, due to the solute atoms segregating to grain boundaries, retards grain growth. Second, upon heating during consolidation, phase separation into f.c.c. copper and bcc iron occurs inside the nanograins or along the abundant grain boundaries. The new grains thus start out with sizes smaller or at least similar to those in the nanocrystalline precursor phase. Third, the resultant two-phase mixture configuration helps to isolate grains and/or domains of the same structure and thereby reduce grain growth boundary migration. In other words, incorporating a second element or phase helps to retain nano phase grain size when reaching full density.

## 2.7 Kinetics of nanocrystalline (metastable) phase transformation

Many metastable phases are found in the nature and also been produced by the recently developed novel materials processing techniques. According to the thermodynamics, there is a possibility for both stable and metastable phases to form. There are two reasons why metastable phases form [25]. These are:

- 1) Metastable phases can nucleate before the stable phases can nucleate, and
- 2) The crystal growth rate of the metastable phase exceeds that of the stable phase.

## 2. 7. 1 Nucleation of the metastable phases:

The free energy hierarchy, the relative magnitude of the driving forces for the possible phase transformations, doesn't tell us which phase is more likely to form under a given set of conditions. It is well known according to the Ostwald step rule (Ostwald 1897) that the first phase to appear will be a metastable phase which has a higher free energy than the stable phase.

The excess free energy of critical nucleus ( $\Delta G^*$ ) can be expressed as:

$$\Delta G^* = (16/13) * \pi * (0.065)^3 * \Delta H_f^* [T_m^2 / (T_m - T)^2] \quad (4)$$

where  $\Delta G^*$  = the excess free energy of critical nucleus,

$\Delta H_f$  = the enthalpy of fusion,

$T_m$  and  $T$  are melting temperature and temperature of cooling ( $T < T_m$ ).

Fig 2.5 shows a schematic illustration of excess free energy for critical nucleus for stable and metastable phases vs. temperature. The condition ( $B < 1$ ) should usually be satisfied because  $\Delta H_f$  approaches  $\Delta G$  at low temperatures and  $\Delta G^*$  for the metastable phase is always less than that of

the stable phase. Therefore, it may generally expected that the nucleation frequency of the metastable phases is larger than that of the stable phase if the under cooling is large enough.

## 2. 7. 2 The crystal growth rate of the metastable phase:

There have been only a few schematic studies of the growth rate. In general, the growth rate can be expressed as a function of the under cooling by the equation (Jackson 1984):

$$S = S_0 (\Delta T)^\beta \quad (5)$$

With  $S_0$  and  $\beta$  ( $1 < \beta < 2$ ) as constants, and  $\Delta T$  is the degree of under cooling.  $S_0$  and  $\beta$  have no physical meaning. However, when  $\beta$  of the metastable phase is larger than that of the stable phase, the growth rate of the metastable phase become larger than that of the stable phase at a under cooling as shown in the Fig 2.6. Such a situation can occur when the stable phase has a faceted solid liquid interface while the metastable phase a molecularly rough interface (Tuckerman and Bechhoefer 1992). In this Figure,  $\beta$  of stable and metastable phases is 1.4 and 2.0 respectively. For  $S_0$ , the value for the metastable phase is three times larger than that of the stable phase.

## 2.8 Mechanical alloying

Mechanical alloying is a powder processing technique that allows production of homogeneous materials starting from blended elemental powder mixtures. The mechanical alloying process was developed in 1966 by John Benjamin and his colleagues at the Paul D. Merica Research Laboratory of the International Nickel Company (INCO) as a part of program to produce a

material combining oxide dispersion strengthening (ODS) with  $\gamma$  precipitation hardening in a nickel based super alloy intended for gas turbine applications [26].

The actual process of M.A. starts with mixing of the powder in the right proportion and loading the powder into the mill along with the grinding medium. This mix is milled for the desired length of time until a steady state is reached when the composition of every powder particle is the same as the proportion of the elements in the starting powder mix. The milled powder is then consolidated into a bulk shape and heat treated to obtain desired microstructure and properties. The important attributes of mechanical alloying are listed in Table 2.3 We will discuss the different parameters involved in the selection of raw materials, type of mill and process variables.

### 2.8.1 Raw materials:

The raw materials used for MA are widely available commercially pure powders that have particle sizes in the range of 1-200  $\mu\text{m}$ . But the powder particle size is not very critical, except that it should be smaller than the grinding ball size. The powders fall into the broad categories of pure metals, master alloys, pre-alloyed powders and refractory compounds. Dispersion strengthened materials usually contain additions of carbides, nitrides and oxides. Oxides are the most common and these alloys are known as oxide dispersion strengthened (ODS) materials. Metal powder can be milled with a liquid medium and this is referred to as wet grinding [27-30]; if no liquid is involved then it is referred to as dry grinding. It has been reported, that wet grinding is a more suitable method than dry grinding to obtain finer ground products because the solvent molecules are absorbed on the newly formed surfaces of the particles and lower

their surface energy. The less agglomerated condition of the powder particles in the wet conditions is also a useful factor. It has been reported that of amorphization is faster during wet grinding than during dry grinding [30].

## 2.8.2 Types of mills

The MA process can be successfully performed in both high energy (attrition type ball mill, planetary type ball mill, centrifugal type ball mill and vibratory type ball mill) and low energy tumbling mills (ball and rod mills). They differ in their capacity, efficiency of milling and additional arrangements for cooling, heating etc. A detailed description of different types of mills available for MA can be found in Ref [31], a brief description is provided below.

### 2.8.2.1 Ball Attritor or Attritor mill

Szigvari introduced this type of mill to industry in 1922 in order to quickly attain fine sulphur dispersion for use in vulcanization of rubber [32]. The illustration of this mill also known as Szigvari attritor, is shown in Fig 2.7. The operation of an attritor is simple. The powder is placed in a stationary tank with the grinding media. The milling is done by the stirring action of an agitator, which has a vertical rotating central shaft with horizontal arms (impellers). Attritors of different sizes and capacities are available. The rotation speed of the central shaft is about 250 rpm (4.2 Hz). This causes the media to exert both shear and impact forces on the material.

### 2.8.2.2 Planetary ball mill

The planetary ball mill is one of the most popular mills used in MA for synthesizing almost all of the materials presented in Fig 2.8. In this type of mill, the milling media have considerably high energy, because milling stock and balls come off the inner wall of the vial (milling tool) and the effective centrifugal force reaches up to twenty times gravitational acceleration.

The centrifugal forces caused by the rotation of the supporting disc and autonomous turning of the vial act on the milling charge (balls and powders). Since the turning direction of the supporting disc and the vial are opposite, the centrifugal forces alternatively are synchronized and opposite. Therefore, the milling media and the charged powders alternatively roll on the inner wall of the vial and are lifted and thrown off across the bowl at high speed (360 rpm), as schematically represented in Fig 2.8.

These are manufactured by Fritsch GmbH in Germany and marketed by Gilson Co., US and Canada. The planetary ball mill owes its name to the planetary like movement of its vials. These are arranged on a rotating support disc and a special drive mechanism causes them to rotate around their own axes.

Even though the disc and vial rotation speed could not be independently controlled in the earlier versions, it is possible to do so in the modern versions. In a single mill one can have either two (pulverisette 5) or four (pluverisette 5) milling stations. Recently a single station mill was also developed (pluverisette 6). Grinding vials and balls are available in eight different materials-agate, silicon nitride, sintered corundum, zirconia, chrome steel, Cr-Ni steel, tungsten carbide and plastic polyamides.

#### 2.8.2.3 Vibratory ball mill

The vibratory ball mill is another kind of high-energy ball mill that is used mainly for preparing amorphous alloys. The vials capacities in the vibratory mills are smaller (about 10 ml in volume) compared to previous types of mills. In this mill, the charge of the powder and milling tools are agitated in three perpendicular directions (Fig 2.9) at very high speed as high as 1200 rpm.

Another type of vibratory ball mill, which is used at the Van der Waals-Zeeman Laboratory, consists of a stainless steel vial with a hardened steel bottom, and a single hardened steel ball of 6 cm in diameter. The mill is evacuated during milling to a pressure of  $10^{-6}$  torr. in order to avoid reactions with a gas atmosphere [33]. Subsequently, this mill is suitable for mechanical alloying of some special systems that are highly reactive with the surrounding atmosphere, such as rare earth elements.

#### 2.8.2.4 Low energy tumbling mill

Tumbling mills are defined as cylindrically shaped shells, which rotate about a horizontal axis. Loads of balls or rods are charged into the mill to act as milling media. The powder particles of the reactant materials meet the abrasive and/or impacting force that reduce the particle size and enhance the solid-state reaction between the elemental powders.

#### 2.8.2.5 Tumbler ball mill

The tumbler ball mills date back to 1876 [34] and are characterized by the use of balls (made of iron, steel or tungsten carbides) milling media. The capacities of these mills are governed by several variables (ratio of mill length to diameter, speed of mill, size of balls, particle size etc.) that should be adjusted and balanced. In these mills the useful kinetic energy can be applied to the powder particles of the reactant material [35] by

- Collision between the balls and the powders
- Pressure loading of powders pinned between milling media and the liner
- Impact of the falling milling media
- Shear and abrasion caused by dragging of particles between moving media
- Shock wave transmitted through cross load by falling media

The tumbler ball mills have been successfully used for preparing several kinds of mechanically alloyed powders. However this kind of low energy may lead to an increase in the required milling time for a complete MA process, it produces homogeneous and uniform powders [36]. In addition, it is cheaper than those of the high-energy mills and can be self-made with lower costs. Moreover, tumbling mills operated simply with low maintenance requirement.

#### 2.8.2.6 Tumbler rod mill

Our current knowledge of the materials that are fabricated by MA has shown that almost all ball milled alloy powders are contaminated with iron, when stainless steel balls and vials are used; this is a natural consequence of the collision between milling media. Therefore, MA method is faced with a serious problem, which has impeded progress. Since the ball-powder-ball collision in a tumbling, planetary or vibratory mills can be the main source of iron contamination, different kinds of mills, in which there is no collision between the milling media should be used.

#### 2.8.3 Process variables

MA alloying is a complex process and hence involves optimizing of a number of variables to achieve the desired product phase and/or microstructure. Some of the important parameters that have an effect on the final constitutions of the powder are:

- Types of mills (e.g., high energy mills and low-energy mills)
- The materials of milling tool (e.g., ceramic, stainless steel, and tungsten carbide)
- Types of milling media (e.g., balls or rods)
- Milling atmosphere (e.g., air nitrogen, and an inert gas)
- Milling environment (e.g., dry milling or wet milling)
- Milling media to powder weight ratio
- Milling temperature
- Milling time
- Milling speed
- Process control reagents (PCR)

:

### 2.8.3.1 Types of mill

As described above (section 2.8.2) there are a number of different types of mills for conducting MA. These mills differ in their capacity, speed of operation, and their ability to control the operation by varying the temperature of milling and the extent of minimizing the contamination of the powders. Depending upon the type of the powder, the quantity of powder and final

constitution required, a suitable mill can be chosen. Specially designed mills are used for special applications. The type of mill and typical sample weight used is given in the Table 2.4.

### 2.8.3.2 Milling container

The material used for the milling container (grinding vessel, vial jar or bowl are some of the other terms used) is important since due to impact of the grinding medium on the inner walls of the container, some materials will be dislodged and get incorporated in to the powder. This can contaminate the powder or alter the chemistry of the powder. If the material of the grinding vessel is different from that of the powder, then the powder may be contaminated with the grinding vessel material. On the other hand, if the two materials are the same then the chemistry may alter unless proper precautions are taken to compensate for the additional amount of element incorporated in to the powder. Hardened steel, tool steel, hardened chrome steel, tempered steel, stainless steel, tungsten carbide-cobalt, tungsten carbide lined steel and bearing steel are the most common types of materials used for the grinding vessels. Some specific materials are used for specialized purposes; these include titanium, sintered corundum, yttria-stabilized zirconia (YSZ), partially stabilized Zirconia + Yittria, sapphire, agate, hard porcelain,  $\text{Si}_3\text{N}_4$  and Cu-Be.

### 2.8.3.3 Ball-to-powder weight ratio

The ratio of the weight of then balls to the powder (BPR), sometimes referred to as charge ratio (CR), is an important variable in the milling process. This has been varied by different investigators from a value as low as 1:1 to as high. Generally speaking, a ratio of 10:1 is most commonly used.

The BPR has a significant effect on the time required to achieve a particular phase in the powder being milled. The higher the BPR ratio, the shorter is the time required. Soft conditions (e.g., low BPR, low speed of rotation, etc.) of M.A. produce metastable phases whereas hard conditions produce the equilibrium phases.

#### 2.8.3.4 Milling atmosphere

The atmosphere of the mill is considered as one of the most important factors during ball and/or rod milling of the elemental powders. It has been shown that [27] very fine powders have relatively large surface area and they are highly reactive not just with  $O_2$  but also with other gases, such as hydrogen and nitrogen.

It has been suggested by Yavari et al., [52] that the amorphization reaction, which takes place in a ball mill between immiscible A-B binary couples with  $\Delta H_{mix} < 0$ , is attributed to the presence of some oxygen (~5 at%) and ternary mixture are found to be miscible with  $\Delta H_{mix} > 0$

#### 2.8.3.5 Process control reagents

The powder particles get cold-welded to each other especially if they are ductile, due to the heavy plastic deformation experienced by them during milling. But true alloying among powder particles can occur when a balance is maintained between cold welding and fracturing of particles. A process control reagent (PCR) (also referred to as lubricant or surfactant) is added to the powder mixture during milling to reduce the effect of cold welding. The PCR can be solids,

liquids, or gases. They are mostly but not necessarily, organic compounds, which acts as surface-active agents. The PCA absorbs on the surface of the powder particles and minimizes cold welding between powder particles and thereby inhibiting agglomeration. The surface active agents absorbed on the particle surface interfere with cold welding and lower the surface tension of the solid material, Since the energy required for the physical process of size reduction is given by,

$$E = \gamma * \Delta S \quad (6)$$

where  $\gamma$  is the specific surface energy and  $\Delta S$  is the increase in the surface area. A reduction in the surface energy results in the use of shorter milling times and/or generation of finer powders. A wide range of PCAs has been used in practice at a level of 1-5wt% of the total powder charge. The most important of the PCAs include stearic acid, hexane, methanol and ethanol. A partial listing of different investigations and their quantities is presented in Table 2.5 [22].

#### 2.8.3.6 Milling time

The time of milling is the most important parameter. Normally the time is so chosen as to achieve a steady state between the fracturing and cold welding of the powder particles. The times required vary depending upon the type of mill used, the intensity of milling, the ball to weight ratio and the temperature of milling. The time of milling has to be decided taking into the consideration the above parameters and the particular powder system. But it should be realized that the level of contamination increases and some undesirable phases form if the powder is

milled for times longer than required. Therefore it is desirable that the powder is milled just for the required duration and not any longer.

#### 2.8.3.7 Milling speed

It is easy to realize that the faster the mill rotates the higher would be the energy input into the powder. But depending upon the design of the mill there are certain limitations to the maximum speed that could be employed. For example, in a conventional ball mill increasing the speed of rotation will increase the speed with which the balls move. Above a critical speed, the balls will be pinned to the inner wall of the vial and do not fall down to exert any impact force. Therefore, the maximum speed should be just below this critical value so that the balls fall down from the maximum height to produce the maximum collision energy.

Another limitation to the maximum speed is that at high speed (or, intensity of milling), the temperature of the vial may reach a high value. This may be advantageous in some cases where diffusion is required to promote homogenization and/or alloying in the powders. But in some cases, the increase in temperature may be disadvantageous because the increased temperature accelerates the transformation process and results in the decomposition of supersaturated solid solutions or other metastable phases formed during milling. Additionally the high temperature generated may also contaminate the powders. It has been reported that during nanocrystalline formation the average crystal size increases and the internal stress decreases at higher milling intensities due to enhanced dynamic recrystallization. The maximum temperature reached is different in different type of mills and the values vary widely.

#### 2.8.3.8 Temperature of milling

The temperature of milling is another parameter in deciding the constitution of the milled powder. Since diffusion processes are involved in the formation of alloy phases irrespective of whether the final product phase is a solid, solution, intermetallic, nanostructure, or an amorphous phase, it is expected that the temperature of milling will have a significant effect in any alloy system. During the formation of nanocrystalline, it was reported that the root mean square (r.m.s.) strain in the material is lower and grain size is greater, when milled at higher temperatures as compared to room temperature.

#### 2.8.4 Mechanism of mechanical alloying

During high-energy milling powder particles are repeated by flattened, cold-welded, fractured and re-welded. When two steel balls collide, some amount of powder is trapped in between them. Typically around 1000 particles with an aggregate weight of about 0.2 mg are trapped during each collision (Fig 2.10). The force of impact plastically deforms the powder particles leading to work hardening and fracture. The new surfaces created enable the particle to weld together and this adds to an increase in particle size. Since in the early stages of milling, the particles are soft (if we are using either ductile-ductile or ductile-brittle material combination), and their tendency to weld together and form large particles is high. A broad range of particle sizes develops, with some as large as three time bigger than the starting particles. The composite particles at this

stage have a characteristic layered structure consisting of various combinations of the starting constituents. With continued deformation, the particles get work hardened and fracture by a fatigue failure mechanism and/or by the fragmentation of fragile flakes. Fragments generated by this mechanism may continue to reduce in size in the absence of strong agglomerating forces. At this stage, the tendencies to fracture predominate over cold welding. Due to the continued impact of grinding balls, the structures of the particles is steadily refined, but the particle size continued to be the same. Consequently, the inter-layer spacing decreases and the number of layer in the particles increase.

After milling for a certain length of time, steady state equilibrium is attained when a balance is achieved between the rate of welding, which tends to increase the average particle size, and the rate of fracturing, which tends to decrease the average composite particle size. At this stage each particle contains substantially all of the starting ingredients, the proportion they were mixed together and the particles reach saturation hardness due to the accumulated strain energy. The effects of various parameters on mechanical alloying are discussed earlier.

## 2.8.5 Application of Mechanical Alloying

Mechanically alloyed materials find applications in a variety of industries. The applications include synthesis and processing of advance materials (magnetic materials, super conductors, functional ceramics), intermetallics, nanocomposites, catalysts, hydrogen storage materials, food heaters, gas absorbers, and also in the modification of solubility of organic compounds, waste management, and production of fertilizers. But the major industrial applications of mechanically alloyed materials have been in the area of thermal processing, energy production, glass

processing, aerospace, and other industries. These applications are based on the oxide dispersion strengthening effect achieved in mechanically alloyed nickel-, iron-, or aluminum based alloys.

## 2.9 Fe-Ni system

The calculated phase diagram for the Fe-Ni system is shown in Fig 2.11. The two elements are close together in the periodic table and are chemically similar, with almost identical electronic structures. The behavior of their alloys could therefore be expected to be quite straightforward. However the behavior of these alloys is complex, due to the fact that iron and nickel are both ferromagnetic transition elements. As shown in Table 2.6. Iron and nickel occupy the end of the first period of transition elements. Both these elements together with Co, show the characteristic properties of this group. This is due essentially due to the fact that the 4s electron shell is occupied without the 3d orbital being completely filled. In the solid state, this leads to a narrow 3d band in which the electrons are mainly localized, together with a high density of states close to the fermi level. This particular electronic structure gives rise to a number of general characteristics in the transition elements such as strong cohesion, relatively high electrical resistivity and variable chemical behavior. In some cases, it also leads to some curious effects such as the appearance of magnetic order, causing either ferromagnetism ( $\alpha$ -Fe, Co, Ni) or antiferromagnetism (Cr, Mn,  $\gamma$ -Fe).

### 2.9.1 Crystal structure of the Fe-Ni alloys

The face-centered cubic phase exists over a wide concentration field, ranging from pure nickel to 27% Ni at room temperature. Below 27% Ni, the number of electrons per atom is no longer

sufficient for the f.c.c. structure to remain the only stable phase, and it is gradually replaced by the body centered cubic lattice. For nickel content greater than 27%, the stability of the f.c.c. structure offers a number of significant advantages. It provides high ductility, enabling the alloy to be rolled down to very small thickness, of the order of 10  $\mu\text{m}$ . The absence of a ductile brittle transition at low temperatures makes it possible to use these materials at cryogenic temperatures (Invar for LNG tankers). Finally, heat treatment can be performed at all temperatures without the complication of phase transformations. This is extremely useful for developing recrystallization textures or exceptional magnetic properties. One of the simplest consequences of the stability of f.c.c. phase in Fe-Ni alloys is that their lattice parameters and densities obey the rule of mixtures over a wide range of compositions, from pure nickel to 40% nickel (Fig 2.12). However, below 40% Ni, the situation becomes much more complicated, since the normal variation of lattice parameter with composition is accompanied by a more unusual and quite unexpected effect of temperature.

## 2.9 2 Electromagnetic properties of Fe-Ni alloys

The Fe-Ni alloys are ferromagnetic through out the range of concentrations, and their original electromagnetic behavior have led to a wide variety of soft magnetic materials. The variations of their electromagnetic characteristics ( $M_s$ , etc,) with parameters such as composition, microstructure and temperature have natural repercussions on their functional properties, particularly on the most commonly used one, the relative permeability  $\mu$ . It is given by

$$\mu = B / (\mu_0 H) \quad (7)$$

where  $B$  is the induction,  $H$  is the field strength and  $\mu_0$  is the permeability of vacuum. In weakly anisotropic materials such as the Fe-Ni alloys, the permeability  $\mu_z$  for the usual case of AC operation can be written as

$$1/\mu_z = ((b + K_u + (3/2gd)) * (1.5)) / A M_s + 16fdl/(\pi * \pi^*) * \rho \quad (8)$$

where  $M_s$  is the saturation magnetization, corresponding to the maximum magnetic flux which the material can support,  $\rho$  is the electrical resistivity which limits the eddy current losses during AC operations and therefore improves the efficiency of electromagnetic energy exchange,  $K_1$  and  $K_2$  are the magnetocrystalline and induced (unidirectional) magnetic anisotropies via which the magnetic structure can be adapted,  $g$  is the magnetostriction, which accounts for the effect of stress  $s$ ,  $b$  is a magnetostatic energy term which takes into account of the effects of precipitates, grain boundaries, etc.,  $f$  is the operating frequencies,  $d$  is the strip thickness,  $l$  is the width of the magnetic domains and  $A$  is a constant.

The simplified relation shows that, in addition to the stability of ferromagnetism ( $M_s$  and  $T_c$ ) four major parameters ( $\rho$ ,  $K_1$ ,  $K_u$ ,  $\lambda$ ) determine the functional magnetic properties of commercial alloys. For high permeability, it can be seen that  $M_s$  and  $\rho$  must be as large as possible and  $K_1$ ,  $K_u$ , and  $\lambda$  as small as possible.

### 2.9.2.1 Ferromagnetism of Fe-Ni alloys

When iron, with 2.2 Bohr magnetons ( $\mu_B$ ), per atom, i.e.,  $M_s = 2.15T$ , and a curie point of  $770^0C$  is added to nickel, which has only 0.6  $\mu_B$  per atom and a curie point of  $358^0C$ , it is to be expected that the saturation magnetization and curie point will be increased and this is indeed observed, as

shown in Fig 2.13 [40]. The fall in curie point beyond 30-40% Fe indicates that the ferromagnetic coupling gradually weakens above this concentration, and it should be noted that this behavior corresponds to the change in sign of the spontaneous volume magnetostriction. The increase in saturation magnetization with iron content is linear up to about 60% Fe, as predicted by the band theory of magnetism. However, the behavior deviates slightly from linearity beyond 50% Fe, and becomes frankly anomalous on approaching the invar composition (64 %Fe). Between 40 and 25% Ni, it is as though not only does the ferromagnetic coupling disappear, but also, at the same time, the magnetization of the material vanishes. This can be due to the tendencies for local anti ferromagnetic coupling. Another possibility is that the magnetic moments decrease at a specific electron concentration [39].

### 2.9.2.2 Electrical resistivity of Fe-Ni alloys

The electrical resistivity increases with temperature and with the presence of irregularities in the crystal lattice (foreign atoms, differences in magnetic moments, etc.,) since these factors disturb the propagation of conduction electrons. The resistivity near room temperature increases rapidly as the iron content increases above 50%, reaching a maximum in the region of the invar composition [40]. This abnormal increase in the resistivity is a consequence of the highly disturbed magnetic state in this range of concentrations.

### 2.9.2.3 Magnetic Anisotropy in Fe-Ni alloys

Equation (8) shows that, neglecting complications due to inevitable eddy currents, the permeability of Fe-Ni alloys depend essentially on two factors. Firstly, microstructural features, such as non-magnetic precipitate particles, grain boundaries, etc., disturb the induced magnetic flux lines, creating magnetostatic energy of density  $b$ . In order to magnetize the material, the magnetizing field must expand this energy. It can be reduced essentially by careful control of the melting, working and heat treatment processes. Secondly the term  $(K_l + K_u + \lambda\delta)$  corresponds to the sum of the different anisotropies in the crystal environment, which exert an influence on the local magnetization of the material [39,40]. In fact ferromagnetic lattices are naturally high anisotropic, and the effect sometimes can be enhanced by external factors such as stresses, magnetic field annealing, recrystallization, etc.

### 2.9.4 High Permeability of 80Ni-20Fe Alloys

In the binary 80Ni-20Fe alloys with around 80% Ni, the magneto crystalline anisotropy  $K_l$  and the magnetostriction do not vanish exactly at the same composition, so that it is not possible to obtain a total anisotropy of zero. Moreover, these alloys have two additional disadvantages. Firstly, their electrical resistivity is only moderate and is insufficient for ac applications. Secondly, the ordering reaction occurs too rapidly for it to be readily controlled during industrial heat treatments. Empirical solutions have been obtained for most of these problems, and consist

in adding a small amount (3-6%) of Cr or Mo, sometimes combined with copper. As expected these elements increase the resistivity (Fig 2.14) and retard ordering but also have more unexpected effects. In particular, they shift the composition, where  $K_1$  falls to zero, and with an appropriate choice for additions it becomes possible to make it coincide with that for the magnetostriction.

In order to make use of these complex behaviors, it is necessary to finally adjust both the alloy chemistry and the heat treatments. In particular the composition is adjusted to determine the resistivity and the value of the magnetostriction, which is little dependent on ordering. Heat treatments are then used to adjust  $K_1$  and  $K_2$ , either to as low a value as possible, or a value tuned to the magnetostriction. The heat treatment cycles involve two stages. High temperature annealing is performed first of all to induce recrystallization and eliminate defects liable to hinder the magnetization process, such as precipitates, dislocations and residual stress, grain boundaries etc. This is followed by holding at a medium temperature ( $\sim 500^0\text{C}$ ) to induce short range order sufficient to bring  $K_1$  to zero (Fig 2.15). Rapid cooling at the end of this treatment minimizes  $K_u$ , which develops only slowly. By combining particular composition with appropriate heat treatments, it is possible to obtain a family of alloys whose range of properties covers the requirement of a wide variety of applications [40].

## CHAPTER 3

### 3. Experimental procedure

#### 3.1 Raw materials

##### 3.1.1 Iron Powders

Electrolytic iron powders supplied by M/S Sudhakar Products Bombay was used.

##### 3.1.2 Nickel Powder

INCO type 123-nickel powder was used. This was produced by carbonyl process.

##### 3.1.3 Binder

Reagent grade anhydrous methyl cellulose powder having methoxy content of 28-32% was used as binder.

##### 3.1.4 Plastisizer

Reagent grade glycerol having density of 1.255-1.260 g/ml at 293K and ash content of not more than 0.02 was used as plastisizer.

## CHAPTER 3

### 3. Experimental procedure

#### 3.1 Raw materials

##### 3.1.1 Iron Powders

Electrolytic iron powders supplied by M/S Sudhakar Products Bombay was used.

##### 3.1.2 Nickel Powder

INCO type 123-nickel powder was used. This was produced by carbonyl process.

##### 3.1.3 Binder

Reagent grade anhydrous methyl cellulose powder having methoxy content of 28-32% was used as binder.

##### 3.1.4 Plastisizer

Reagent grade glycerol having density of 1.255-1.260 g/ml at 293K and ash content of not more than 0.02 was used as plastisizer.

### 3.1.5 Vehicle Medium

Distilled water was used as vehicle medium for the binder solution.

### 3.1.6 Gases

IOLAR-2 grade argon and hydrogen gases were used in the present work.

## 3.2 Preparation of nanocrystalline 80Ni-20Fe powder by mechanical alloying.

The carbonyl nickel and electrolytic iron powders were blended in the ratio of 80Ni-20Fe (wt %) and were milled in a high-energy ball mill to produce nanocrystalline Ni-Fe (4:1) at a disc rotation speed of 450 r.p.m. and disc to vial coupling ratio of 1:2. High Ni-Cr steel vials were first given one trial run so that a thin coating of Ni-Fe (4:1) was formed on the vial as well as high nickel-chrome steel balls. This minimizes the contamination during mechanical alloying. The Ball: Powder ratio was maintained at 5:1. In order to avoid agglomeration wet milling was carried out using acetone as suspending media. The lids of the vials were tightly closed to isolate the system from the atmosphere. After different time intervals samples were taken from the vials for further investigations.

## 3.3 Consolidation of mechanically alloyed 80Ni-20Fe powder.

It is contemplated that nanostructured 80Ni-20Fe powder would be obtained from mechanically alloying process. Consolidation of powders require sintering, which is usually done at a temperature equal to 0.8 T<sub>m</sub> (where, T<sub>m</sub> is the M.P. of the powder material Kelvin). Thus during consolidation of mechanically alloyed powder grain growth would also take place. If proper care is not taken then nanocrystallinity may be destroyed during the process. Thus every effort must be made to choose a processing route, in particular temperature and number of unit steps in such a way that the grain growth is minimum.

The melting points of Ni and Fe are 1276 K and 1808 K respectively. Thus a temperature of about 1400 K would be suitable for sintering of such a powder. The following processing route has been followed to make strip from mechanically alloyed 80Ni-20Fe powder in the present investigation.

M.A. 80Ni-20Fe powder → Slurry making → Casting of “green” strip → Drying → Sintering at 1273 K for 15 min → First hot rolling at 1273 K → Second hot rolling at 1273 K.

It can be noted that the temperature of sintering and hot rolling has been kept below the normal sintering/rolling temperature.

### 3.3.1 Preparation of Green Strips by Slurry Casting Methods

Green strips of M.A. 80Ni-20Fe were prepared by using the batch process of slurry casting method. The slurry composition is given in the Table 3.1

At first, a dry pre-mix of binder and metal powder was prepared and then a solution of glycerol in water was made. This was done to prevent the agglomeration occurring during direct mixing of binder with solvent. Then the premix was mixed with the aqueous

solution of glycerol in a beaker with the help of laboratory stirrer for 30 minutes and homogenous slurry having good flow characteristics was obtained. Mixing of the slurry was done very carefully to reduce the amount of entrapped air bubbles in the cast strips.

The monolithic green strips of M.A. 80Ni-20Fe were prepared by casting the slurry into single stage flat horizontal detachable type metal mold of size 20X40X6 mm. Prior to pouring, the mold was cleaned and dried and then a thin coating of glycerol was applied which acted as releasing agent. After pouring the excess slurry was scraped of the mold by a scraper blade i.e. doctor blade to maintain the uniformity in thickness of green cast strip. The cast strip in the mold was dried in hot air blast for 5 to 10mins. The green strips were finally dried in a hot air oven at 383K for 1hr.

### 3.3.2 Sintering of the green strips

The green strips were sintered in a specially designed furnace. The heating chamber, which was heated by SiC rod, consisted of an INCONEL tube, 750 mm long and 100 mm internal diameter and was closed from one end. The constant temperature zone of length 200 mm existed at the close end of the furnace. The open ends of furnace have 200 mm long cooling chamber, where the sintered strips were cooled under protective atmosphere. Gases were introduced at the closed end of the chamber through a thin INCONEL tube passing through the open end of the chamber. Dried green strips were sintered at 1273K for 15 minutes under dry hydrogen atmosphere. After sintering the strips were slowly transferred into the cooling zone of the furnace where they were cooled under hydrogen atmosphere.

### 3.3.3 Hot densification rolling of the sintered strips

The sintered strips were porous and contained about 45% porosity. Therefore in order to make a fully dense strip these were hot rolled in dry condition. A small hole was made near one end of the sintered strip through which a thin nichrome wire was fastened which was required for pulling the hot strip through the rotating rolls, during hot rolling operation. The sintered strips fastened with a nichrome wire were slowly introduced one at a time into the hot zone of a specially designed reheating furnace interlinked with a two high rolling mill. Reheating for each strip was done at 1273K for 15 min under hydrogen atmosphere. Hot rolling was done on a single stand, non-reversing 2-high rolling mill, having 135 mm diameter rolls rotating at a fix speed of 55 r.p.m. Reheating furnace was interlinked with the rolling mill in such a way that the strips remained in the protective atmosphere up to the roll nip. The set up for the hot rolling of porous sintered strip under protective atmosphere is schematically shown in Fig 3.1 Thickness reduction was achieved by pulling the strip by the wire fastened to it and forcing the hot strip to pass through the rotating rolls, set at predetermined roll gap. Soon, after rolling, the strips were cooled in a bed of fine graphite chips to prevent internal oxidation of the strip caused by the interconnected pores present in it. No annealing was done after hot rolling.

## 3.4 Electron Microscopy

### 3.4.1 Transmission Electron Microscopy

For this purpose, suitable sized pieces of hot rolled 80Ni-20Fe were cut from the rolling plane section and it was hot mounted. It was subjected to grinding in such a way to avoid grain coarsening. For that it was intermittently cooled in water. The metal so obtained is now having thickness approximately 0.4 mm is mechanically polished on emery paper (No 1-3) to 0.2 mm. Since the material was brittle, it was carefully cut into pieces and its sharp corners are polished to make it nearly circular. The final size of the sample is 3 mm diameter. In the last stage, it was further thinned down by electropolishing before examination under Transmission Electron Microscope (TEM) [42].

The mechanically polished samples were further thinned down to the extent of electron transparency using twin jet electro-polishing unit at 80 V. An electrolyte containing 10% (by volume) perchloric acid and 90% acetic acid was used. The bath temperature was maintained at 10 °C. All TEM work was carried out in a JOEL JEM-2000FX microscope at 160 kV.

### 3.4.2 Scanning Electron Microscopy

Powder morphology of M.A. 80Ni-20Fe was observed under a JOEL JSM 840A, Scanning Electron Microscope (SEM). The metal powder morphologies were observed by dispersing the powders with acetone on finely polished brass stubs prepared especially for this purpose. Sample preparation for the microstructural studies consisted of standard emery paper polishing followed

by fine cloth polishing with  $0.3\mu\text{m}$  alumina abrasive particles in suspension with water. The surface of thin film was parallel to the plane containing longitudinal and transverse directions.

### 3.5 X-ray diffraction.

Powder samples were taken out of planetary ball mill after different time intervals, and were characterized using X-ray diffraction technique. The instrument used was Seifert, ISO-DEBYFLEX 2002 diffractometer with copper target. The tube was operated at 30kV and 10 mA. The radiation used was  $Cu K\alpha$  having wavelength of 1.540598 Å. the scanning rate in the X-ray powder diffraction was kept  $2^0/\text{min}$  and  $0.3^0/\text{min}$ .

### 3.6 Grain size determination of M.A. powders

The grain sizes of the powder samples were determined by using “PEAKOC” software. The details about this software are as follows:

#### 3.6.1 PEAKOC

“PEAKOC” is a general profile fitting computer program written in C++. It is particularly suitable for the INEL CPS detector data as it runs with the INEL data format and performs CPS calibration (files). But it can treat any other raw data in ASCII format too (from a Bragg Brentano setting for instance). Peakoc allows fitting peak-by-peak diffractogram under windows. Six peak shapes are proposed: Gaussian, Lorentzian, Pearson VII, Voigt, Pseudo-Voigt and

Split-Pseudo-Voigt. “PEAKOC” is able to perform background removing, smoothing or  $K\alpha_2$  stripping.

### 3.6.2 Procedure for Analysis

The data collected from the diffractometer was converted into the required format for the software. The X-ray diffraction patterns were fitted with a Gaussian function convoluted with an asymmetric function using the “PEAKOC” software for diffraction. The whole pattern was fitted in one step along with a parabolic varying background. A non-linear least square-fitting algorithm was used to minimize the residuals. Usual correction for the  $q$ -dependent part of the diffraction pattern was applied. The effect of diffraction of  $K\alpha_2$  line is removed with the correction for the instrumental broadening. Both the profile shape parameters (viz. peak position  $2 q$ , maximum intensity  $I$ , half width  $w$  and the  $pV$  mixing parameter  $h$ ) along with the background were refined simultaneously.

The grain size was calculated using Gaussian function and pseudo-Voigt function. The PEAKOC software gives the values have  $2\theta$  and full width at half maximum (FWHM). In this value Si standard value of FWHM was eliminated by the approximation as follows:

$$B = (W^2 - W_s^2)^{0.5} \quad (9)$$

where  $B$  is the full width at half maximum after suitable correction,  $W$  is FWHM of the sample under consideration and  $W_s$  is FWHM of the standard, i.e. Silicon in the present case.

The value of B thus obtained is fed in the Scherrer's formula, to find the value of crystallite size as follows:

$$D = (K\lambda)/BCos(\theta) \quad (10)$$

where K is Scherrer's constant,  $\lambda$  is wavelength of Copper  $K\alpha$  radiation,  $\theta$  is half the value of  $2\theta$  in radians.

### 3.7 Laser particle size analysis

FRITSCH PARTICLE SIZER ANALYSETTE 22 was used to determine the particle size of pure electrolytic iron, pure carbonyl nickel and 30 hours ball milled 80Ni-20Fe powder. Measurement duration was of 20 scan in each of the above case.

### 3.8 Density Measurement

Apparent density of the green strip, sintered M.A. 80Ni-20Fe and hot rolled strips were calculated by measuring all the three dimensions, i.e., length, breadth, and thickness and mass.

### 3.9 Magnetic characterization

पुस्तकालय केन्द्र कर्पोरेशन  
भारतीय प्रौद्योगिकी संस्थान कानपुर  
141906  
अवाप्ति क्र. No. A

Magnetic saturation curve and Curie temperature were determined by Vibrating Sample Magnetometer (VSM), model 155 (Fig 3.2 and Fig 3.3) [43]. A sample of 3 mm diameter was cut from the hot rolled M.A. 80Ni-20Fe strip. The sample was fixed in a sample holder, which is kept at the center of the region between the pole pieces of the magnet. A slender vertical sample

rod connects the sample holder with a transducer assembly located above the magnet, which in turn, supports the transducer assembly by means of sturdy, adjustable support rods.

The transducer converts a sinusoidal ac drive signal, provided by an oscillator/amplifier circuit located in the console, into a sinusoidal vertical vibration of the sample rod, and the sample is thus made to undergo a sinusoidal motion in a uniform magnetic field. Coils mounted on the pole pieces of the magnet pick up the signal resulting from the sample motion. This ac signal at the vibration frequency is proportional to the magnitude of the moment induced in the sample. However, it is also proportional to the vibration amplitude and frequency. This being the case, moment readings are taken by measuring the amplitude of the signal.

# Chapter 4

## 4. Result and discussion

4.1 Size, size distribution and shape of the starting nickel and iron powders, and mechanically alloyed 80Ni-20Fe powders.

Fig 4.1a and 4.1b show the particle size histograms of starting carbonyl nickel and electrolytic powders respectively obtained from sieve analysis. It can be seen that about 85 wt % nickel powder are of size <400 mesh, while for iron powder only 50 wt% is below 400 mesh.

Fig 4.2a, 4.2b and 4.2c show the particle size distribution of carbonyl nickel, electrolytic iron powders, and mechanically alloyed 80Ni-20Fe powders milled for 30hrs respectively, obtained from Fritsch Particle Sizer Analysette model 22. The interpolated particle size data are tabulated in Table 4.1. The values of  $d_5$ ,  $d_{50}$  and  $d_{95}$  for nickel, iron, and M.A. 80Ni-20Fe powder are given in Table 4.2. It is interesting to note that the  $d_{50}$  values of nickel, iron and 80Ni-20Fe are 9  $\mu\text{m}$ , 89  $\mu\text{m}$  and 4  $\mu\text{m}$  respectively. It is evident that the mean particle size after 30hr milling has been decreased to 4 $\mu\text{m}$ , which is even smaller than the mean particle size of starting nickel powder, which was about 9 $\mu\text{m}$ .

Fig 4.3a and 4.3b show the SEM photographs of nickel powder and iron powder respectively. The shape of nickel powder is more or less spherical, whereas that of iron is irregular.

Fig 4.3c and 4.3d show the SEM photographs of M.A. 80Ni-20Fe powder (milling time = 30hr). It can be noted that the shape of the M.A. powder is platelet or flaky type.

## 4.2 Phase Identification in M.A. 80Ni-20Fe

X-ray diffraction pattern of M.A. 80Ni-20Fe (Fig 4.4 to 4.7) show predominantly three peaks at  $44.6^\circ$ ,  $51.9^\circ$ , and  $76.5^\circ$  (in order of decreasing intensity). On comparing these  $2\theta$  values with all the standard of compounds of Ni, Fe and oxygen (Ni, Fe, Fe.Ni, FeNi<sub>3</sub>, FeO, Fe<sub>2</sub>O<sub>3</sub>, and NiO) it was concluded that no oxide peaks were present indicating absence of any substantial quantities of oxide. The predominant peak in the XRD is at an angle of  $44.6^\circ$  which coincides with 100% intensity of pure Ni ( $44.507^\circ$ ) [44] pure Fe ( $44.712^\circ$ ) [45], Fe.Ni ( $44.684^\circ$ ) [46] and FeNi<sub>3</sub> ( $44.316^\circ$ ) [47], since they all have highest intensity very close to the observe peaks, thus peaks with lower intensity were used to arrive at the phase composition of the system. The other two observed peaks at  $51.9^\circ$  and  $76.5^\circ$  were found to be present only in FeNi<sub>3</sub> system. Hence it was concluded that the system is predominantly solid solution of Fe in Ni. FeNi<sub>3</sub> is essentially a solid solution of Fe in Ni solid phase (though minor quantities of NiFe<sub>3</sub> and Fe.Ni can not be ruled out). The values of  $2\theta$ , intensity and plane of reflection as given in the standard are indicated for each peak in the XRD (Fig 4.4 to 4.7).

## 4.3 Progressive variation of crystallite size with time of milling

Another interesting observation from the Fig 4.10 is that the crystallite size after milling for as small period as 5 min is of the order of 50 nm, which itself is in the nano scale range. This is very strange observation and it was decided to investigate the crystallite size of starting Ni and Fe powder.

#### 4.4. Crystallite size of the starting powder

In order to determine the exact crystallite size of the starting powder it was decided to take two sets of standards one for Fe and another for Ni, prepared by Ni and Fe standards. By sintering of respective loose powders in a porcelain refractory boat at 1373K for one hour under H<sub>2</sub> atmosphere. This resulted in coarse gram size specimen of respective metals. The X-ray diffraction of the starting and the standard for Ni and Fe powder are given in Figure 4.11 to 4.14.

It can be seen from Fig 4.13 and Fig 4.14 that the diffraction data for Fe contain its XRD pattern a lot of noise. It was decided that since Fe is in small quantity (20 wt%) in our investigation, and contains a lot of noise, not to use this data for crystallite size determination. The crystallite size of the starting Ni was determined by fitting Gaussian profile shape function as given in Fig 4.15 and Fig 4.16. It is curious to note that on sintering the loose powder of nickel not only do the broadening decreases but also K $\alpha_1$  and K $\alpha_2$  peaks can be separately resolved (Fig 4.12). The crystallite size for the starting powder of nickel was measured to be 51nm. Hence the starting nickel powder itself is of nano size range, which indicates the observation, made on 5 min M.A. 80 Ni-20Fe. It appears that the crystallite size of the Ni powder prepared by the decomposition of nickel carbonyl is itself of nano size range.

## 4.5 Properties of hot strip prepared from the M.A. 80Ni-20Fe powders

### 4.5.1 Density of the strip prepared from M.A. 80Ni-20Fe at various stages of processing

The apparent density of the green strip, sintered strip and hot rolled strip prepared from M.A. 80Ni-20Fe are given in Table 4.6. The densification parameter for the sintering of M.A. 80Ni-20Fe powder at 1273K for 15 min can be calculated as follows:

$$\begin{aligned}\text{Densification Parameter} &= (\rho_{\text{sinter}} - \rho_{\text{green}}) / (\rho_{\text{TD}} - \rho_{\text{green}}) * 100 \quad (11) \\ &= (3.76 - 2.84) / (8.697 - 2.84) * 100 \\ &= 15.7\%\end{aligned}$$

After second hot rolling step, the density of the strip comes out to be 70% of the theoretical. It was found that the strip cracked during second hot rolling.

### 4.5.2 Crystallite size of the hot rolled (H.R.) 80Ni-20Fe Strip

The microstructure of 80Ni-20Fe strip was studied under Transmission electron Microscope. Fig 4.17a to Fig 4.17f show the bright field images of the TEM specimen of our material. As can be seen the specimen is not uniformly thin, which is seen as dark regions in the images. Sub grain structure in the form of forest of dislocation is seen which are low angle grain boundaries. Prior

to hot rolling of the M.A. 80Ni-20Fe the strip was heated at 1273 K. However, at the time of actual hot rolling, the temperature of the strip would be less than 1273 K, because of time taken in transferring the specimen from hot zone to the roll nip and also because of the quenching of strip specimen by relatively cold rolls. Hence actually the strip is being warm rolled. Observations on the TEM micrograph Fig 4.17 reveal an approx estimate grain size of 120 nm. It is interesting to note that even after exposure of the M.A. 80Ni-20Fe to a temperature of 1273K for 45 min (in three parts of 15 min each) reveal crystallite size in the range of 100 nm. Select area diffraction was performed on the specimen and corresponding diffraction pattern are given in the Fig. 4.18a to Fig. 4.18f.

#### 4.5.3 Magnetic properties of the hot rolled 80Ni-20Fe strip

Magnetic properties of consolidated 80Ni-20F were determined using Vibrating Sample Magnetometer (VSM), model 155. Focus was centered mainly on determination of Curie temperature of consolidated 80Ni-20Fe and hysteresis curve. These are described as follows:

##### 4.5.3.1 Determination of Curie temperature of 80Ni-20Fe

Fig 4.21 shows the temperature dependence of magnetizations for HR M.A. 80Ni-20Fe under a heating rate of 3K/min. It is seen that the magnetization remains more or less constant till it reaches the Curie temperature. The obsereve value of Curie temperature is found to be approx 525°C. The Curie temperature for nickel, the temperature at which the change from ferromagnetic to paramagnetic occurs is affected by numerous factors, including the prior

mechanical and thermal treatment of the specimen, the nature and the amount of the impurities present, and the method of determination. The Curie point for high purity nickel occurs between 350 C and 360 C [8]. Most alloying elements lower the curie point of nickel but cobalt and iron are exceptions, which increase Curie temperature. The increase in the Curie temperature could be due to the additions of 20 wt% iron in pure nickel. Another factor that could have resulted in increase in Curie temperature is the nano crystallite size as also reported by E. Jartych et al [9] for Ni-Fe.

Figure 4.22 show the field dependence of magnetization for 80Ni-20Fe at room temperature. It can be observed that saturation in magnetization is reached on application of magnetic field greater than 0.4 Tesla. Beyond this any increase in the applied magnetic field does not increase magnetization .The value of saturation magnetization is evaluated to be 6 emu/g. The sample weight was 1.40g.

## 5. Conclusions

- 1) It has been possible to produce NC 80Ni-20Fe powder from commercially carbonyl nickel and electrolyte iron powder. The predominant phase formed is nickel rich solid solution.
- 2) The crystallite size decreases with milling time. The rate of decrease of crystallite size is very rapid between 5min-12hr milling time. Beyond this milling time, the crystallite size is more or less constant with respect to milling time. A value of 30 nm crystallite size was obtained after 30hr milling time.
- 3) The crystallite size determined by line X-ray boarding of the peak corresponding to the plane (200) is consistently smaller than that determined from the peaks corresponding to (111) plane.
- 4) It has been possible to hot roll the sintered strip prepared from 30hr-milled M.A. 80Ni-20Fe powders to about 55% thickness reduction at 1273K. The total time for which the material was kept during processing i.e. sintering stage and preheating prior to hot rolling was about 45 minutes. The hot rolled strip contained about 30% porosity.
- 5) The crystallite size obtained in the hot rolled strip was found to be 120 nm.
- 6) The Curie temperature was observed to be 525°C.

## References

1. Brian H. Pandya, "Nanotechnology Workforce Pipeline Challenges – A Current Assessment and The Future Outlook," report to *ASME International*, 2001, p. 5
2. Mindy N. Ritter and Thomas Abraham, "Nanostructured Materials: An overview and Commercial Analysis", *Intl. J. of Powder Metallurgy*, 1998, vol.34, no.6, p.33-35.
3. Bernard H. Kear and Ganesh Skandan, "Overview: Status and Current Developments in Nanomaterials", *Intl. J. of Powder Metallurgy*, 1999, vol.35, no.7, p.35-36.
4. R.P. Andres, R.S. Averback, et al., *J. Mater. Res.*, 1989, 4, p.704
5. B.H. Kear, et al., Research Opportunities for Materials with Ultra fine Microstructures, *National Academy*, 1989, vol. NMAB-454.
6. H. Gleiter, *Prog. Mater. Sci.* 1989, 33, p. 223-315.
7. G.C. Hadjipanayis and R.W. Siegel, (ed.), *Nanophase Materials: Synthesis, Properties, Applications*, Kluwer, 1994.
8. R. W. Siegel, In *Encyl. Appl. Phys.*, G.L. Trigg (eds.) VCH, 1994, vol. 11, p.173.
9. H. Gleiter: in 'Deformation of polycrystals: Mechanism and microstructures', (ed. N.Hansen et al.), 1981, Roskilde, Denmark, 15-21.
10. C. Suryanarayana, " Nanocrystalline materials", *Intl. Mater. Rev.*, 1995, vol. 40, no. 2, p.41-55.

11. R.W. Siegel, "Synthesis and properties of nanophase materials", *Mater. Sci. and Eng.*, A168, 1993, p. 189-197.
12. C. Suryanarayana and C.C. Koch, " Nanostructured materials", in 'Non-equilibrium processing of materials', (ed. C. Suryanarayana), 1999, Pergamon, p. 313-334.
13. Xue-Dong Liu, "Microstructure of nanocrystalline materials synthesized by amorphous crystallization", *Mat. Trans.*, JIM, 1998, vol. 39, no.8, p. 783-784.
14. C. Suryanarayana and F.H. Froes, "Nanocrystalline Metals: A Review", in 'Physical Chemistry of Powder Metals Production and Processing', (ed. W. Murray Small); TMS, 1989, p.282-285.
15. H.J. Hofler, et al., "Processing of nano-grained materials", *Mater. Sci. Eng. A166*, 1993, p. 169-177.
16. X.D. Liu, et. al., "The Hall-Petch Relationship in Nanocrystalline Materials", *Mat. Trans.* JIM, 1997, vol. 38, no. 12, p. 1033-1039.
17. D.D. Beck, and R.W. Siegel, *J. Mater. Res.*, 1992, vol.7, p.2840.
18. M.E. McHenry and D.E. Laughlin, " Nano-scale Materials Development for Future Magnetic Applications", *Acta mater*, 2000, vol. 48, p. 223-238.
19. M.J. Mayo, et al., "Processing of nanocrystalline ceramics for application in super plasticity", *Mater. Sci. Eng.*, A166, 1993, p. 145-159.
20. S. Bhaduri and S.B. Bhaduri, *JOM*, 1998, 50 (1), p.44.
21. K. Niihara, *J. Ceram. Soc.*, Japan, 1991, vol. 99, p. 974.
22. E. Ma, "Consolidation and mechanical behavior of nanophase iron alloy powders prepared by mechanical milling", *Powder Metallurgy*, 2000, vol. 43, no 4, p. 306-309.

23. E. Ma, and L. He, "Nanophase Fe alloys consolidated to full density from mechanically milled powders", *J. Mater. Res.*, 2000, vol. 15, no. 4, p. 904-911.
24. E. Ma, and L. He, "Full-density nanocrystalline Fe-29Al-2Cr intermetallic consolidated from mechanically milled powders", *J. Mater. Res.*, 1996, vol. 11, no. 1, p.72-79.
25. Keiichi N. Ishihara, " Thermodynamics and Kinetics of Metastable phase transformation", in 'Non-equilibrium processing of materials', (ed. C. Suryanarayana), 1999, Pergamon, p. 12-18.
26. M. Sherif El-Eskandarany, in "Mechanical Alloying for Fabrication of Advanced Engineering Materials", 2001, Noyes Publishing, NY, USA, p.1-33.
27. K. Okada, et al., *J. of Mater. Sci. Lett.*, 1992, vol. 11, 862-864.
28. G. Nicoara, and M. Nogues, et al., *Mater. Sci. Forum*, 1997, 235-238: 145-150.
29. A. Bellosi, et al., *Mater. Sci. Forum*, 1997; 235-238, 255-260.
30. B.P. Dolgin, et al., "J. of Non-Crystalline Solids", 1986, 87, 281-189.
31. C. Suryanarayana, In: "Powder Metal technologies and Applications", *ASM Hand book*, vol. 7, Materials Park, OH, ASM International, 1998, p. 80-90.
32. P.S. Gilman and J.S. Benjamin, "Ann. Rev. Mater. Sci.", 1983, 13:279.
33. H. Bakker, et al., *Prog. Mater. Sci.*, 1995, 39:159.
34. C. Suryanarayana, "Mechanical Alloying", *Prog. In Mat. Sci.*, 2001, 46, 1-184.
35. A.F. Taggart, Handbook of Mineral Dressing: Ores and Industrial Minerals, John Wiley & Sons Inc., NY, 1927.
36. El-Eskandarany, M.S., *J. Alloys Comp*, 1999, 284:295.
37. El-Eskandarany, M.S., *J. Alloys Comp*, 1999, 284:295

38. H. Zhang and R.M. German, "Sintering MIM Fe-Ni Alloys", *Intl. J. of Powder Met.* 2002, vol. 38, no. 1, p. 51-54.

39. Samuel J. Rosenberg, In: "Nickel and Its Alloys", *National Bureau of Standards Monograph* 106, 1968, p.22-26.

40. G. Couderchon and J.L. Porteseil, "Some properties of nickel rich commercial Fe-Ni alloys", in 'The iron-nickel alloys', (eds. G. Beranger et al.,), 1996, Lavoisier, NY, p. 29-58.

41. Manual for laboratory planetary type ball mill, Fritsch, Pulverisette 5.

42. P.J. Goodhew, "Specimen preparation in material science", 1973, p.71.

43. Manual for Vibrating Sample Magnetometer, Model 155.

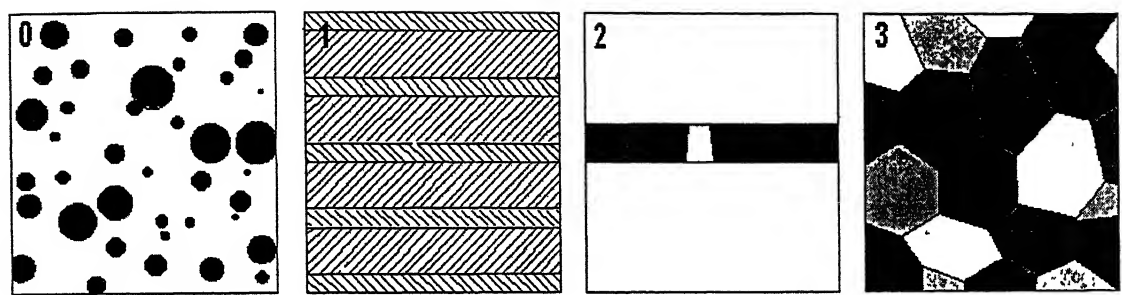
44. Carturan. G et al., Materials Letters, 7, 47 (1988)

45. Swanson et al, Natl. Bur. Stand. (U.S). Circ. 539. IV, 3

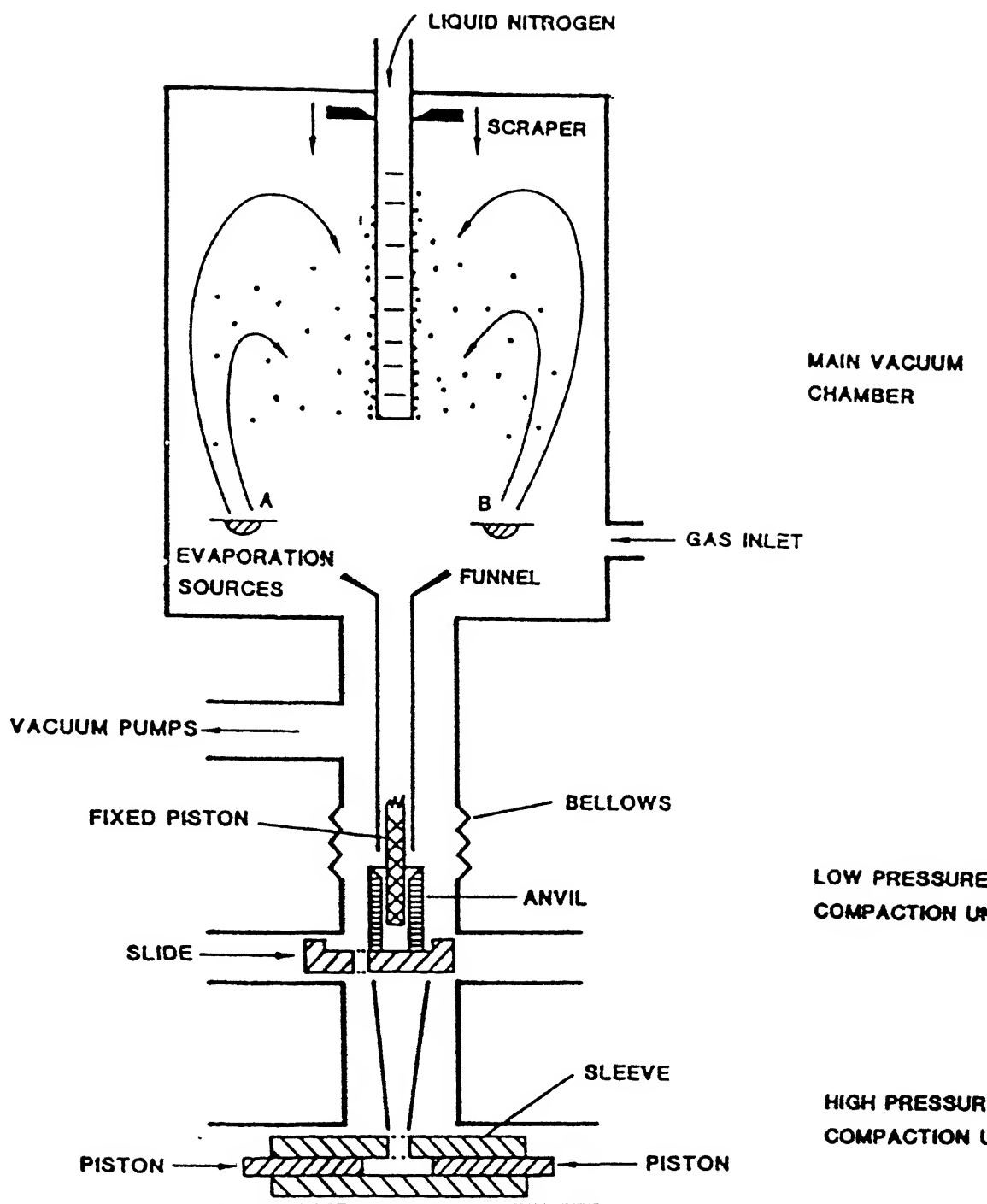
46. Keller. L., Rask. J. Buseck, & P. Arizona State. ( Personal Communication, Tewari, A.)

47. Williams. K., Am. Mineral. 45. 450 (1960)

# FIGURES

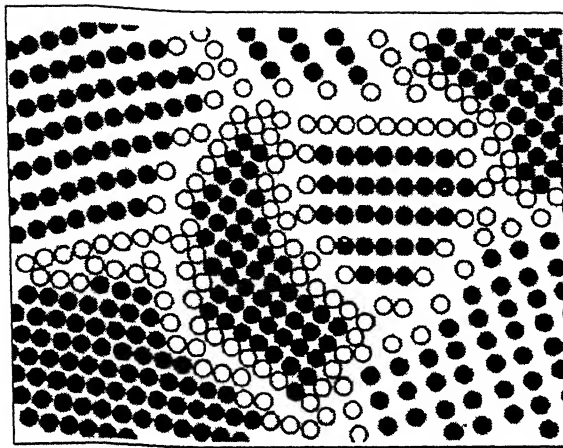


2.1 Schematic representation of four types of nanocrystalline materials (after Siegel 1994).

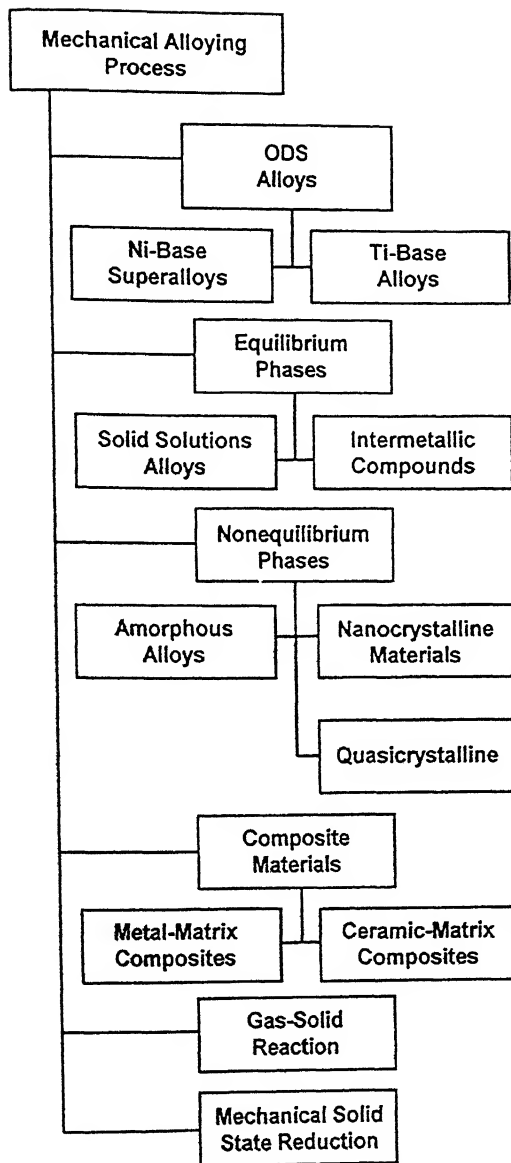


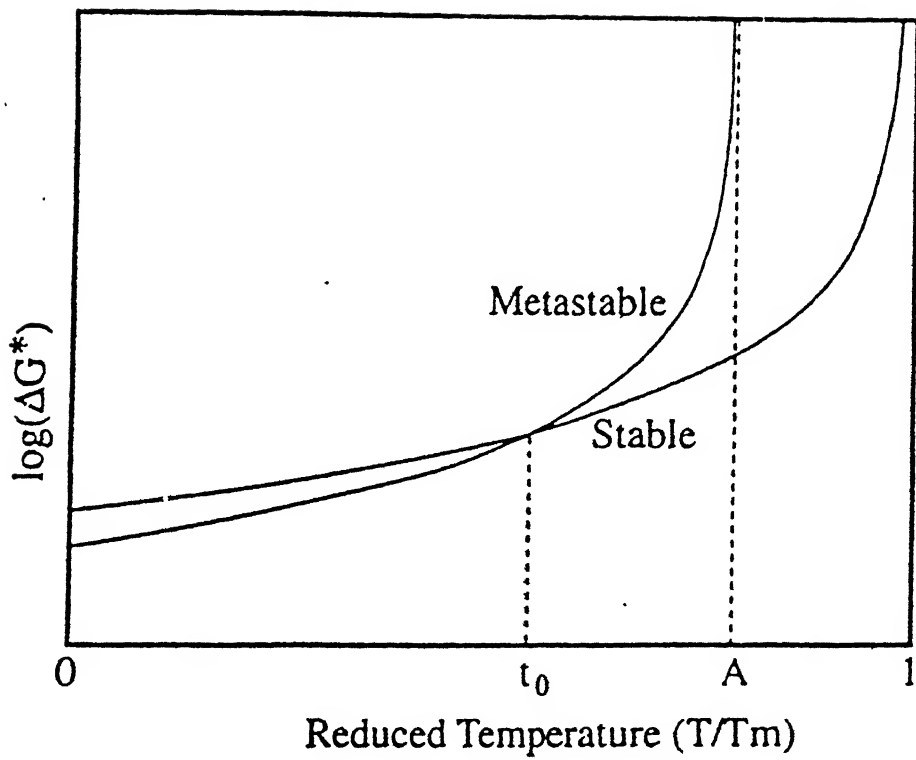
2.2

Schematic representation of a gas condensation chamber for the synthesis of nanocrystalline materials (after Siegel 1990).



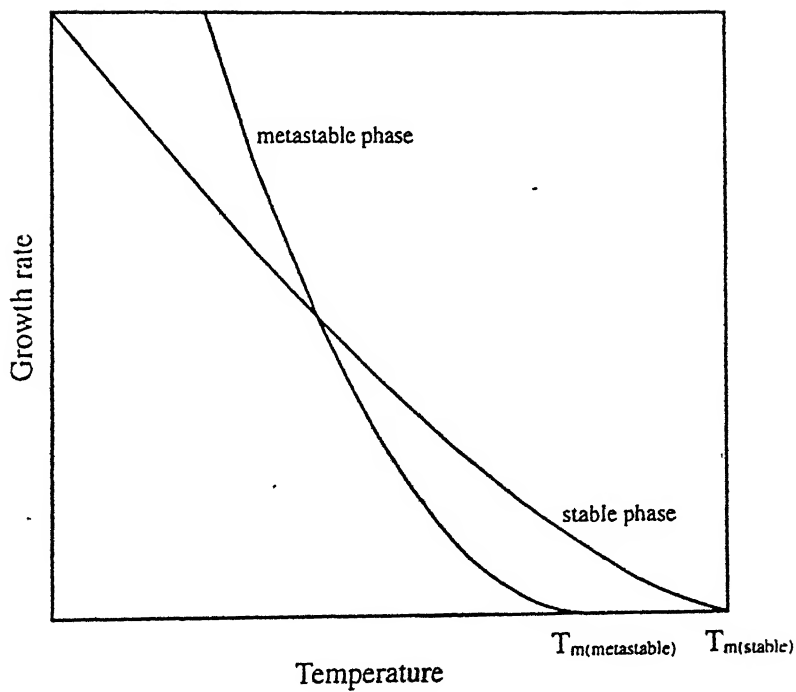
2.3 Schematic representation of an equiaxed nanocrystalline metal distinguishing between the atoms associated with the individual grains (filled circles) and those constituting the grain boundary network (open circles) (after Gleiter 1989)





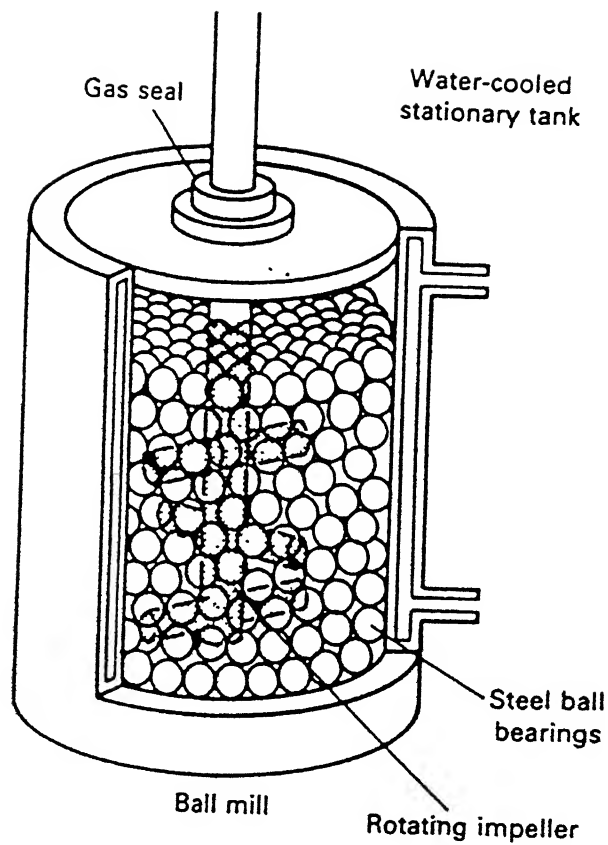
2.5

Schematic illustration of excess free energy for critical nucleus for stable and metastable phases vs. temperature.

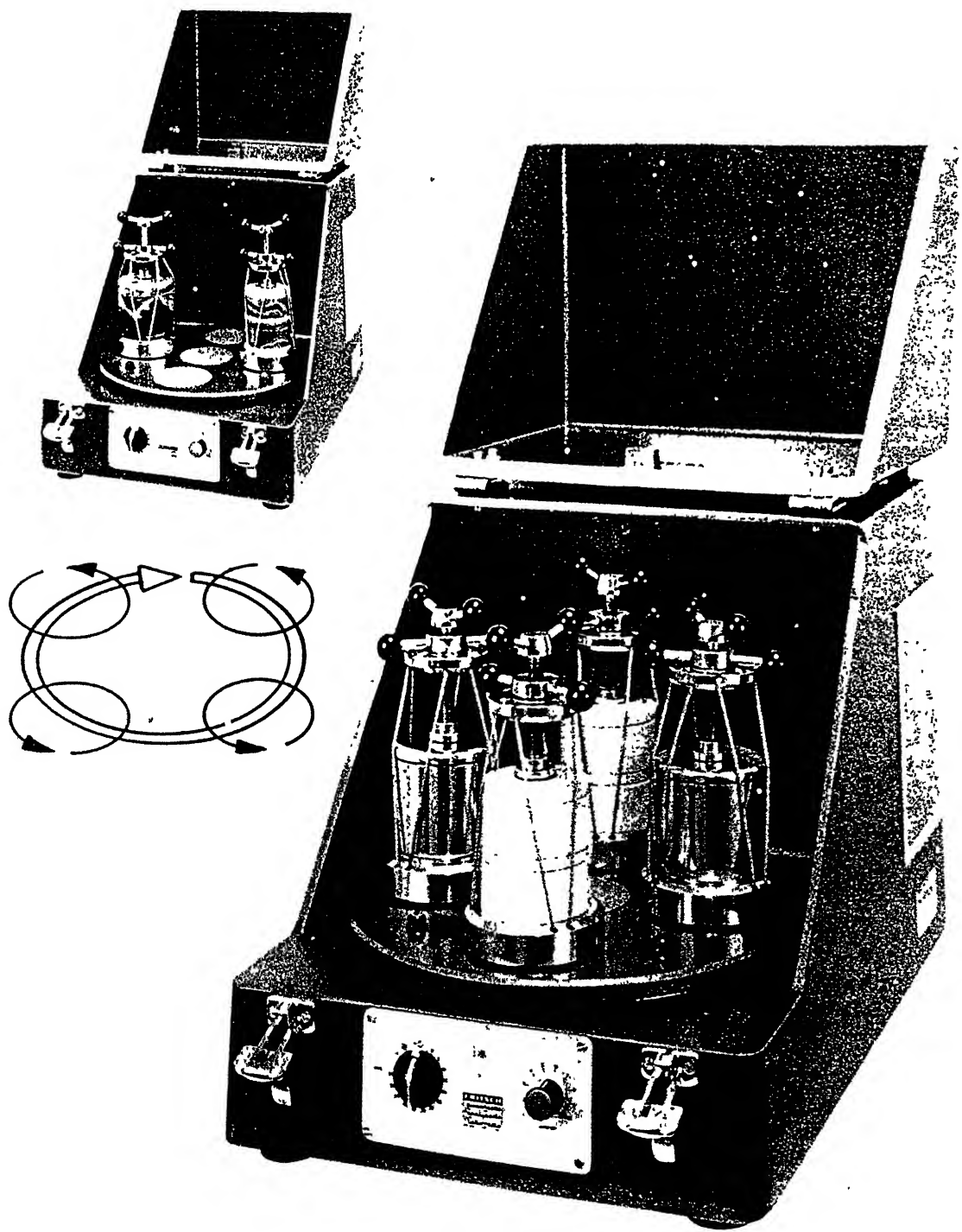


2.6

Hypothetical relation of the growth rate for both stable and metastable phases. In this figure,  $\beta$  of stable and metastable phases is 1.4 and 2.0, respectively. For  $S_0$ , the value for the metastable phase is three times larger than that of the stable phase.

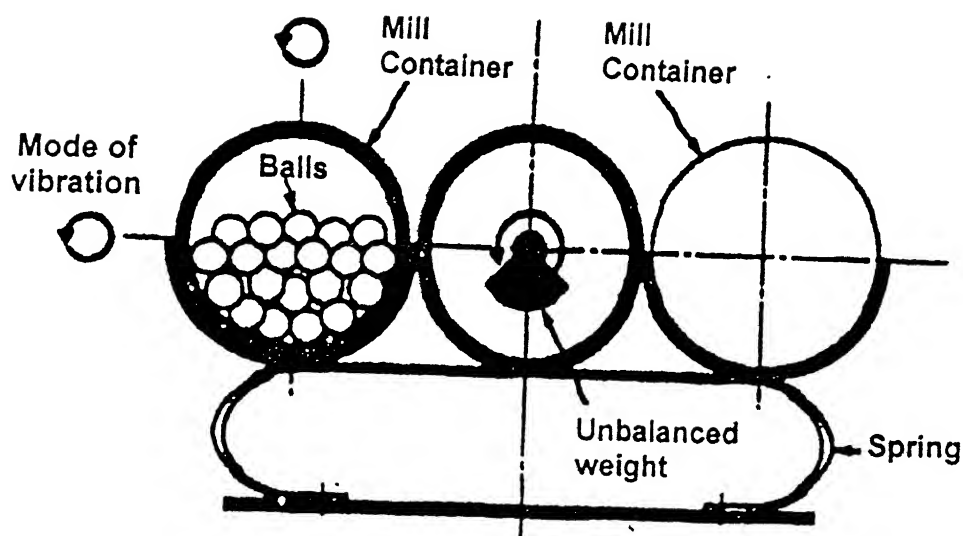


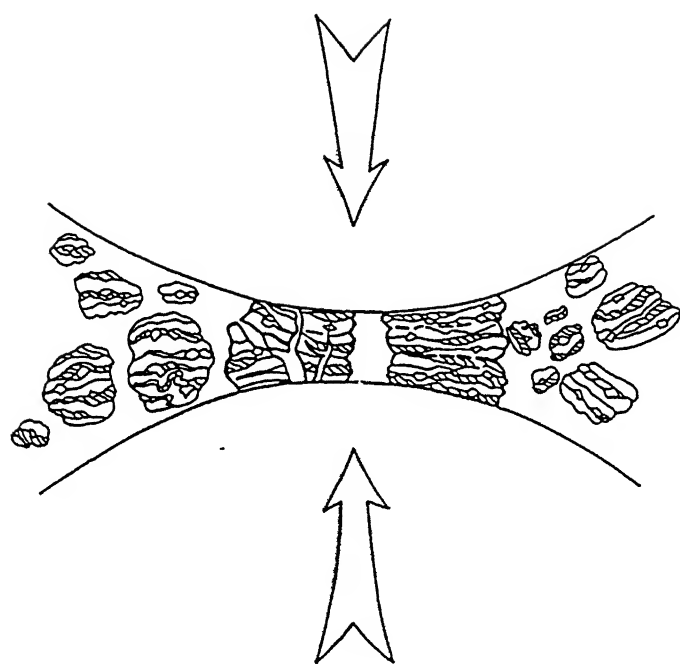
2.7 Szigvari attritor ball mill, the ball is charged by impellers radiating from a rotating vertical shaft, which rotates at speed up to 250 rpm. (After Gilman *et al.*)



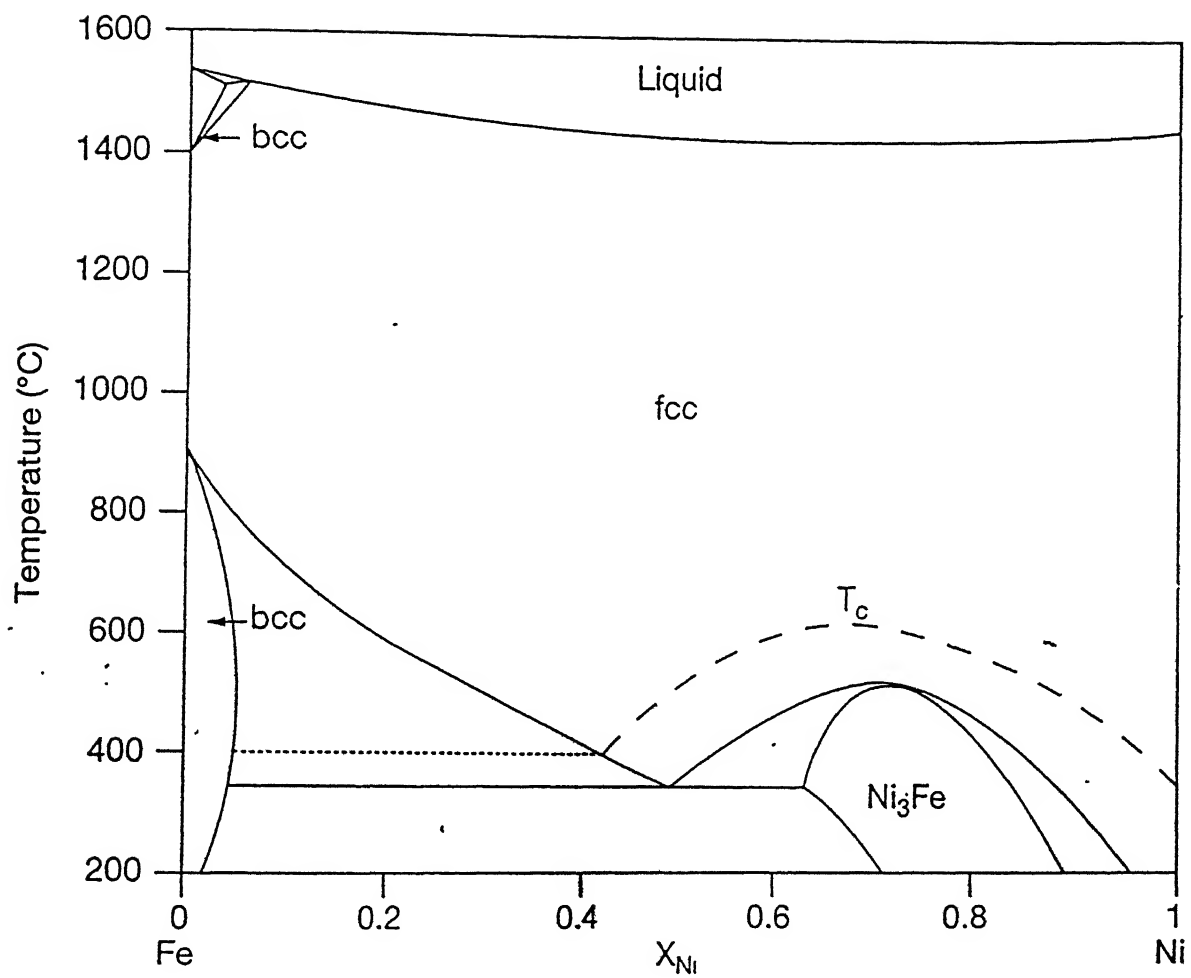
2.8

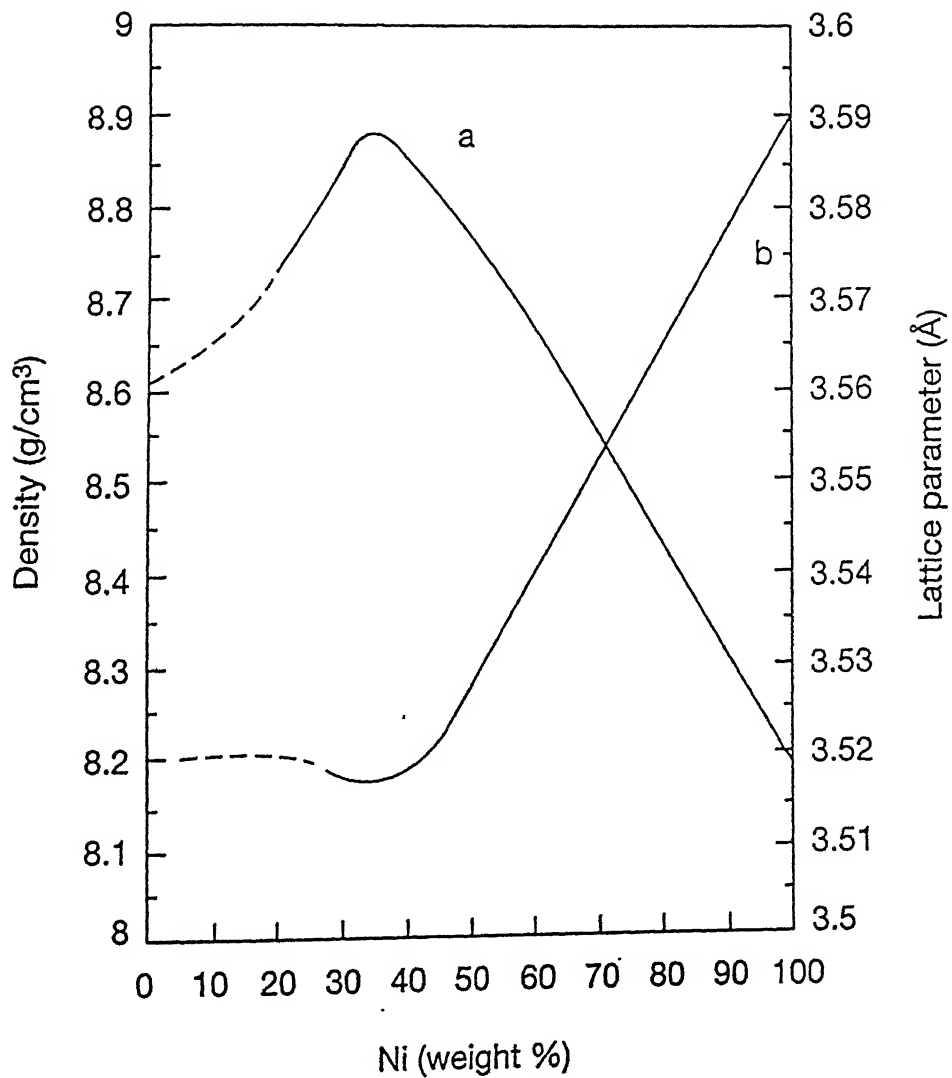
Schematic drawing of a high-energy planetary ball mill.





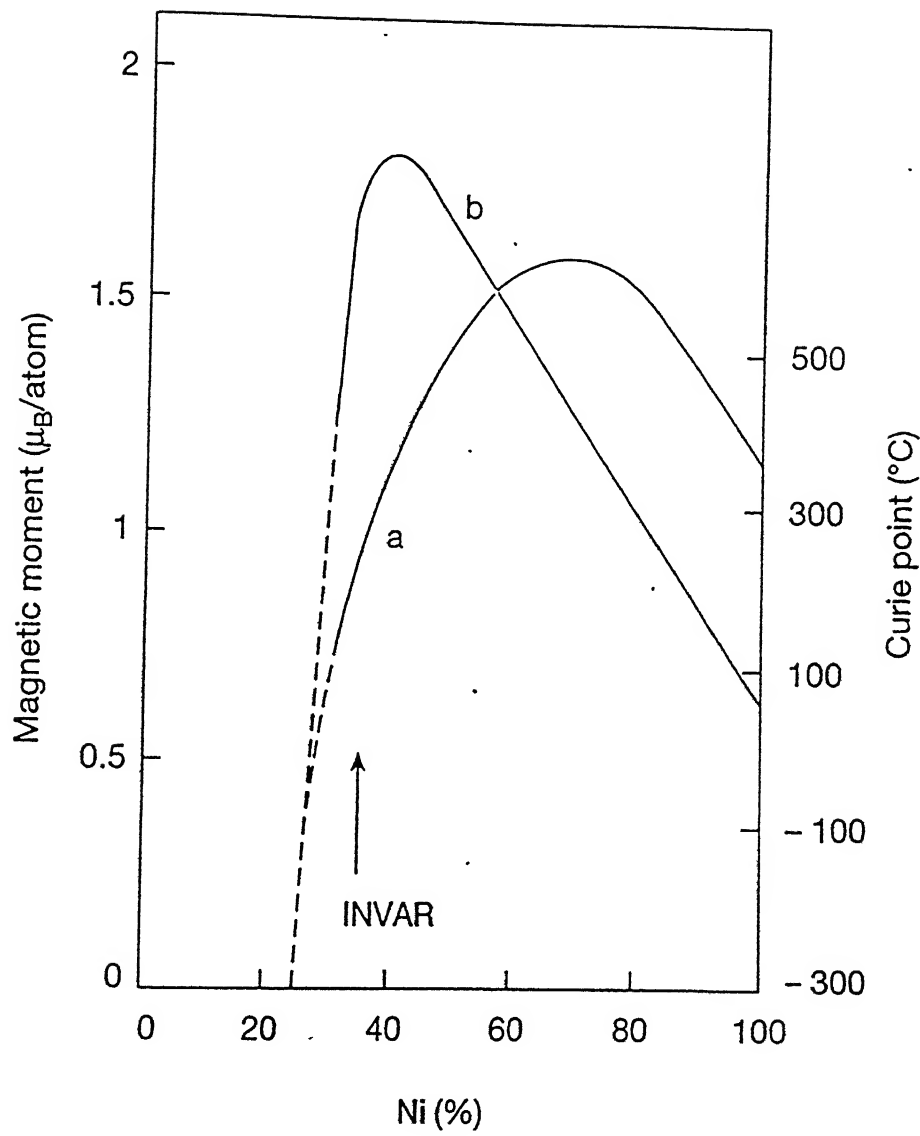
2.10 Ball-powder-ball collision of powder mixture during mechanical alloying (Gilman and Benjamin 1983).





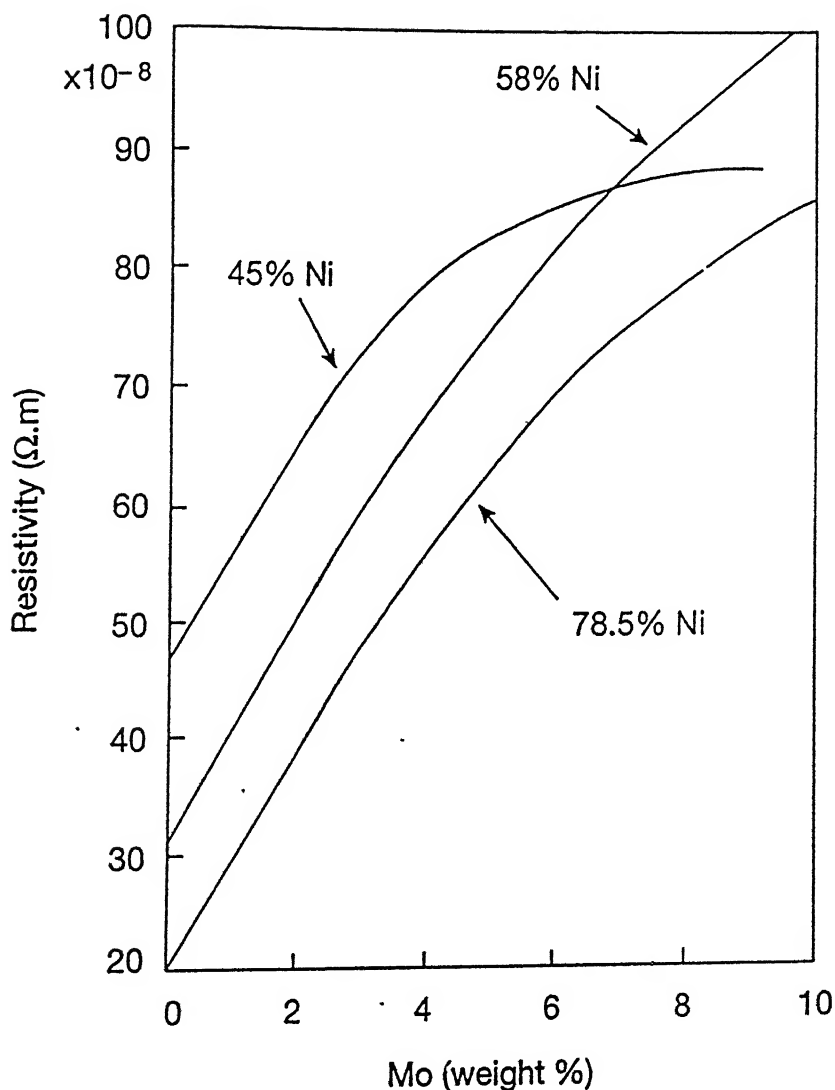
2.12

Effect of composition on lattice parameter (a) and density in Fe-Ni alloys at  $20^\circ\text{C}$ .



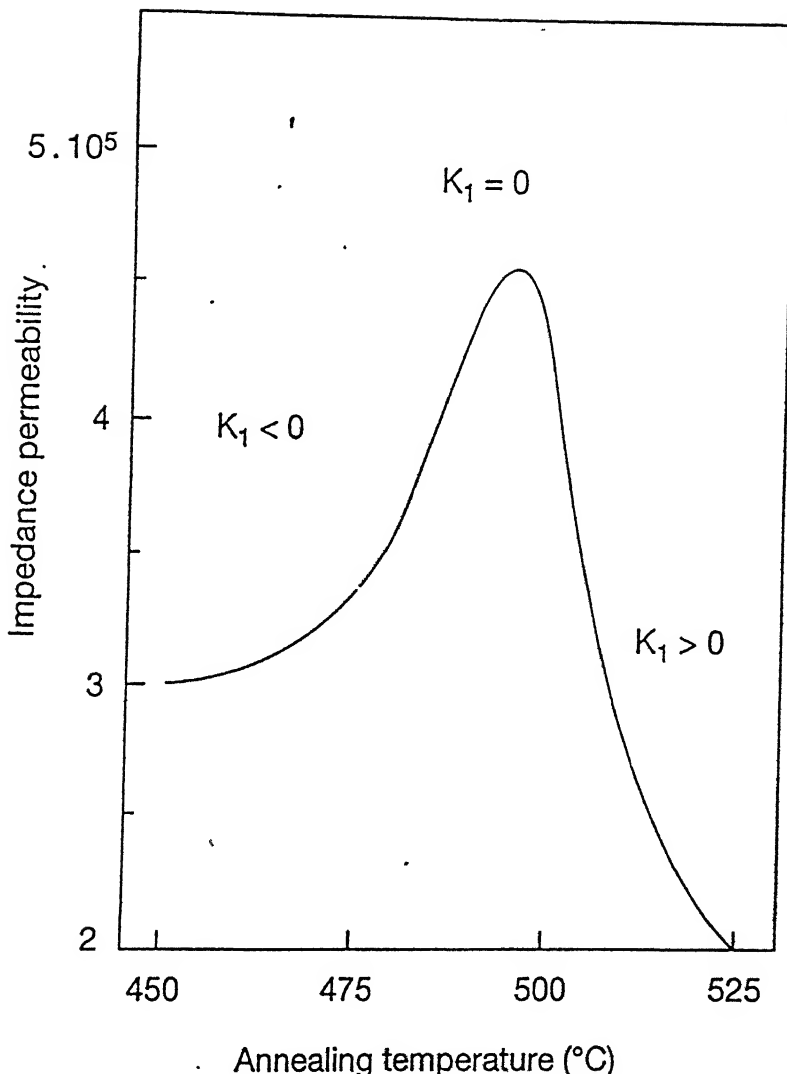
2.13

Variation of the Curie point and magnetic moment 770C is added to nickel, which has only  $0.6\mu_B$  in Fe-Ni alloys (Nakamura, 1976).



2.14

Effect of Mo on the resistivity of different Fe-Ni alloys.



2.15 Maximum impedance permeability for a 80Ni-15Fe-5Mo alloy as a function of annealing temperature.

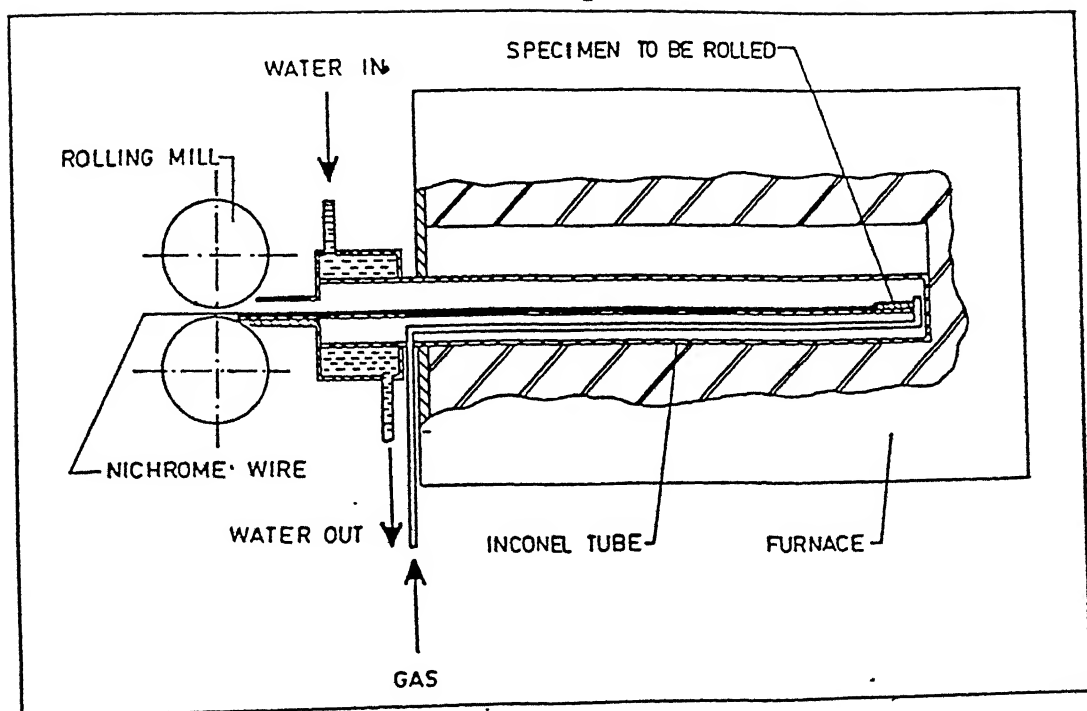


Fig 3.1

Hot rolling mill arrangement

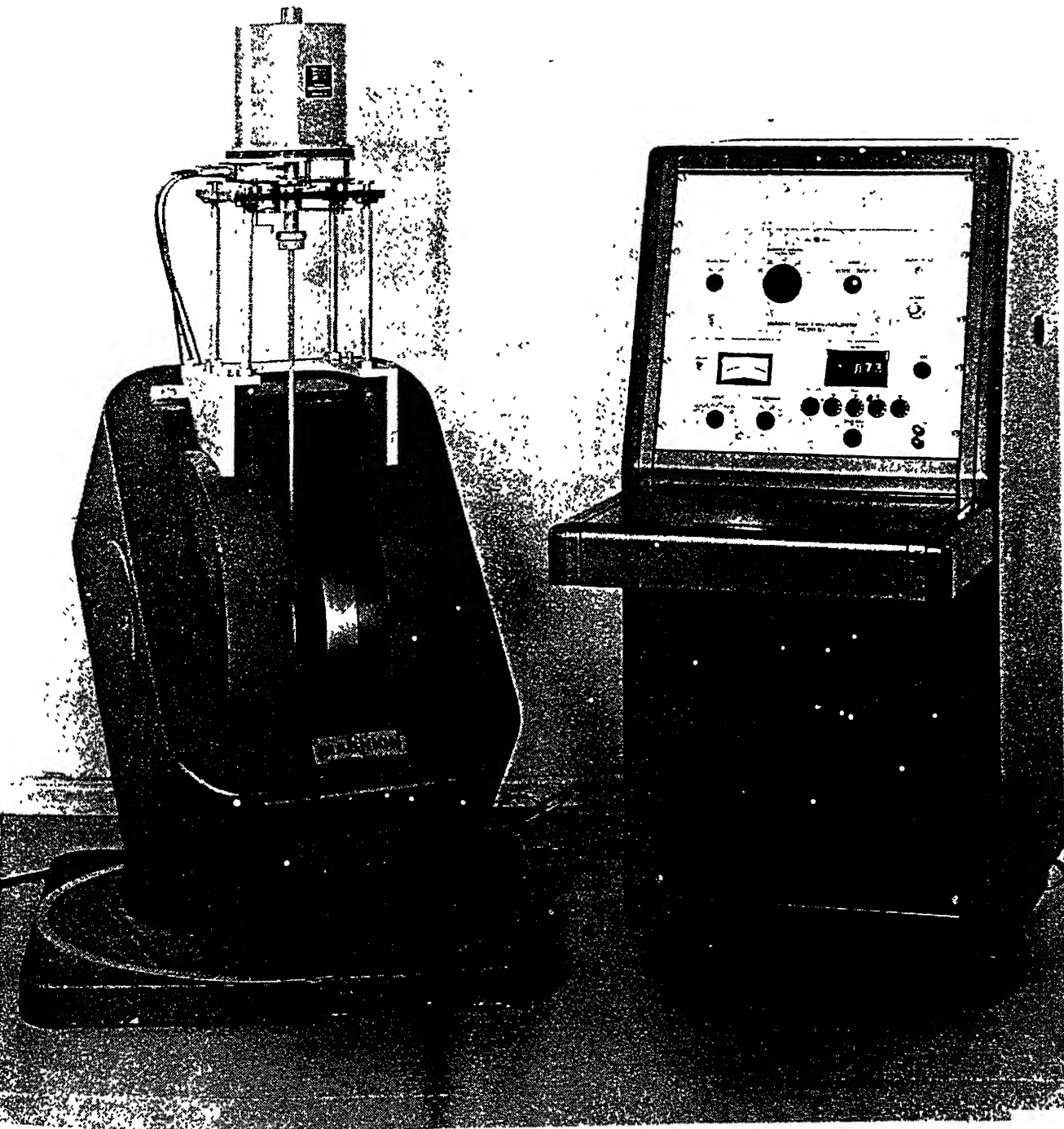


Fig 3.2

Model 155 Magnetometer system

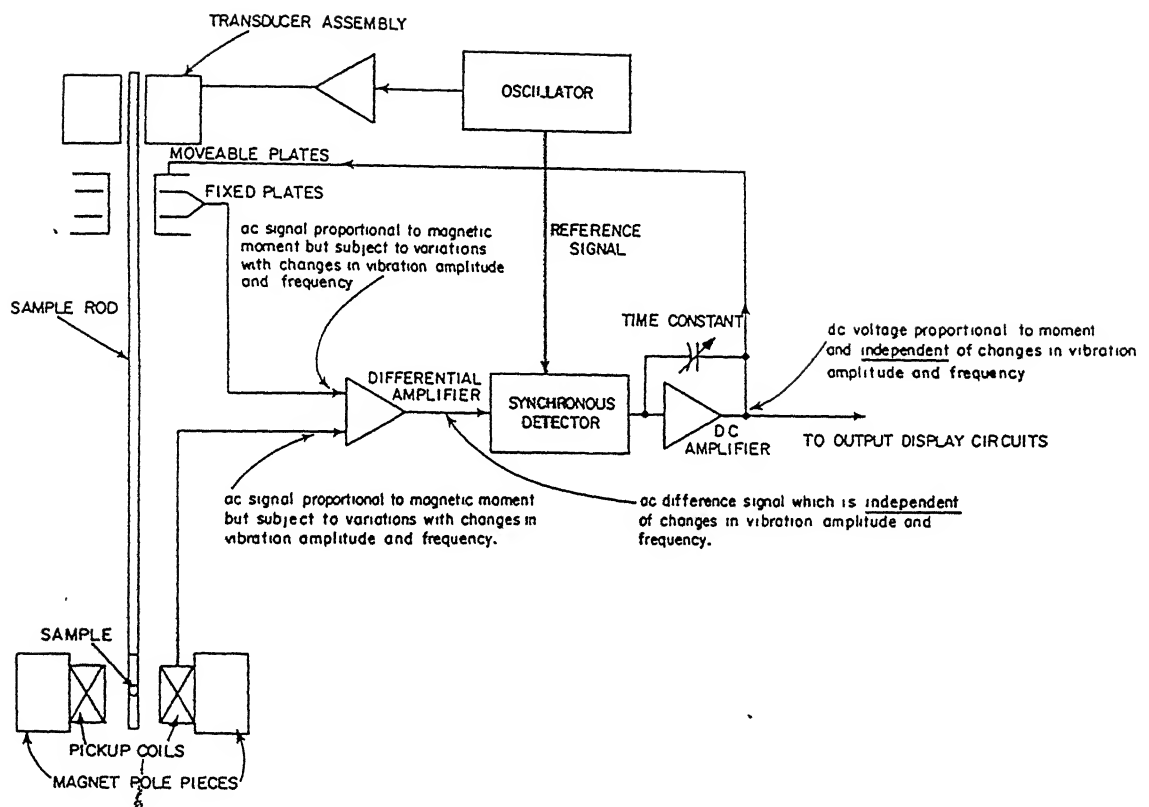


Fig 3.3

Simplified block diagram of the model 155 Magnetometer.

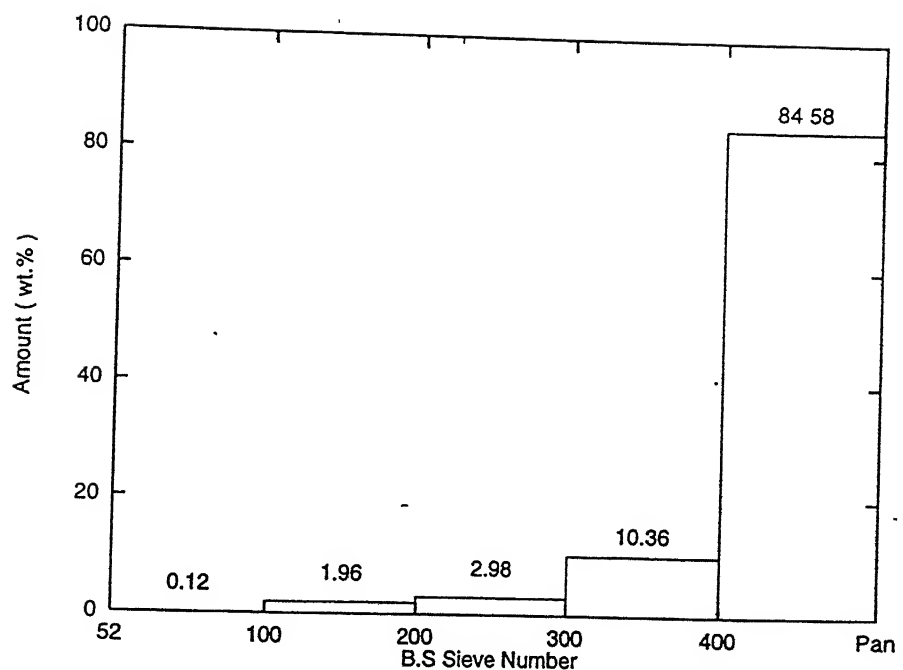


Fig 4.1a: Size distribution of carbonyl nickel powder.

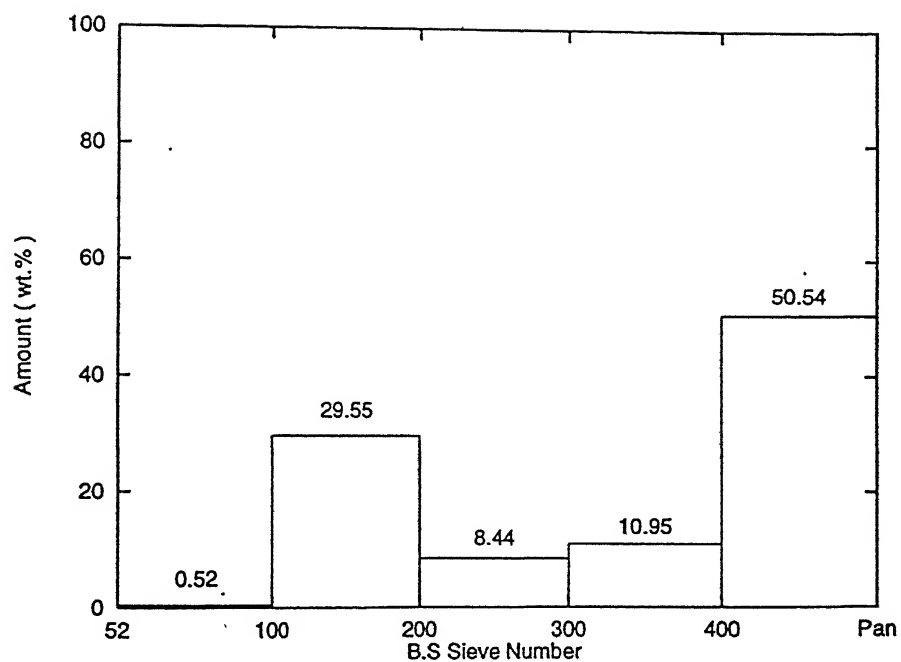


Fig 4.1b: Size distribution of electrolytic iron powder.

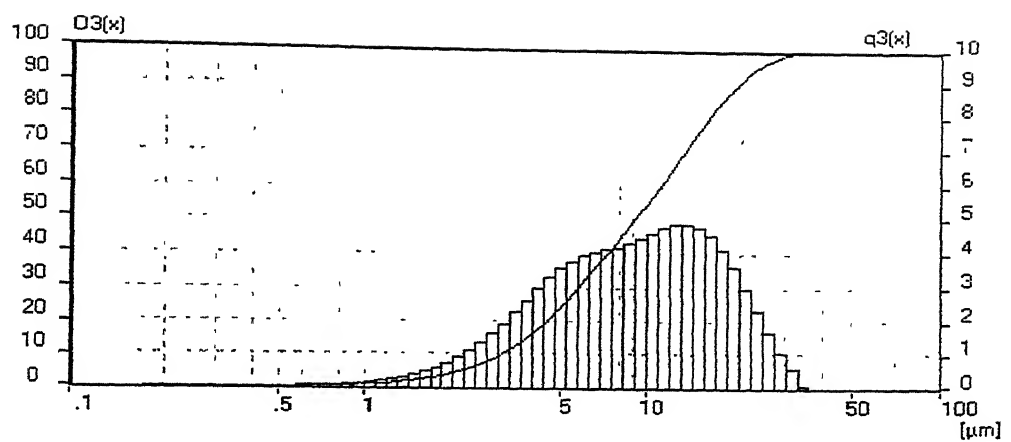


Fig 4.2a: Size distribution of carbonyl nickel powder determined by Laser Particle Size Analyzer.

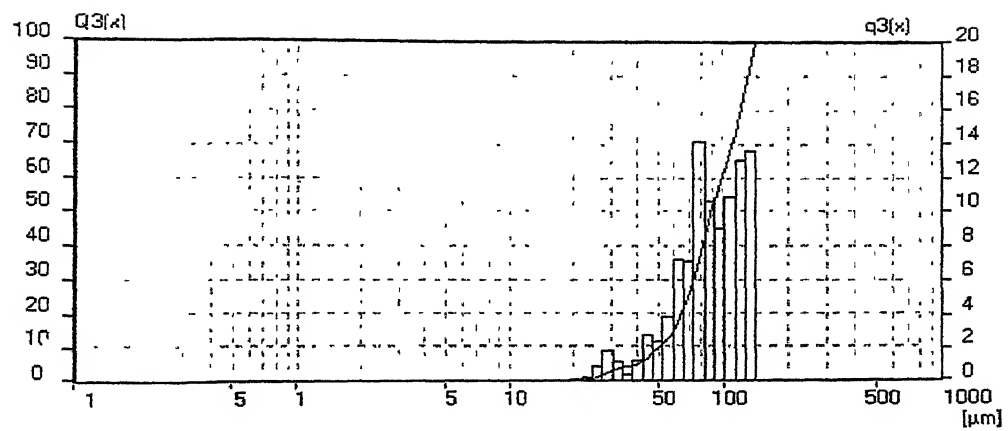


Fig 4.2b: Size distribution of electrolytic iron powder determined by Laser Particle Size Analyzer.

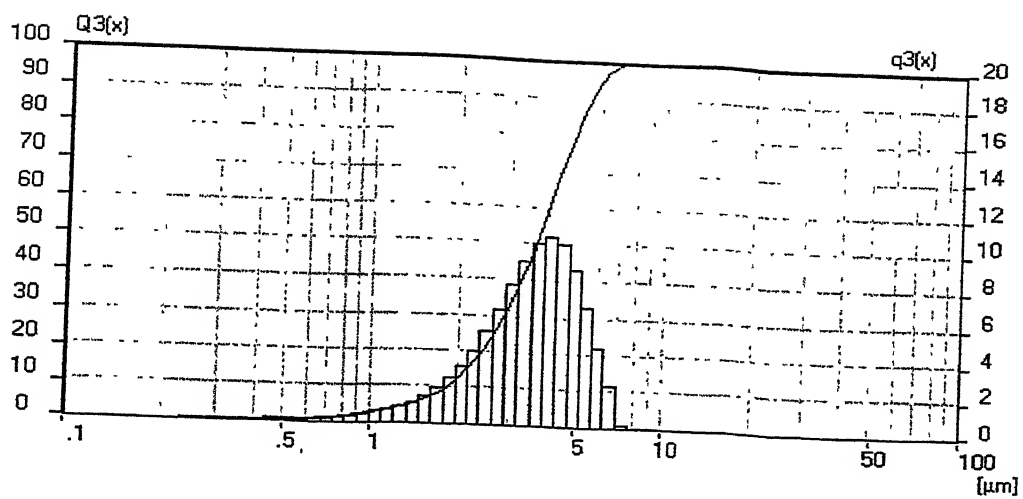
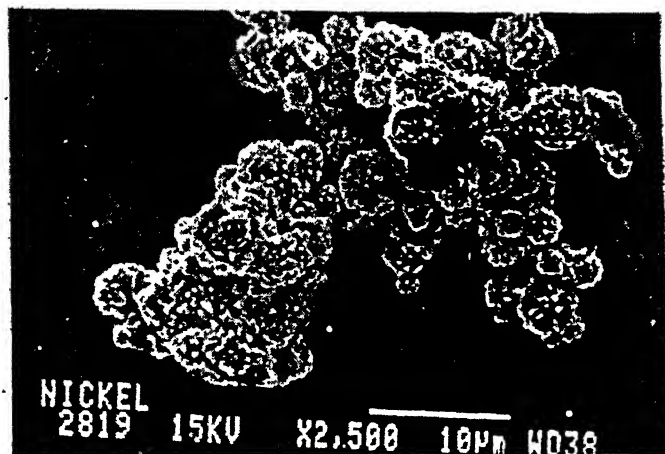
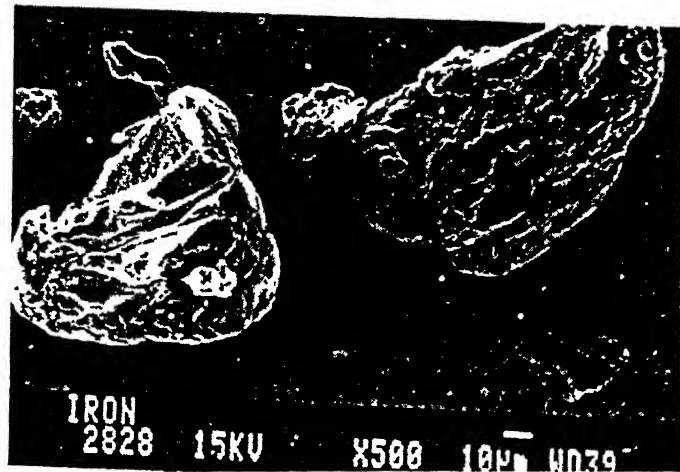


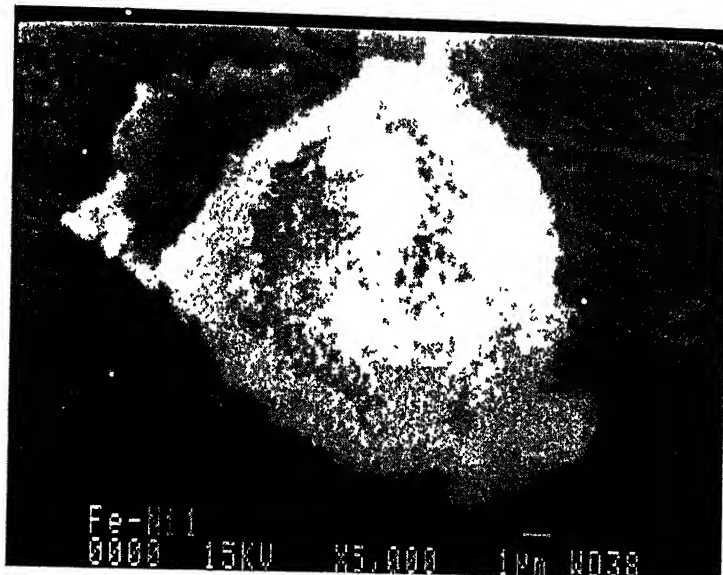
Fig 4.2c: Size distribution of mechanically alloyed 80wt%Ni-20wt%Fe powder (milling time =30hrs) determined by Laser Particle Size Analyzer.



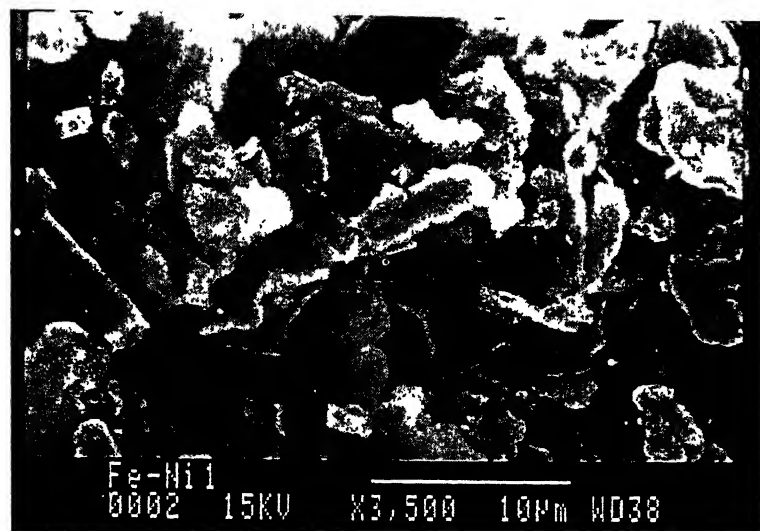
4.3a: SEM photograph of carbonyl nickel powder



4.3b: SEM photograph of electrolytic iron powder



4.3c: SEM photograph of mechanically alloyed 80Ni-20Fe powder (milling time=30hrs)



4.3d: SEM photograph of mechanically alloyed 80Ni-20Fe powder (milling time=30hrs)

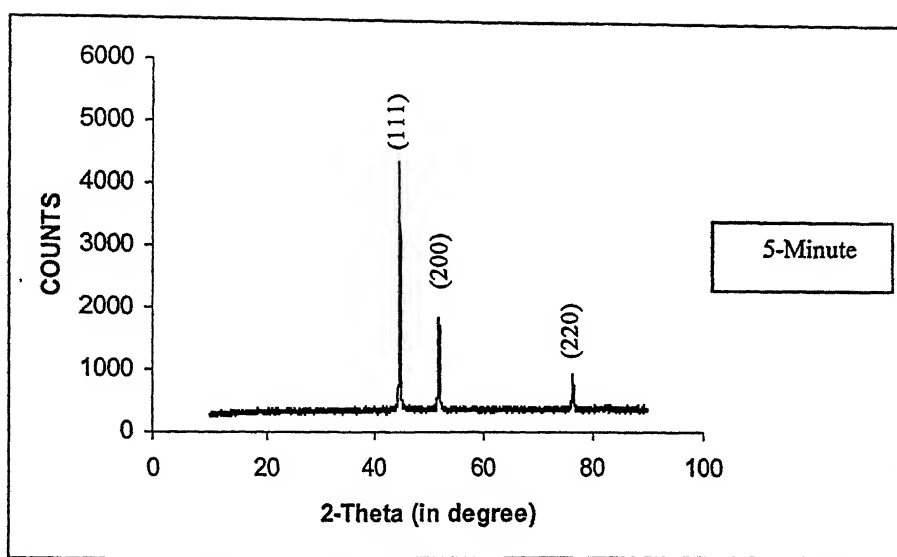


Fig 4.4: XRD pattern of mechanically alloyed 80Ni-20Fe powder (milling time=5min)

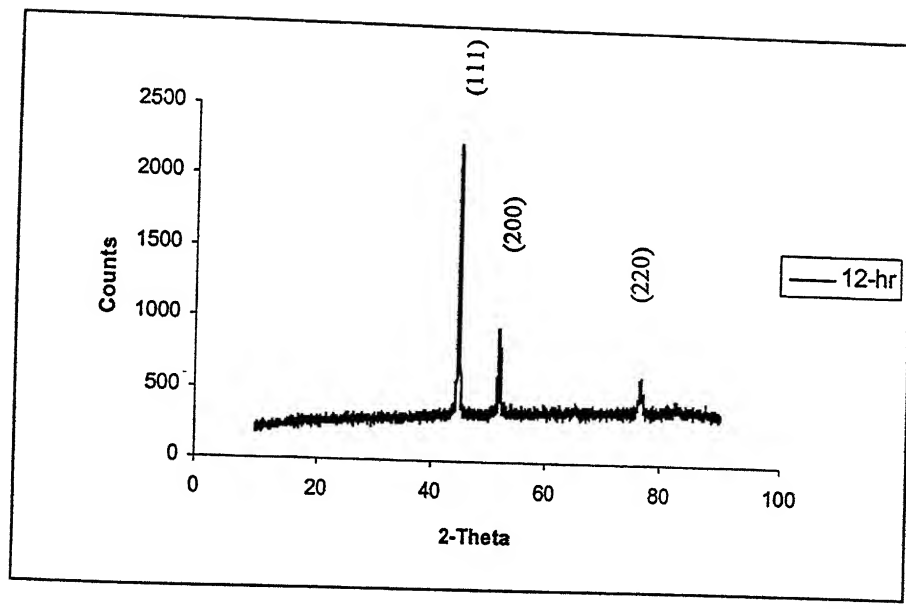


Fig 4.5: XRD pattern of mechanically alloyed 80Ni-20Fe powder (milling time=12 hr)

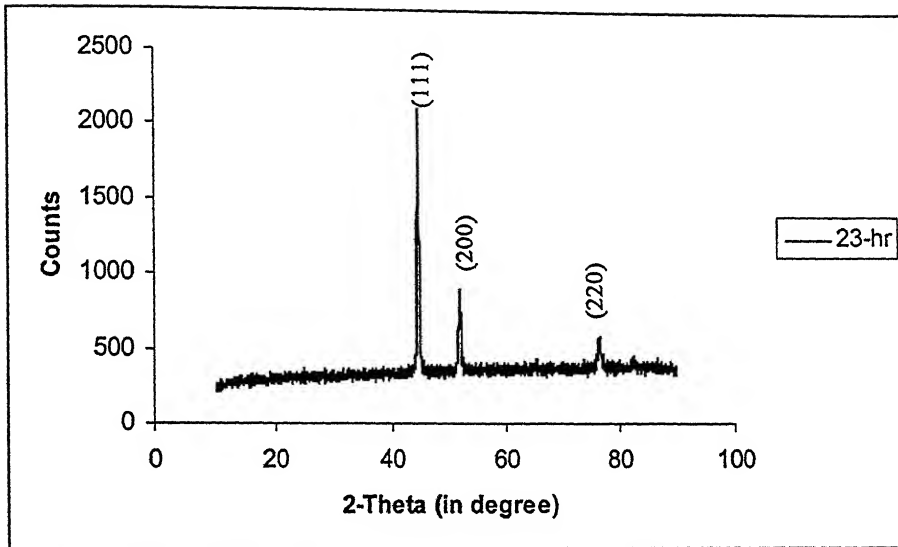


Fig 4.6: XRD pattern of mechanically alloyed 80Ni-20Fe powder (milling time=23hr)

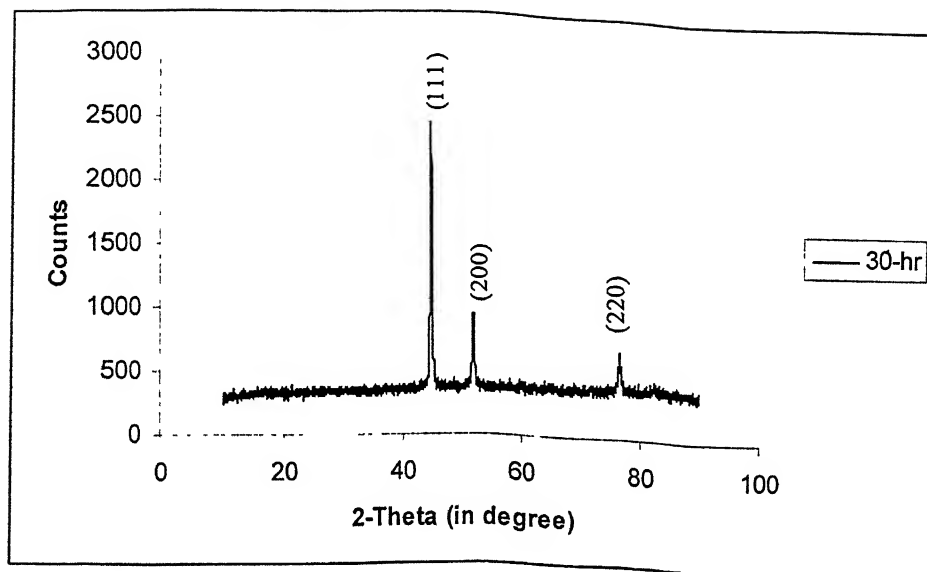


Fig 4.7: XRD pattern of mechanically alloyed 80Ni-20Fe powder (milling time=30hr)

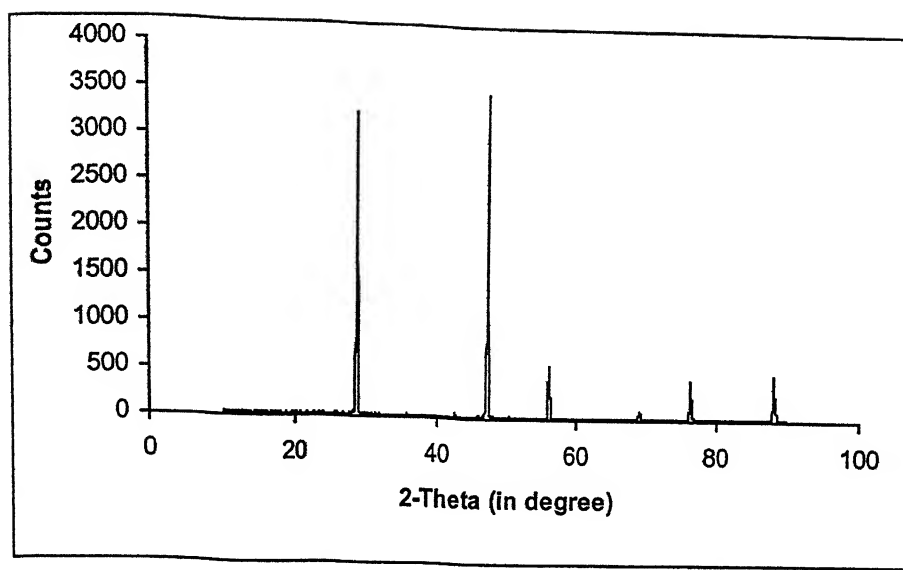


Fig 4.8: XRD pattern of pure standard Si powder

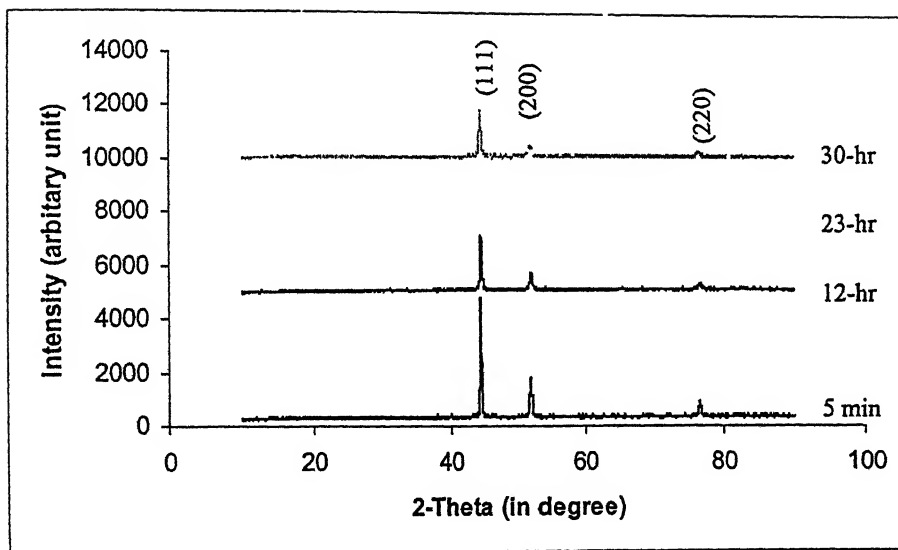


Fig 4.9: Comparison of XRD patterns of mechanically alloyed 80Ni-20Fe powders for 5min, 12hr, 23hr and 30hr.

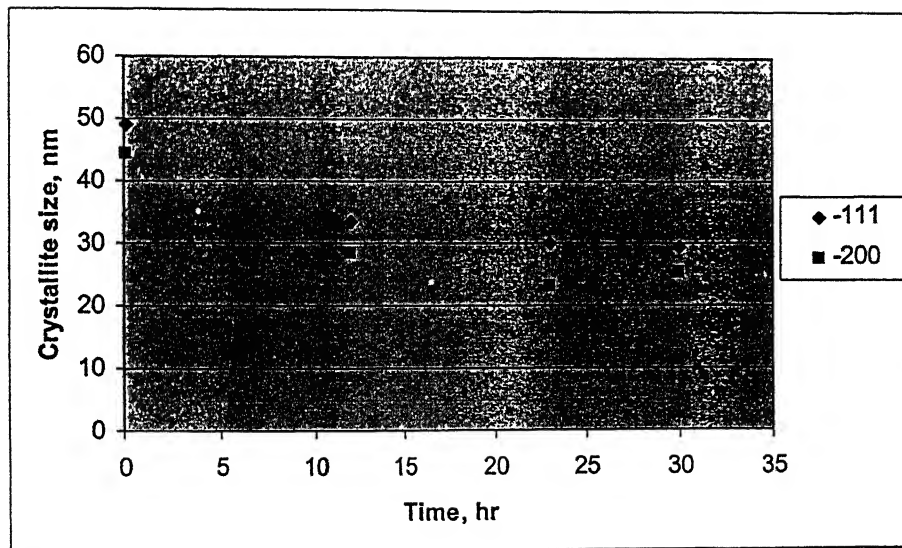


Fig 4.10: Effect of milling time on the crystallite size of mechanically alloyed 80Ni-20Fe.

**XRD-Ni PURE**

Sweep 0.3 °/min Range (CPM) 100K Time Constant (s) 30

Target Cu 20 mA 30 kV

Datafile C:\xray-data\Xx072203.txt Run on 22 Jul 2002 at 13:00

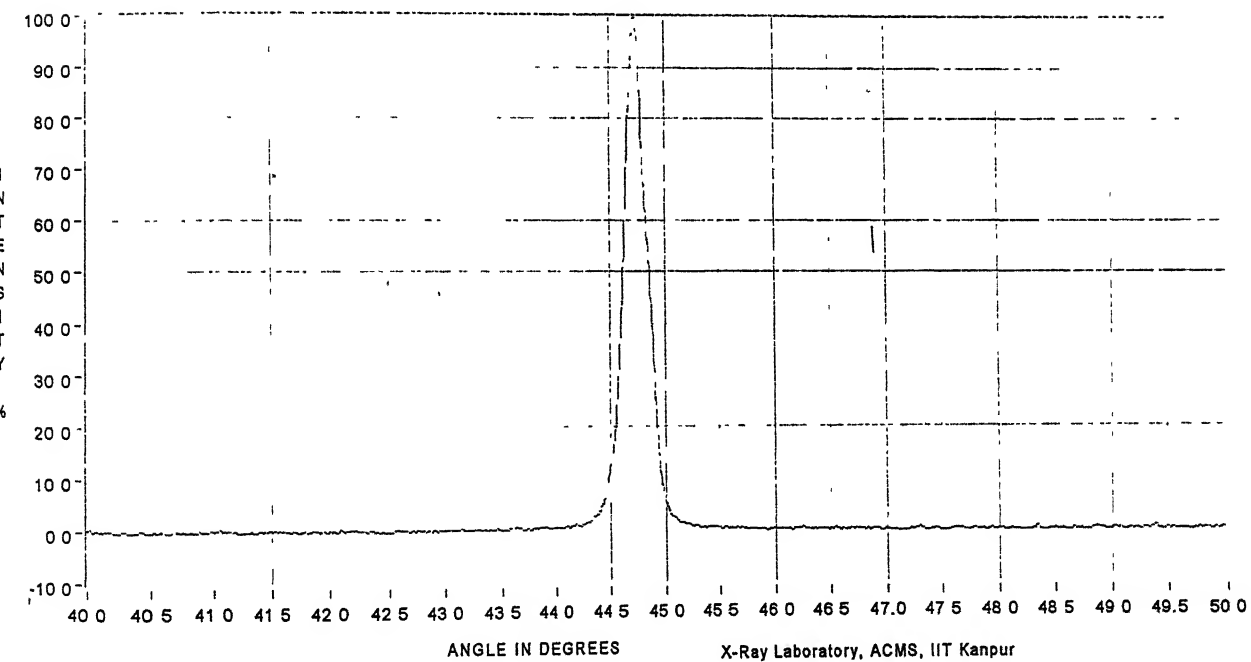


Fig 4.11: XRD pattern of as received carbonyl nickel powder.

**XRD Ni,1hr,1100C**

Intensity %	Angle <sup>o</sup>	d Å
99.08	44.58	2.032405
50.37	44.70	2.027399

Sweep 0.3 °/min Range (CPM) 100K Time Constant (s) 30

Target Cu 20 mA 30 kV

Datafile C:\xray-data\Xx072413.txt Run on 24 Jul 2002 at 17:29

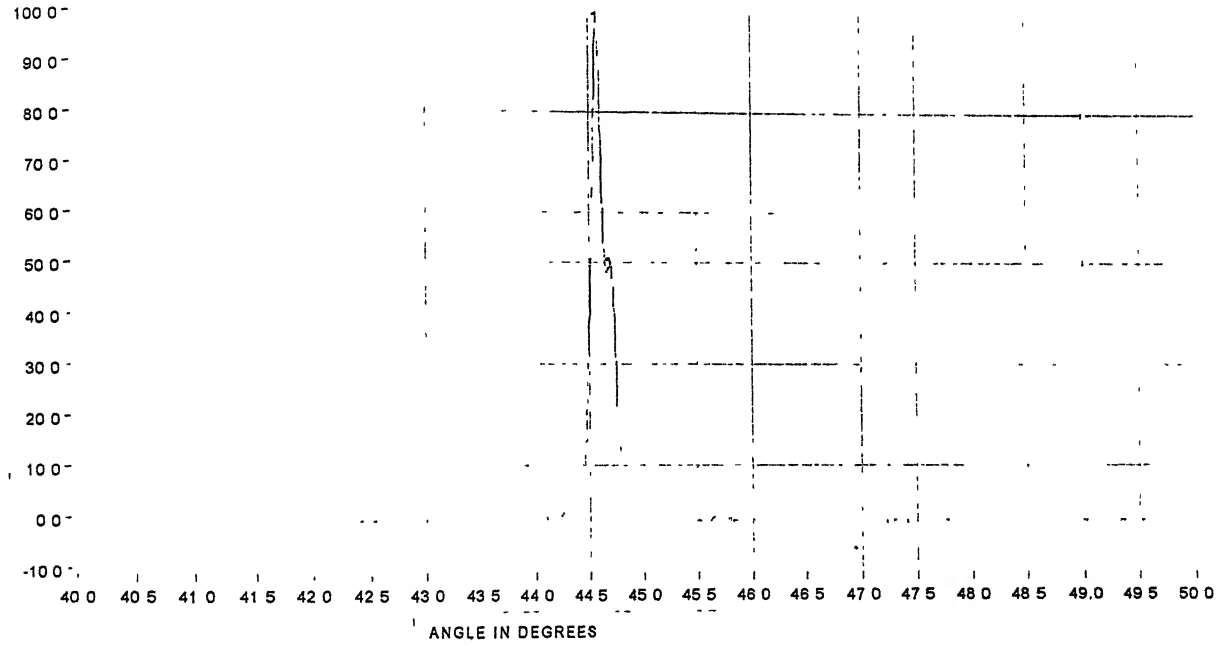


Fig 4.12: XRD pattern of carbonyl nickel powder after sintering for 1hr at 1100°C in a porcelain boat under hydrogen atmosphere.

**XRD -pure electrolytic iron**

Sweep 0.3 °/min Range (CPM) 20K Time Constant (s) 30  
Target Cu 20 mA 30 kV  
Datafile C:\xray-data\Xx072200.txt Run on 22 Jul 2002 at 10:22

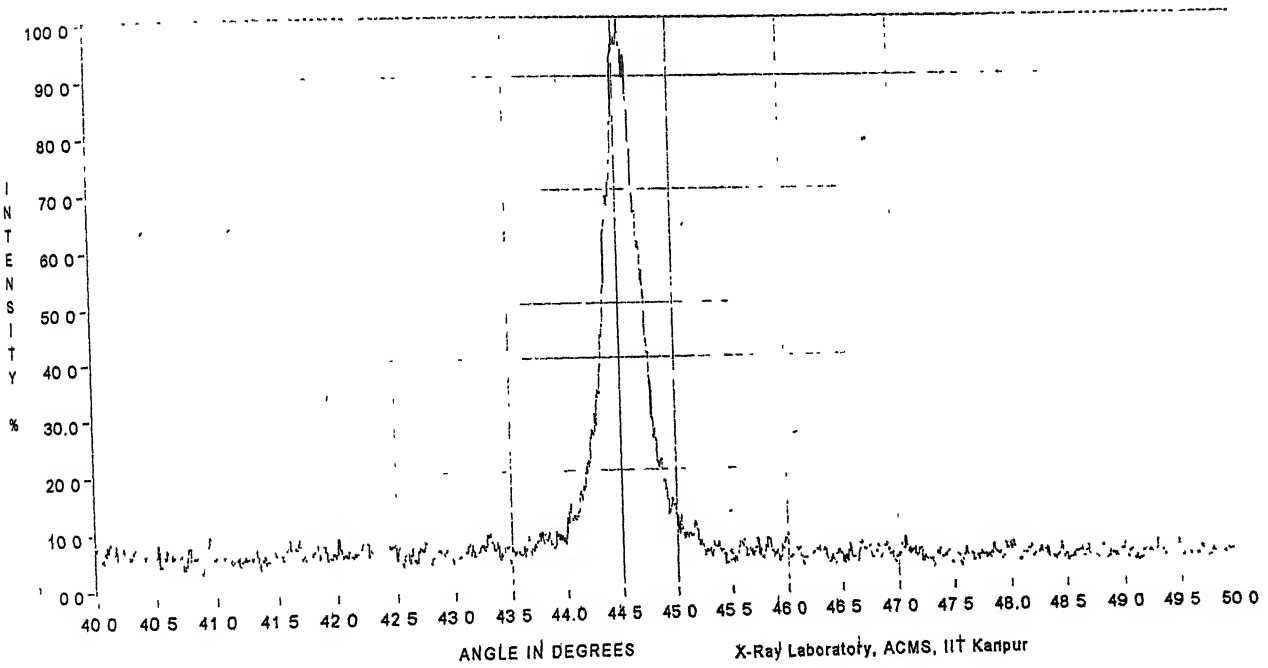


Fig 4.13: XRD pattern of as received carbonyl nickel powder.

### XRD Fe,1 hr,1100C

Sweep 0.3 °/min Range (CPM) 20K Time Constant (s) 3.0  
Target Cu 20 mA 30 kV  
Datafile C:\xray-data\Xx072414.txt Run on 24 Jul 2002 at 18:08

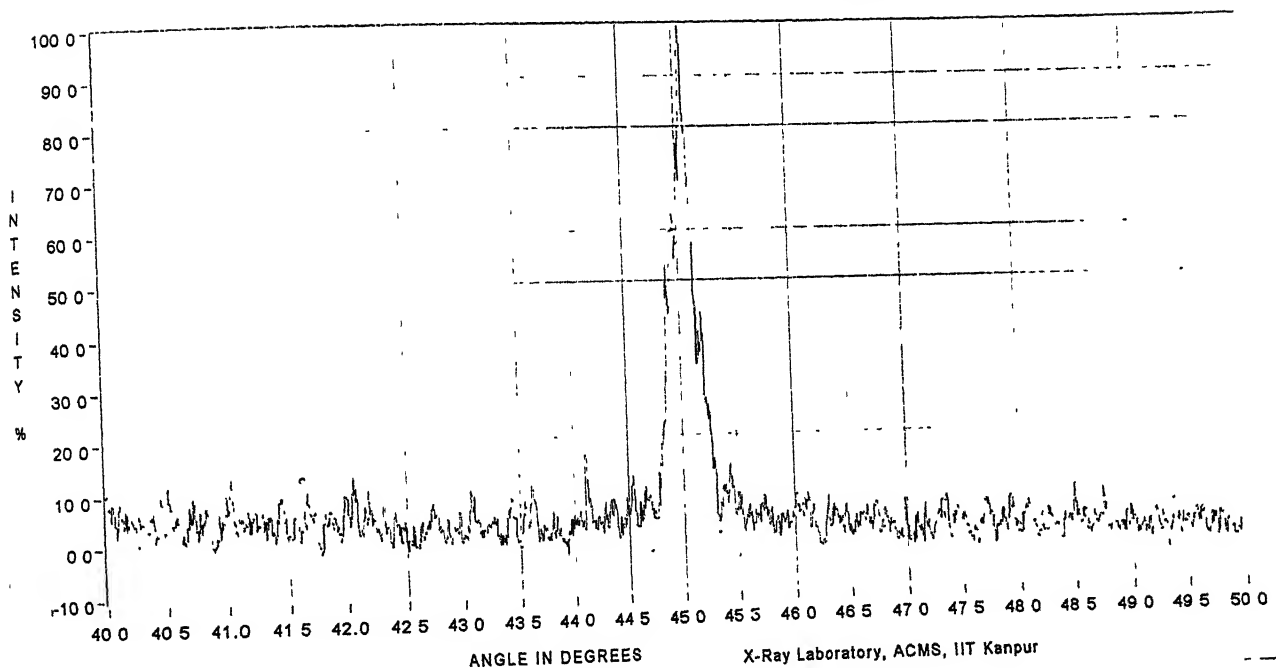


Fig 4.14: XRD pattern of electrolytic iron powder after sintering for 1hr at 1100°C in a porcelain boat under hydrogen atmosphere.

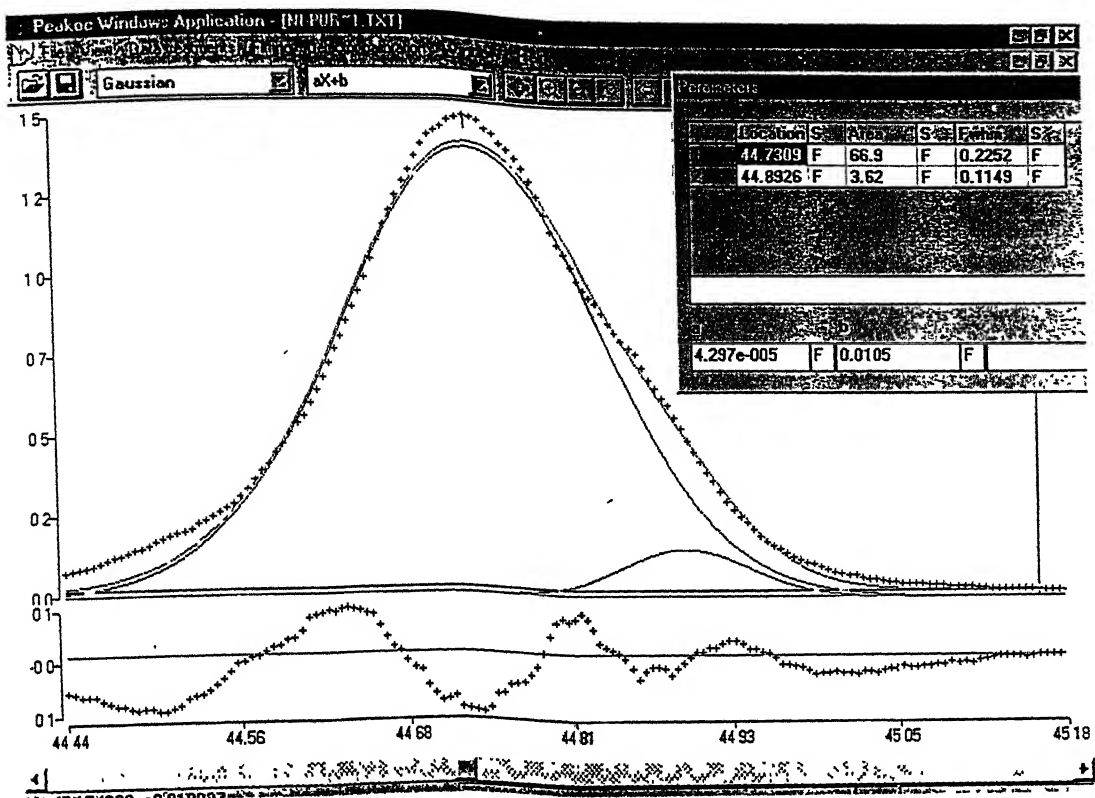


Fig 4.15: Profile shape function of Gaussian type for carbonyl nickel. This shows the value of respective  $2\theta$  and FWHM.

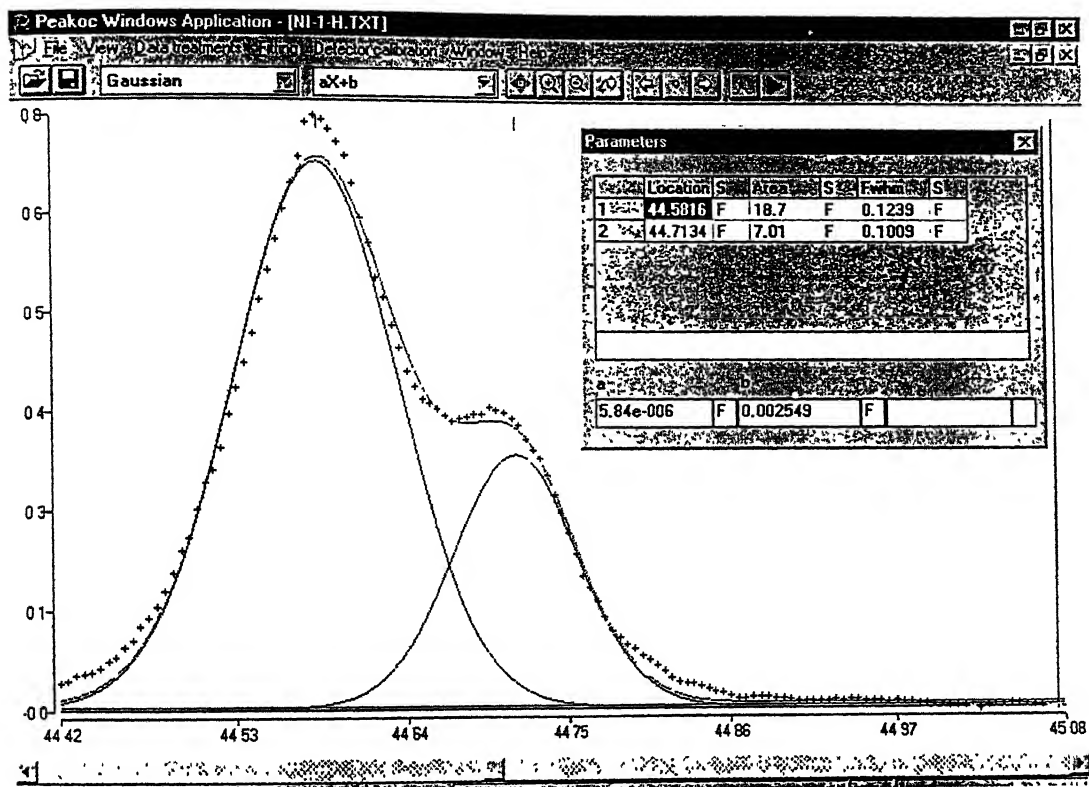


Fig 4.16: Profile shape function of Gaussian type for carbonyl nickel sintered at  $1100^{\circ}\text{C}$  under  $\text{H}_2$  atmosphere. This shows the value of respective  $2\theta$  and FWHM.



a)



b)

Fig 4.17. Bright field images of hot rolled mechanically alloyed 80Ni-20Fe seen under Transmission Electron Microscope (a, and b)



c)



d)

Fig 4.17 Bright field images of hot rolled mechanically alloyed 80Ni-20Fe  
seen under Transmission Electron Microscope (c and d)

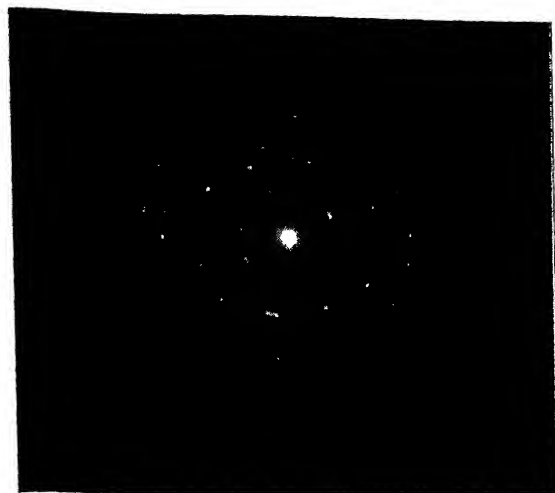


e)

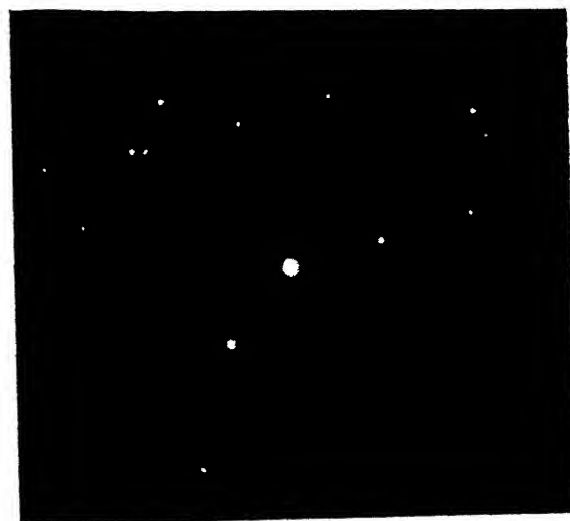


f)

Fig 4.17 Bright filed images of hot rolled mechanically alloyed 80Ni-20Fe seen under Transmission Electron Microscope (e and f)

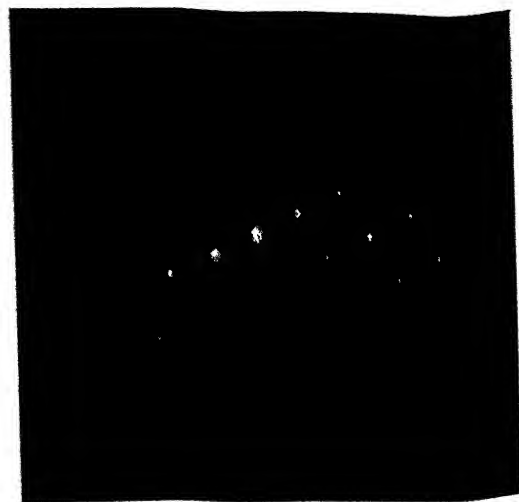


a)

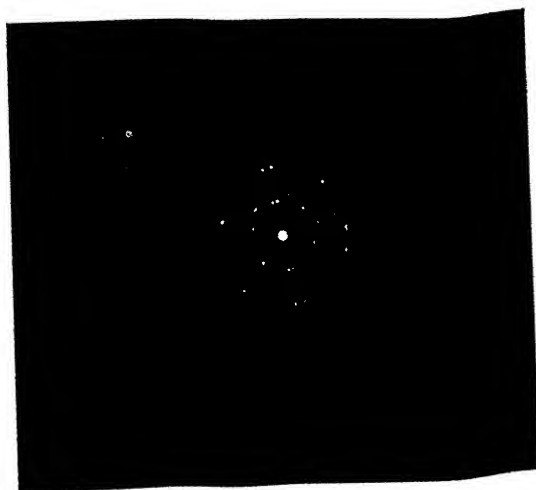


b)

Fig 4 18: Selected area diffraction patterns of hot rolled mechanically alloyed 80Ni-20Fe seen under Transmission Electron Microscope (a and b)

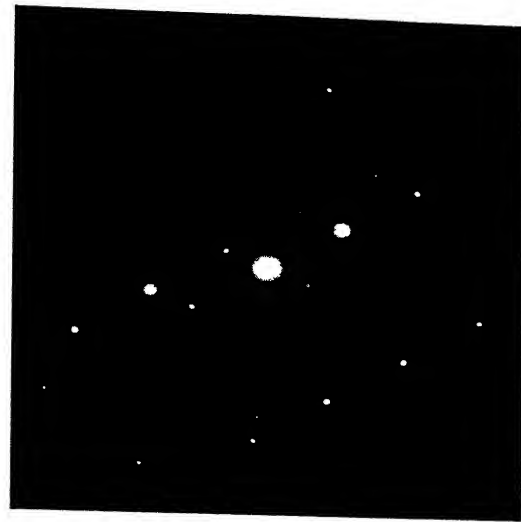


c)

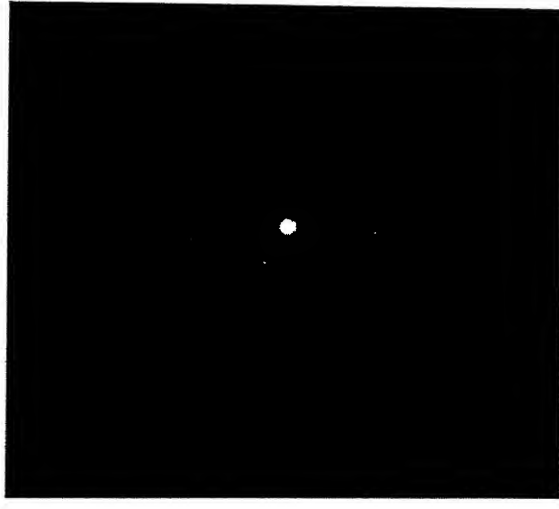


d)

Fig 4.18: Selected area diffraction patterns of hot rolled mechanically alloyed 80Ni-20Fe seen under Transmission Electron Microscope (c and d)



e)



f)

Fig 4 18: Selected area diffraction patterns of hot rolled mechanically alloyed 80Ni-20Fe seen under Transmission Electron Microscope (e and f)

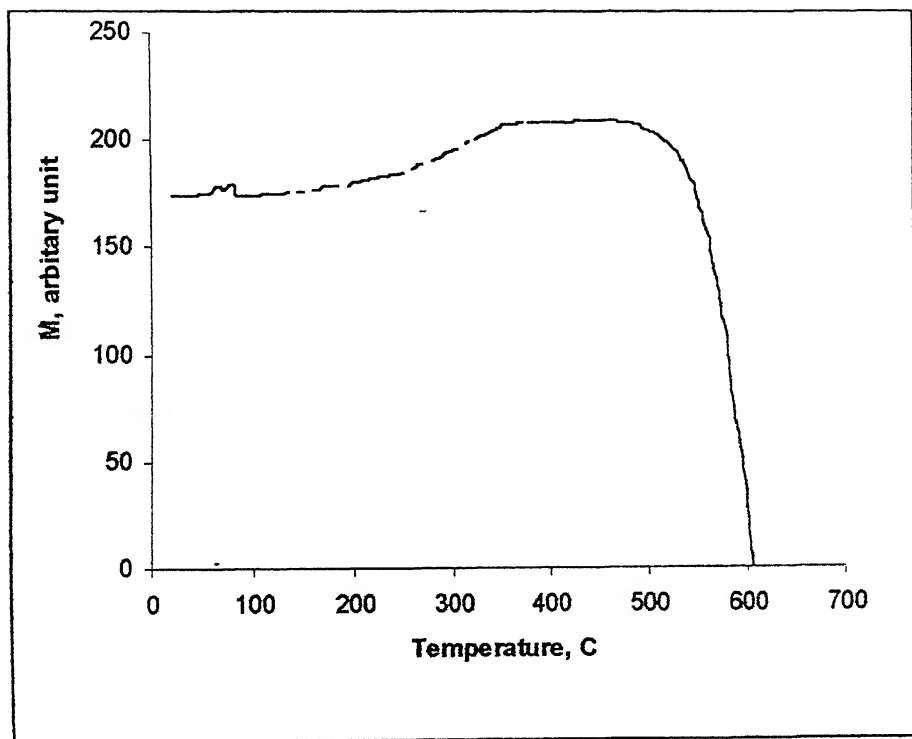


Fig 4 19 Temperature dependence of magnetizations for hot rolled mechanically alloyed 80Ni-20Fe at a rate of 3K/min the Curie temperature was found to be  $525^{\circ}\text{C}$

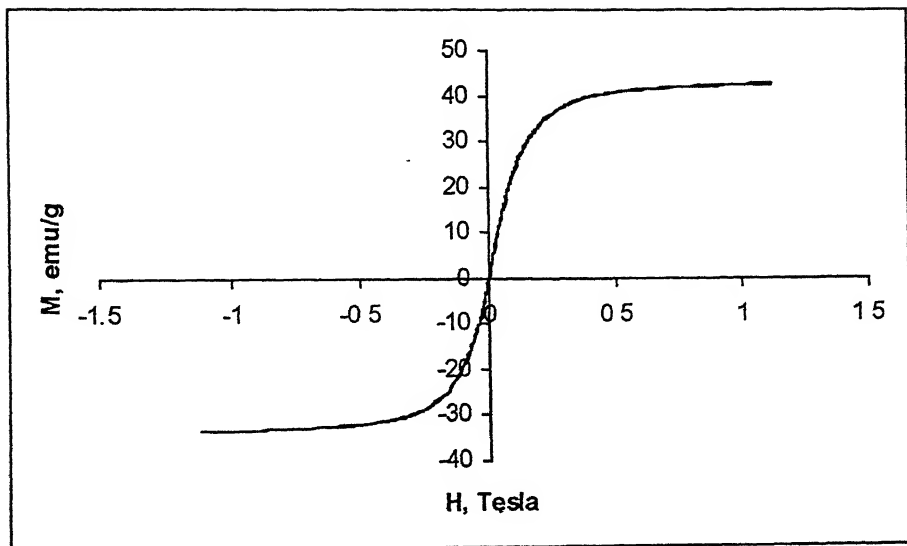


Fig 4.20 Magnetic field dependence of saturation magnetization for mechanically alloyed 80Ni-20Fe at room temperature.

# TABLES

## LIST OF TABLES

---

**TABLE 1.1 CHANGES IN PROPERTIES AT THE NANOCRYSTALLINE-SIZE SCALE [2]**

**Electrical**

Higher electrical conductivity in ceramics and magnetic nanocomposites  
Higher electrical resistivity in metals

**Magnetic**

Increase in magnetic coercivity down to a critical grain size  
Below critical grain size, decrease in grain size leading to super paramagnetic behavior

**Mechanical**

Increase in hardness and strength of metals and alloys  
Enhanced ductility, toughness and formability of ceramics

**Optical**

Blue-shift of optical spectra of quantum confined crystallites  
Increase in luminescent efficiency of semiconductors

*Source: Business Communications Company*

---

**TABLE 1. 2 CURRENT AND PROJECTED U.S. MARKET FOR NANOSTRUCTURED MATERIALS [2]**

	1996		2001		Avg. Annual
	Dollar Value	Market Percent	Dollar Value	Market Percent	
Growth rate					
Particles*	\$41,300,000	97.6%	\$ 148,600,00	96.1%	24.2%
Coatings	\$1,000,000	2.4%	\$ 6,000,000	100%	3.29.6%
Total	\$42,300,000	100%	\$ 154,600,000	100%	29.6%

\*Dry powders and liquid dispersions

*Source: Business Communications Company*

TABLE 2.1 CLASSIFICATION OF NANOCRYSTALLINE MATERIALS [12]

Dimensionality	Designation	Typical methods of synthesis
Zero-dimensional (0-D)	Clusters	Sol-gel methods
One-dimensional (1-D)	Layered (lamellar)	Vapor deposition Electro deposition
Two-dimensional (2-D)	Filamentary	Chemical vapor deposition
Three-dimensional (3-D)	Crystallites (equiaxed)	Gas condensation Mechanical alloying

TABLE 2.2 METHODS TO SYNTHESIZE NANOCRYSTALLINE MATERIALS [12]

Starting phase	Technique	Nature of product
Vapor	Inert gas condensation	3-D
	Physical vapor deposition-	1-D
	Plasma processing	3-D
	Chemical vapor deposition	3-D, 2-D
Liquid	Rapid solidification	3-D
	Electro deposition	1-D, 3-D
	Chemical reactions	3-D
Solid	Mechanical alloying	3-D
	Devitrification	3-D
	Spark erosion	3-D
	Sliding wear	3-D

---

**TABLE 2.3 ATTRIBUTES OF MECHANICAL ALLOYING [12]**

1.	Production of a fine dispersion of second phase particles
2.	Extension of solid solubility limits
3	Refinement of grain sizes down to the nanometer range
4.	Synthesis of novel crystalline and quasi crystalline phases
5.	Development of amorphous (glassy) phases
6.	Disordering of ordered intermetallics
7.	Possibility of alloying of difficult to alloy elements
8.	Induction of chemical (displacement) reactions at low temperatures
9.	Scalable process

---

**TABLE 2.4 TYPES OF MILL AND TYPICAL SAMPLE WEIGHT GENERALLY USED [12]**

Mill Type	Sample Weight
Mixer mills	up to 2*20g
Planetary mills	up to 4*250g
Attritors	0.5 to 100kg
Uni-ball mills	4*2000g

---

TABLE 2.5 COMMONLY USED PROCESS CONTROL REAGENTS (PCR) [34]

PCA	Chemical formula	Quantity
Benzene	C <sub>6</sub> H <sub>6</sub>	---
DDAA	C <sub>28</sub> H <sub>59</sub> NO <sub>2</sub>	---
DHDAA	C <sub>36</sub> H <sub>75</sub> NO <sub>2</sub>	---
Dodecane	CH <sub>3</sub> (CH <sub>2</sub> ) <sub>10</sub> CH <sub>3</sub>	---
Ethanol	C <sub>2</sub> H <sub>5</sub> OH	4 wt%
Ethyl Acetate	CH <sub>3</sub> CO <sub>2</sub> C <sub>2</sub> H <sub>5</sub>	---
Graphite	C	0.5 wt%
Methanol	CH <sub>3</sub> OH	---
Octane	CH <sub>3</sub> (CH <sub>2</sub> ) <sub>6</sub> CH <sub>3</sub>	1 wt%
Paraffin	-----	---
Sodium Chloride	NaCl	2 wt%
Toluene	C <sub>6</sub> H <sub>5</sub> CH <sub>3</sub>	5 ml
Tetrahydrofuran	-----	---
Stearic Acid	CH <sub>3</sub> (CH <sub>2</sub> ) <sub>16</sub> COOH	1 wt%
Silicon grease	-----	---
Hexane	CH <sub>3</sub> (CH <sub>2</sub> ) <sub>4</sub> CH <sub>3</sub>	---
Heptane	CH <sub>3</sub> (CH <sub>2</sub> ) <sub>4</sub> CH <sub>3</sub>	0.5 wt%

TABLE 2.6 PROPERTIES OF THE FERROMAGNETIC AND NEIGHBOURING TRANSITION ELEMENTS [26]

	Ti	V	Cr	Mn	Fe	Co	Ni	Cu
Electronic structure	[Ar]3d <sup>2</sup> 4s <sup>2</sup>	[Ar]3d <sup>3</sup> 4s <sup>2</sup>	[Ar]3d <sup>3</sup> 4s	[Ar]3d <sup>5</sup> 4s <sup>2</sup>	[Ar]3d <sup>6</sup> 4s <sup>2</sup>	[Ar]3d <sup>7</sup> 4s <sup>2</sup>	[Ar]3d <sup>8</sup> 4s <sup>2</sup>	[Ar]3d <sup>10</sup> 4s
Metallic radius <sup>(a)</sup>	1.45	1.31	1.28	1.17	1.27	1.26	1.24	1.28
Melting point <sup>(b)</sup>	1,670	1,890	1,860	1,244	1,535	1,495	1,453	1,083
Thermal expansion at 20°C <sup>(c)</sup>	8.5	8	6	22	12	12	13	16.6
Resistivity at 20°C <sup>(d)</sup>	42	25	13.5	~200	10	9.8	7.8	1.7
Magnetic state	Para.	Para.	Anti ferro.	Anti ferro.	Ferro	Ferro	Ferro.	Dia.

(a). A

(b). °C

(c) · 10<sup>-6</sup>/ °C

(d) · 10<sup>-8</sup>Ωm

TABLE 3.1 Slurry composition used for casting green strip of M.A. 80Ni-20Fe

Constituents	Amount
Nickel-iron	70 wt%
Glycerol	4 wt%
Methyl Cellulose	1 wt%
Water	25 wt%

Table 4.1 Interpolated values of the particle size of Ni, Fe, and M.A. 80Ni-20Fe (milling time = 30 hr) powders

Cumulative	Ni	Fe	Ni-Fe
95%>	2.19 $\mu\text{m}$	40.37 $\mu\text{m}$	1.34 $\mu\text{m}$
90%>	3.09 $\mu\text{m}$	51.44 $\mu\text{m}$	1.83 $\mu\text{m}$
85%>	3.80 $\mu\text{m}$	59.65 $\mu\text{m}$	2.16 $\mu\text{m}$
80%>	4.45 $\mu\text{m}$	64.43 $\mu\text{m}$	2.43 $\mu\text{m}$
75%>	5.09 $\mu\text{m}$	69.65 $\mu\text{m}$	2.67 $\mu\text{m}$
70%>	5.75 $\mu\text{m}$	74.47 $\mu\text{m}$	2.88 $\mu\text{m}$
65%>	6.47 $\mu\text{m}$	77.52 $\mu\text{m}$	3.08 $\mu\text{m}$
60%>	7.24 $\mu\text{m}$	80.55 $\mu\text{m}$	3.26 $\mu\text{m}$
55%>	8.09 $\mu\text{m}$	84.23 $\mu\text{m}$	3.45 $\mu\text{m}$
50%>	9.00 $\mu\text{m}$	88.74 $\mu\text{m}$	3.63 $\mu\text{m}$
45%>	9.99 $\mu\text{m}$	93.69 $\mu\text{m}$	3.81 $\mu\text{m}$
40%>	11.04 $\mu\text{m}$	99.61 $\mu\text{m}$	3.99 $\mu\text{m}$
35%>	12.15 $\mu\text{m}$	105.29 $\mu\text{m}$	4.18 $\mu\text{m}$
30%>	13.36 $\mu\text{m}$	110.76 $\mu\text{m}$	4.38 $\mu\text{m}$
25%>	14.68 $\mu\text{m}$	116.10 $\mu\text{m}$	4.60 $\mu\text{m}$
20%>	16.18 $\mu\text{m}$	121.20 $\mu\text{m}$	4.85 $\mu\text{m}$
15%>	17.97 $\mu\text{m}$	126.29 $\mu\text{m}$	5.13 $\mu\text{m}$
10%>	20.24 $\mu\text{m}$	131.64 $\mu\text{m}$	5.49 $\mu\text{m}$
5%>	23.63 $\mu\text{m}$	137.09 $\mu\text{m}$	6.00 $\mu\text{m}$
1%>	29.46 $\mu\text{m}$	141.45 $\mu\text{m}$	6.75 $\mu\text{m}$

Table 4.2: Particle size of Ni, Fe and 80Ni-20Fe (milling time=30hr) powders corresponding to various d values

d values , $\mu\text{m}$	Particles size corresponding to respective d values, $\mu\text{m}$		
	Ni	Fe	80Ni-20Fe
$d_{95}$	2.2	40.4	1.3
$d_{50}$	9	89	4
$d_5$	24	137	6

Table 4.3: Profile shape function fitting parameter for MA 80Ni-20Fe a) Gaussian fit

Time	2θ	FWHM
5-min	(45.7867, 53.3943, 78.7790)	(0.223, 0.298, 0.327)
12 hr	(44.6933, 52.0192, 76.5767)	(0.306, 0.399, 0.638)
23 hr	(44.6641, 51.9972, 76.5206)	(0.337, 0.468, 0.494)
30 hr	(44.5707, 51.8921, 76.4264)	(0.343, 0.436, 0.519)

b) Pseudo-Voigt fit

Time	2θ	FWHM
5-min	(44.5784, 51.9289, 76.4557)	(0.160, 0.231, 0.272)
12 hr	(44.6554, 51.9745, 76.4896)	(0.229, 0.377, 0.391)
23 hr	(44.6626, 51.998, 76.528)	(0.273, 0.433, 0.426)
30 hr	(44.5707, 51.8921, 76.4264)	(0.319, 0.467, 0.519)

Table 4.4 Variation of grain size with milling time

Time	Plane (111)	Plane (200)
5 min	49	44
12 hr	33	29
23 hr	30	23
30 hr	29	25

Table 4.5 Ratio of d spacing vs. crystallite size

Time	Plane (111) / Plane (200)	$d_{(111)} / d_{(200)}$
5 min	1.107	1 1534
12 hr	1.175	1 1534
23 hr	1.290	1.1534
30 hr	1.159	1.1534

Table 4.6: Density of the strip prepared for M.A. 80Ni-20Fe powders at various stages of processing.

Strip	Apparent density (g/c.c.)	%T.D
1.Green strip of M.A. 80Ni-20Fepowder, 6.23mm thickness.	2.84	32.7%
2.Suitered M.A. 80Ni-20Fe powder, 5.23mm thickness,(Sintering Temp=1273K,Snitering tune=15min)	3.76	43.2%
3.Hot Rolled M.A. 80Ni-20Fe strip, 3.14mm thickness, (Hot Rolling Temperature 1273K, % H.R. reduction=40%)	5.29	60.8%
4.Hot Rolled M.A. 80Ni-20Fe strip, 2.35mm thickness (Hot Rolling Temperature=1273K, % H.R. reduction w.r.t. the thickness of the sintered strip=55%)	5.99	68.9%



A141906